The variety of forced atmospheric structure in response to tropical SST anomaly in the Aqua-Planet Experiments

Kensuke NAKAJIMA

Faculty of Sciences, Kyushu University, Fukuoka, Japan

and

Yukiko YAMADA

Faculty of Science, Hokkaido University, Sapporo, Japan

and

Yoshiyuki O. TAKAHASHI

Center for Planetary Sciences, Kobe, Japan
Kobe University, Kobe, Japan

and

Masaki ISHIWATARI

Faculty of Science, Hokkaido University, Sapporo, Japan

and

Wataru OHFUCHI

Earth Simulator Center, Japan Agency of Marine Science and Technology, Yokohama, Japan

and

Yoshi-Yuki HAYASHI

Center for Planetary Sciences, Kobe, Japan
Kobe University, Kobe, Japan

December 18, 2012

Corresponding author: Kensuke Nakajima, Faculty of Sciences, Kyushu University, 6-10-1, Hakozaki, Fukuoka, Fukuoka 812-8581, Japan.
E-mail: kensuke@geo.kyushu-u.ac.jp

Abstract

We examine the steady state responses of the models participating in the Aqua-Planet Experiment project (APE) to zonal asymmetry of equatorial sea surface temperature (SST) anomalies (SSTAs). Experiments are performed with three different SSTA distributions, which are localized SSTAs with common shape but with two different intensities and a SSTA varying with zonal wavenumber one. The obtained structures of the responses differ significantly among the models. However, some features which can be regarded as common exist.

The principal features of the responses to the localized SSTAs are a positive precipitation anomaly over the SSTA, widespread negative precipitation anomaly along the intertropical convergence zone, a pair of Rossby wavetrains along the equatorward flanks of mid-latitude westerly jets originating from a pair of upper tropospheric anticyclones that develop to the east of the SSTAs, and zonally wavelike precipitation and geopotential anomalies along the baroclinic zones. It is worth notifying that the structure of the tropical responses are considerably different from the Matsuno-Gill pattern. The magnitudes of the response is almost proportional to the intensity of the localized SSTA in each of the models.

The responses to the zonal wavenumber one SSTA are dominated by zonal wavenumber one structures. Around the longitudes of the warm

(cold) SSTA, tropical precipitation increases (decreases). At the longitudes shifted eastward of the positive precipitation anomaly, the region of nearly zero absolute vorticity around the equator in the upper troposphere expands polewards, and the mid-latitude westerly jets become narrower and stronger. Around the longitudes shifted westward of the positive precipitation anomaly, the upper tropospheric region of nearly zero absolute vorticity shrinks, and the mid-latitude jets become weaker but broader, so that the regions of westerly winds reach to the equator resulting in the development of zonal mean westerly wind anomaly around the equator. The longitudinal shift of the upper tropospheric westerly zonal wind anomaly relative to the precipitation anomaly is in marked contrast to that realized for the Walker circulation and the convection center around the Maritime continent.

1. Introduction

The general circulation of the atmosphere is driven by thermal inhomogeneity in the atmosphere itself and that of the ground or ocean surface below. In addition to the planetary scale meridional thermal contrast caused by inhomogeneity of solar radiation, there are zonal contrasts caused by surface inhomogeneity such as land-sea contrasts and sea surface temperature (SST) variations. Surface thermal contrasts drive a variety of zonally inhomogeneous responses in the atmosphere (Webster, 1983) such as inhomogeneity of precipitation (Lindzen and Nigam, 1987; Neelin and Held, 1987), zonally propagating equatorial waves (Matsuno, 1966; Gill, 1980), and Rossby wavetrains propagating to extratropics (Bjerkness, 1969; Hoskins and Karoly, 1981). Inhomogeneity of precipitation is caused not only directly by the local surface condition but also indirectly by the remote surface condition through long-reaching circulation anomaly (Hosaka *et al.*, 1998; Nakajima *et al.*, 2004). These atmospheric responses, in turn, affect the conditions of ground and sea surface underneath, all of which form mutual feedback processes of the land-sea-atmosphere system. Appropriate understanding of such interactions is not only important in theoretical interest but also indispensable for practical purposes such as weather prediction and projection of future climate.

With those important roles of zonal inhomogeneity of the surface conditions in mind, the Aqua-Planet Experiment Project (APE) defined three zonally inhomogeneous SST distributions to be specified in the atmospheric general circulation model (AGCM) intercomparison. As is presented in Neale and Hoskins (2000a) and is reproduced in Blackburn and Hoskins (2012) in this special issue, each of these three distributions, 1KEQ, 3KEQ, 3KW1, consists of an SST anomaly (SSTA) placed at the equator superposed on the CONTROL profile, one of the zonally homogeneous SST distributions of the APE. In the two of them, 1KEQ and 3KEQ, the SSTAs are localized, whereas in the other, 3KW1, the SSTA takes a form of zonal wavenumber one variation. The purpose of these specifications are, as stated in Blackburn and Hoskins (2012), (i) to determine the circulation response to a localized anomaly in tropical SST, what processes determine the local and global responses, and how these vary between models, and (ii) to determine the circulation response to a planetary scale anomaly in tropical SST, which involves the generation and propagation of planetary-scale Rossby waves, their longitudinal modulation of the extra-tropical storm-track and their impact on meridional transports. All of these issues are among the important ring of chains producing the complex behavior of the atmosphere in the climate system (Alexander et al, 2002; Liu and Alexander, 2007).

The purpose of the present paper is to examine the results of AGCM experiments conducted with the zonally varying SSTs in the APE, namely, to identify similarities and differences in the structure of atmospheric features that develop as the responses to the SSTAs in the 15 participating models. We describe the steady state responses of precipitation because it is the primary "conduit" from the tropical SST to the global atmosphere. We also describe and compare tropical and extratropical dynamical responses, i.e., pressure and wind fields.

We will present rather extensive number of figures, most of which compare various features of the responses in all of the 15 participating models. By providing those figures, this paper will serve as one of the reference material on the APE, in particular, on the results on the experiments with zonally varying SST. The choice of figures in the present paper is to be complementary to the APE-ATLAS (Williamson et al. 2012a). The APE-ATLAS contains a large number of figures showing the zonally averaged response to the SST anomalies, the space-time spectra of precipitation at the equator, and model mean response structure etc., but the figures showing the responses of individual models are limited.

Another intention of the present paper to be complementary to the APE ATLAS is the explanation of the response structures depicted in the figures. APE-ATLAS contains a large number of figures, but it provides little description or explanation on those figures. Of course, this is because it aims to be a collection of figures of the results of the APE project. In this aspect, the present paper can be regarded as an overview on the subset of the APE, which complements the two overview papers (Blackburn *et al.* 2012; Williamson *et al.* 2012,this issue), both of which cover the cases with zonally symmetric SST.

In the followings, a number of unique features and new issues will be presented in due course of the description of the APE results with zonally inhomogeneous SST. In the present paper, however, we will not go into the details of them. Our focus here is to describe the results of this subset of the APE as complete as possible. Theoretical investigations of those interesting issues will be left for future studies.

The paper is organized as follows. Section 2 will explain the setup of the experiment, the data, and the method of analysis. In Section 3, principal features of the atmospheric structures in the experiment with zonally homogeneous CONTROL SST profile will be briefly reviewed because it stands as the "basic state" of the experiments with SSTAs. In Section 4, response to a localized equatorial SST anomaly will be described mainly with the 3KEQ runs, and in Section 5, response to zonal wavenumber one variation of SST will be described with the 3KW1 runs. Summary and remarks will be given in the last section.

2. Methods

2.1 Specification of SST

SST in each experiment are prescribed as functions of latitude (φ) and longitude (λ). In CONTROL experiments, the SST, expressed in degrees Celsius, is zonally uniform and given as

$$T_{\mathrm{CONTROL}}(\lambda,\varphi) = \begin{cases} 27\left[1-\sin^2\left(\frac{90}{60}\varphi\right)\right] & \text{if } |\varphi| < 60^\circ, \\ 0 & \text{if } |\varphi| \geq 60^\circ. \end{cases} \tag{1}$$

Neale and Hoskins (2000) states that the CONTROL SST profile is chosen as the standard "because it leads to a definite, but not unrealistic, single ITCZ regime" in their preliminary experiment. However, as is described in Blackburn et al (2012), definite double ITCZ emerge in some of the APE models. The flattening of SST in the higher latitudes is introduced in order to prevent the ocean surface from freezing in the participating models, which are state-of-the-art climate or numerical weather prediction models.

In 1KEQ, 3KEQ, and 3KW1 experiments, SST anomalies are added to the CONTROL SST given above, which are

$$T_{\mathrm{1KEQ}}(\lambda,\varphi) = \begin{cases} \cos^2\left(\frac{90}{15}\varphi\right)\cos^2\left(\frac{90}{30}\lambda\right) & \text{if } |\varphi| < 15^\circ \text{ and } |\lambda| < 30^\circ, \\ 0 & \text{otherwise,} \end{cases} \tag{2}$$

$$T_{\mathrm{3KEQ}}(\lambda,\varphi) = \begin{cases} 3\cos^2\left(\frac{90}{15}\varphi\right)\cos^2\left(\frac{90}{30}\lambda|\right) & \text{if } |\varphi| < 15^\circ \text{ and } |\lambda| < 30^\circ, \\ 0 & \text{otherwise,} \end{cases} \tag{3}$$

and

$$T_{\mathrm{3KW1}}(\lambda,\varphi)=\begin{cases}3\cos^2\left(\frac{90}{30}\varphi\right)\sin(\lambda) & \text{if } |\varphi|<30^\circ,\\ 0 & \text{otherwise,}\end{cases} \tag{4}$$

respectively. These SST distributions are plotted in Fig. 1.

By comparing 1KEQ or 3KEQ with CONTROL, we can examine the response of the global atmosphere to a localized equatorial SSTA, including anomalous precipitation and equatorial and extratropical wave activities which develop responding mainly to the latent heating in the precipitation anomaly. By comparison between 1KEQ and 3KEQ, we can obtain a hint on how 'linearly' the atmosphere behaves to an imposed SSTA. Comparison between 3KW1 and CONTROL should provide information on atmospheric responses to planetary scale zonal variations of tropical SST.

Also plotted in Fig. 1 is another zonally uniform SST distribution of the APE setup, QOBS, whose latitudinal profile is broader than that of CONTROL. In comparison to QOBS which is chosen to be "a simple geometric function closest to the observed zonal mean SST distributions" (Neale and Hoskins 2000a), the characteristics of the CONTROL profile is that the region of high SST are confined around the equator and the region of large latitudinal gradient of SST are located in the lower latitudes. As will be described later, because of this characteristics of the CONTROL profile, the climatological states obtained in the APE runs of the CONTROL experiment are somewhat peculiar in all of the participating models compared to those known for the real atmosphere, and the responses to the SSTAs are greatly influenced by these climatological states. Fig. 1

In some models, there are a few differences from the standard specification. First, in the 1KEQ and 3KEQ setups of ECMWF05, the western half of the SSTA lacks unintentionally. Second, in the 3KW1 setups of ECMWF05 and ECMWF07, the meridional scale of the SSTA is halved unintentionally. We decide to include the results of these experiments in this paper although such off-specifications should affect the characteristics of the response to the SSTA. As will be shown later, these cases display unique characters of response, so that they enrich the variety of the models to be compared. Third, in GFDL, the mean surface pressure is 1000hPa instead of the standard value of 1013.25hPa. As a result, GFDL model might exhibit slightly stronger responses to SSTA than other models would, since 1.35 % deficit of the air pressure results in the same amount of the increase of water vapor mixing ratio. However, we expect that this small amount does not affect the overall features of responses of the GFDL runs, and assume that this does not affect the argument of intercomparison to be presented here.

2.2 Data and analysis

Data for the analysis in this paper is the results of the AGCM runs with the SST distributions of CONTROL, 1KEQ, 3KEQ, and 3KW1 of the APE conducted by 15 participating groups, whose specifications are briefly summarized in Table 1. Unfortunately, the parameterized forcing (PF) data, which is "optional" in the data specification of the APE project, is archived for a subset of the participating models. Consequently, the responses of latent heating due to convective and resolved cloud processes are analyzed for 9 out of the 15 models. For further details, readers are referred to the APE-ATLAS (Williamson et al. 2012a).

All of the materials presented in this paper concern the steady response of variables in the AGCMs to the anomalies of SST defined above. We leave examination of time dependent responses for future research, including the responses of convectively coupled equatorial waves, the change of transport properties of mid-latitude baroclinic waves, and the development processes of stationary waves. The anomaly as the steady response of a particular variable is calculated for each model as the difference between the temporal mean value of the variable obtained in the particular run of 1KEQ, 3KEQ, or 3KW1 SST profile and the temporal and zonal mean value of the variable in the CONTROL experiment of the model. The integration period of each APE run is 3.5 years. Steady state data are obtained by taking the temporal average over the last 3 years of the time series of each run. Table 1

3. Structure of the atmosphere in CONTROL experiment

As a minimal reference information with which the results of the SSTA experiments presented later can be compared, the temporal and zonal mean meridional structures of the CONTROL experiment is briefly described here. We present the results from one of the models, NCAR. as an example, because the ensemble average of the results of all models would blur dynamically important features. Various aspects and differences observed in the results of the APE models are summarized in Blackburn *et al.* (2012a) and are extensively presented in the APE-ATLAS (Williamson et al. 2012a). Although the climatological states of the APE models show a significant amount of diversity even for the temporal and zonal mean structures as is described in those references, the followings are the features fairly common among the CONTROL runs of the APE models if not specifically mentioned.

Figure 2 shows the temporal and zonal mean structure of the atmosphere obtained in the CONTROL run of NCAR. The latitudinal profile of precipitation (Fig. 2(d)) shows a double ITCZ structure at the equator, but the equatorial minimum is not very strong. It should be remarked that the overall characteristics of the CONTROL runs is that precipitation tends to be sharply confined around the equator, although the structure of the ITCZ, i.e., single peaked or double peaked, considerably varies among the APE models.

In the mid-latitudes, the baroclinic zone is shifted equatorward, and so does the mid-latitude jet (Fig. 2(a) and (b)) , compared to their locations in the real atmosphere (Blackburn *et al.* 2012; Williamson *et al.* 2012b). Near the surface, the maximum of the westerly is located at a few degrees poleward of the upper jet core latitude (Fig. 2(b)). Correspondingly the precipitation maximum associated with the baroclinic waves resides further poleward around 40 degrees latitude (Fig. 2(d)). In the followings, we refer to this single and intense tropospheric westerly jet as the mid-latitude jet.

The tropical upper troposphere is strongly influenced by this peculiar mid-latitude jet profile. At the level of 200hPa, mean zonal wind is westerly at 15 degrees latitude with the intensity of 15 m s^{-1} and exceeds 30 m s^{-1} at 20 degrees latitude. The deep "invasion" of the westerly into the tropics is one of the common features of the CONTROL runs of the APE. Note that the term "invasion" above is used bearing only the morphology of the westerly jets in mind. Dynamically, the strong westerly in the upper tropical troposphere results from the poleward transport of angular momentum from the equator by the upper branch of the Hadley circulation as suggested by nearly homogeneous distribution of absolute vorticity in the upper troposphere equatorward of the latitudes of $\sim \pm 15°$ (Fig. 2(c)). This peculiar feature of zonal wind in the tropics strongly affects many aspects of the general circulation. As results, some characteristics of the atmosphere, including the responses to SSTAs described later, are distinctly different from those often described for the real atmosphere. Fig. 2

4. Response to localized SST anomaly: 1KEQ, 3KEQ

4.1 Characteristic feature of response

In this section, 15 AGCM runs mainly for 3KEQ are presented and compared with one another. Since the structures of the responses are not very simple and vary among the models considerably, in this subsection, we will identify principal features of the response to the 3KEQ SSTA focusing on one of the models, GFDL, as a clear example before the full comparison for the purpose of helping readers grasp similarities and differences among the responses. In later subsections, we will describe the variety of the responses by pointing out the difference in intensity, locations, or shapes etc., of the features to be identified here. After that, we will present multi model statistics of the response of geopotential.

The horizontal distributions of the responses of several atmospheric variables to the 3KEQ SST anomalies of GFDL model are shown in Fig. 3(a)-(g). Absolute vorticity at 250hPa is also shown in Fig. 3(h) but will be discussed later. It can be easily noted that the structures are mostly symmetric about the equator except near the poles. Dominance of north-south symmetry in the response is a common character in the 3KEQ and the 3KW1 runs among all of the 15 APE models. Symmetry degrades in the 1KEQ runs, but it definitely survives in the lower latitudes (not shown).

Figure 3(a) shows the response of precipitation. There are three latitudinal bands where the response is notable; one is the latitudes of the ITCZ, and other two regions are equatorward flank of the mid-latitude baroclinic zones $\sim 30°$. In the response at the ITCZ, there are two notable characteristics. First, a strong positive anomaly develops over the prescribed warm SST anomaly as a direct response to the SSTA, and negative anomaly prevails in the remaining longitudes. Second, the reduction of precipitation is not zonally uniform; the negative anomaly is weak at some longitudes, ($\lambda \sim -180°, -140°, -70°, 85°$, and $140°$), and even positive anomalies appear. Similar wave-like zonal variation can be found also in the mixing ratio anomaly at 700 hPa (Fig. 3(b)), although the signal is significant not on the ITCZ but at about 10 degrees off the equator. In the responses near the baroclinic zones, the precipitation anomalies also exhibit a wave-like structure; the most notable feature is the appearance of east-west dipoles consisting of the positive anomalies centered at $(\lambda, \varphi) \sim (60°, \pm 32°)$ the negative anomalies centered at $(\lambda, \varphi) \sim (10°, \pm 32°)$. The positive anomaly in the mid-latitudes may be regarded as a generic structure of the increase of rainfall observed in the western United States during the warm events of El Niño (Hoerling and Kumar 2002). In other longitudes, the signature of the precipitation anomaly is generally negative, but some degree of wave-like variation can be found. The anomaly of vertical velocity at 500hPa (Fig. 3(c)) exhibits a structure consistent with that of precipitation, i.e., upward (downward) motion in the areas of positive (negative) precipitation anomaly, except that the magnitude of the mid-latitude signal of vertical velocity is more conspicuous than in the precipitation.

Figures 3(d)-(f) show the dynamical response at the middle, the lower, and the upper troposphere, respectively. One of the most puzzling features is that the equatorial Kelvin wave response expected to the east of the SSTA as a Matsuno-Gill pattern (Matsuno, 1966; Gill, 1980) seems to be absent or obscured. In the lower troposphere (Fig. 3(e)), there is no easterly anomaly in the neighborhood to the east of the SSTA along the equator; an easterly wind anomaly can be found in the longitudes of $\lambda \sim 60 - 100°$ but it is disconnected from the area of SSTA. In the upper troposphere (Fig. 3(f)), there is no westerly anomaly in the neighborhood to the east of the SSTA; the upper level wind anomaly is easterly to the east along the equator, which is contrary to that in the Kelvin response of the upper level in a Matsuno-Gill pattern. It is also notable that a pair of anticyclones expected to the west in the standard Matsuno-Gill pattern are not significant. At 850hPa, a pair of velocity anomalies of cyclonic curvature around $(\lambda, \varphi) = (-40° \sim 0°, \pm 10°)$ may be a trace of the equatorial Rossby wave response to the SSTA. At 250 hPa, no pair of anticyclones expected to the west of the SSTA are present; instead, a pair of anticyclonic wind anomalies develop to the *east* of the SSTA around $(\lambda, \varphi) = (0 - 20°, \pm 20°)$, which seems to spread widely in the latitudinal direction and seems to be smoothly connected to the anomalies in higher latitudes. Due to the combination of the eastward shifted Rossby response and apparent absence of the Kelvin response, the upper level divergence associated with the enhanced precipitation at the SSTA consists of meridional divergence and zonal convergence, which is the contrary to that expected from a Matsuno-Gill pattern in an atmosphere without background wind. In short, the tropical response structure in 3KEQ is drastically different from the structure expected in the classical linear theory of thermal response to a localized equatorial heat source without background wind. In the upper troposphere, non-linearity becomes important and the reality of the simple frictional law becomes uncertain. Even in such cases, the longitudinal location of the Rossby response is at the longitude of SSTA or westwards; it does not develop to the east of SSTA (Sardeshmukh and Hoskins, 1988). The eastward development of Rossby response in 3KEQ contradicts to both linear and non-linear theories of thermal response of the equatorial atmosphere. As is presented in Appendix A, this seemingly strange response can be understood when the unique structure of zonal mean zonal wind in CONTROL (and 3KEQ) of the APE is taken into account.

Difference of the response structure from that expected from a standard Matsuno-Gill pattern without background wind is also evident in the vertical section on the equator (Fig. 3(g)). The upward motion and positive temperature anomaly in the area of the positive precipitation anomaly over the SSTA agree to what is usually expected, although the vertical structure is somewhat complex. However, the response of zonal wind is quite strange; in the low levels especially to the east of the SSTA, the signal is very weak, and in the middle- and upper-troposphere, the anomaly is zonally converging. There are two additional unusual features in the temperature response. First, there is a negative temperature anomaly to the west of the SSTA. This may be to some extent explained as a response to the negative precipitation anomaly to the west of the SSTA (e.g., Hosaka *et al.*, 1998). Second, there is an area of positive temperature anomaly to the east centered around (p, λ) $\sim$ (600hPa, 70°). It is partially detached from the warm anomaly over the SSTA, and, moreover, the vertical structure is different from that of the warm anomaly over the SSTA; the temperature anomaly is most intense at the middle troposphere where that over the SSTA has a minimum. This warm anomaly seems to be induced by the deep downward motion at the longitude around $100°$ (Fig. 3(c) and 3(g)), which is supported by the meridional convergence in the upper troposphere (Fig.3(f)) to the east of the pair of anticyclones.

In the extratropics, there exist a pair of barotropic Rossby wavetrains which are notable in the geopotential anomaly of the upper troposphere (Fig.3(f)). They emerge as a pair of anticyclones centered at $(\lambda, \varphi) = (10°, \pm 30°)$ poleward of the anticyclonic circulations to the east of the SSTA mentioned above, propagate to the higher latitudes to appear as a pair of cyclones at $(\lambda, \varphi) = (50°, \pm 40°)$, turns back equatorward to appear as a pair of anticyclones at $(\lambda, \varphi) = (90°, \pm 30°)$, and then appear as a pair of cyclones at $(\lambda, \varphi) = (130°, \pm 20°)$. The Rossby wavetrains seem to continue further eastward to encircle the mid-latitudes, meandering about the westerly jets. As is demonstrated in Appendix A, the Rossby wavetrains are excited mainly by the meridional advection of absolute vorticity by the wind anomaly diverging from the location of positive precipitation anomaly above the SSTA. The vertical structure of the Rossby wavetrains is equivalent barotropic; by comparing Fig.3(e) and (f), we can recognize that the locations of the cyclonic and anticyclonic geopotential centers coincide throughout the troposphere. It is worth notifying that the temperature anomaly is positive (negative) at the high (low) pressure anomalies (Fig.3(d)), and hence the height anomaly is more intense in the upper troposphere (Fig.3(e) and (f)). In the lower atmosphere at 850hPa (Fig.3(e)), geopotential anomalies in the higher latitudes are more prominent; they are anticyclones at $(\lambda, \varphi) = (-60°, \pm 40°)$ and cyclones at $(\lambda, \varphi) = (50°, \pm 40°)$.

It should be noted that the zonal wavenumber of the Rossby wavetrains is about 5, which is the same as that of the quasi-stationary features found in the CONTROL experiments (Blackburn *et al.*, 2012; the APE-ATLAS, (Williamson et al. 2012a)). Comparing Fig. 3(a) and Fig. 3(f), the Rossby wavetrains seem to affect the equatorial anomalies of precipitation; precipitation at the ITCZ seems to be enhanced (suppressed) around the longitudes of midlatitude anticyclonic (cyclonic) perturbations in the upper troposphere. As is discussed in Section 9 of Blackburn *et al.* (2012), similar quasi-stationary wave-like variations of precipitation at the ITCZs are identified in the most of CONTROL runs of the APE models. This may imply that the wave-like variation of precipitation found in the 3KEQ runs may not be a response to the SSTA, but is a kind of intrinsic variation which exists also in the CONTROL setup. However, we do not exclude the possibility that this feature is a significant signal caused by the introduction of the SSTA based on the two pieces of supporting evidences; the amplitude of the meridional wind anomalies is larger in the 3KEQ run of GFDL than in the CONTROL run by a factor of about two, and, the north-south symmetry is much more distinct than that in CONTROL (see fig.4.99 of the APE-ATLAS, (Williamson et al. 2012a)). Fig. 3

4.2 Variety of response among the 15 APE models

a. Precipitation response

Table 2

In the following three subsections, we will compare the responses to the SSTA in 3KEQ experiment in the 15 APE models. Figure 4 shows time mean precipitation anomaly. Since the response is mostly symmetric about the equator in all of the APE models, southern hemisphere below the latitudes of $-15°$ is omitted. Region of the latitudes higher than $60°$ is also omitted because the precipitation, and its anomaly, is weak.

As for the overall characteristics of precipitation responses, we can identify all of the corresponding features of the precipitation anomalies mentioned for the GFDL run in the previous subsection, i.e., the intense positive anomaly over the SSTA, the mostly negative anomaly along the ITCZ outside of the SSTA, the east-west dipoles on the equatorward flanks of the baroclinic zones. The wave-like modulation in the tropics and mid-latitudes, presumably related to wavenumber 5 stationary disturbances, can also be found. However, the detailed structures of the precipitation anomalies are model dependent.

Focusing on the responses in the ITCZ, the positive anomalies over the SSTA for CGAM, CSIROstd, K1JAPAN, and NCAR have two maxima straddling the equator, whereas those for the remaining models have single maxima at the equator. This variation of the meridional profiles seems to reflect those of the ITCZ in the CONTROL runs of the corresponding models, which are presented in Blackburn *et al.* (2012). The responses of ITCZ precipitation outside the SST also exhibit different meridional structure In CSIROold, DWD, ECMWF05, GFDL, and LASG, single zones of negative precipitation anomalies develop along the equator. On the other hand, in the other models, negative anomalies are dominant along the latitudinal lines of $\varphi \sim \pm 5°$.

It should be remarked that the meridional "double trough" structure of the negative anomaly is not a simple reflection of the structure of the ITCZ in the CONTROL experiment. In CGAM, K1JAPAN, and NCAR, the meridionally double-peaked structures of the precipitation anomalies outside the SSTA in 3KEQ are very distinct although the double ITCZ structures observed in the CONTROL experiment have rather modest equatorial minima of precipitation (see Fig.4 in Blackburn et al, 2012). In CGAM, K1JAPAN, and NCAR, zonally averaged anomalies outside the

SSTA along the equator are positive. The double peak structure of precipitation anomaly appears also in MIT where the ITCZ in CONTROL is broad but single peaked. In short, precipitation becomes focused to the equator to a larger degree in the models where the ITCZs in CONTROL are broad, whether they are single or double. This behavior of precipitation reminds us of the equatorial precipitation enhancement found in the response to an localized equatorial SSTA in Hosaka *et al.* (1998), where an equatorial Kelvin wave plays an important role in the meridional focusing of precipitation. However, the dynamics of the precipitation response observed in 3KEQ is left for future study.

Figure 5 and Table 2 show the intensities of the precipitation anomalies at the ITCZs and mid-latitude baroclinic zones in the 15 APE models more quantitatively. In the left column of Fig. 5, the longitudinal distributions of precipitation anomalies along the equator are listed. The peak value over the SSTA varies over a factor of 5 with the weakest response in K1JAPAN to the strongest response in ECMWF05. Since the longitudinal extent of the SSTA in ECMWF05 is half of the APE specification as was noted in section 2, it is expected that the response in ECMWF05 could be still stronger if the SSTA of the specified size were placed. If we compare the anomalies of precipitation by a relative measure, by dividing the precipitation anomaly in 3KEQ by the zonal mean precipitation at the corresponding latitudes in

CONTROL for each run, scattering among the models reduces considerably (the leftmost two columns in Table 2); the maximum values ranges from 156% to 333%, and the minimum values are about 70 % of the CONTROL on the equator. As for those models with "double peak" structure, the range of the scaled responses at the off-equatorial peak latitudes are shown in the next two columns of Table 2. Some of those models show the rainfall reduction of the amount of even larger than half of the CONTROL. Such reduction of precipitation at the off-equatorial peak latitudes occur typically just to the west of the SSTA, as suggested by the distribution of unscaled precipitation anomaly (Fig. 4(b),(c),(g),(i),(j),(l)–(o)).

In the central column of Fig. 5, the longitudinal distributions of the anomalies of precipitation meridionally averaged between $\pm 15°$ in the 15 models are plotted. Since the variety of meridional structure is mostly eliminated by the meridional averaging, the longitudinal distribution becomes similar to each other, although a few outliers still remain. The scaled responses in the same latitudinal band listed in the 6th and 7th columns of Table 2 also confirm the reduction of scattering among the models; in most of the models, the maximum located on the SSTA is $\sim$250% and the minimum located to the west of the SSTA is $\sim$70% of the precipitation in CONTROL experiment. Similar significant reduction of precipitation to the west of the SSTA is also found in previous studies (Hosaka *et al.*, 1998;

Neale and Hoskins,2000b) and has been explained as a result of a Rossby wave response.

In the right column of Fig. 5, the longitudinal distributions of the precipitation anomalies on the southern flank of mid-latitude baroclinic zone averaged between 20°N and 40°N are plotted. The dipole shape anomaly consisting of reduction at the longitude around 0° and the enhancement at the longitude around 60° is commonly noted in all of the models but with varying intensity. The variation with wavenumber 5, noted earlier, can also be identified and its amplitude varies among the models. In the scaled responses listed in the last two columns of Table 2, the amplitudes of mid-latitude average precipitation anomalies are about 20% of the CONTROL in most of the models. Fig. 4

Fig. 5

b. Horizontal structure of dynamic fields

Horizontal structures of the responses, namely anomalies of horizontal wind and geopotential height, on the 250hPa and 850hPa surfaces for all of the 15 models are shown in figures 6∼9. As is in the case of the precipitation anomalies, since the responses are mostly symmetric about the equator, the southern hemisphere is omitted.

Generally speaking, we can identify the features identified in GFDL previously, which are (1) the tropical response that is dissimilar to the

Matsuno-Gill pattern, (2) the extratropical equivalent barotropic Rossby wavetrains and the wavenumber 5 feature along the baroclinic zone excited by the meridional divergent wind from the positive precipitation anomaly over the SSTA, and, (3) the prominent appearance of zonally dipole geopotential anomalies in the higher latitudes at the 850hPa level. However, the intensities, the horizontal scales, and the locations of these features considerably differ among the models. For example, the amplitude of the negative geopotential height anomaly at 250 hPa typically centered around $(\lambda, \varphi) = (40°, \pm 50°)$ constituting the propagating Rossby wave train ranges from about 30m of LASG and MRI to about 100m of GFDL and NCAR. The wavenumber 5 feature along the westerly jet is quite prominent in CGAM, DWD, GFDL, MIT, and NCAR, whereas it is almost absent in AGUforAPE, CSIROld, K1JAPAN, and LASG.

In the upper troposphere, acceleration of zonal mean zonal wind is observed in some of the models, most notable of which are MIT and NCAR. This acceleration mainly occur in the upper troposphere higher than 300hPa. The confinement to the upper troposphere suggests that the acceleration is driven by the Rossby waves excited by the precipitation anomaly and emitted to the higher latitudes.

It is also found that appreciable zonal mean responses develop in the high latitudes. For ECMWF05 and K1JAPAN, for instance, the high latitudes are covered with intense positive geopotential anomalies at the level of 850 hPa (Fig. 8(f) and Fig. 9(j)). For CSIROold, the north polar region is occupied by an intense high pressure anomaly covering all of the troposphere (Fig. 6(d) and Fig. 8(d)). However, whether it is true time mean response or not is uncertain because the zonal mean fields in the high latitudes undergo considerably large amplitude variation with a fairly long period (exceeding 100days) as described in the ensemble AGCM study on the response to an equatorial SSTA by Nakajima *et al.* (2004); the zonal mean responses in the high latitudes found here may be an artifact that could disappear for the longer averaging interval.

Fig. 6

Fig. 7

Fig. 8

Fig. 9

c. *Multi model statistics of the response*

Figure 10 (a) shows the model mean response of geopotential and horizontal wind vectors at 250hPa, and Fig. 10 (b) shows the standard deviation of the geopotential anomalies in 3KEQ at 250hPa in the 15 APE models. Figure 10 (c) and (d) show those at 850hPa. The principal features of the dynamical response, which are the Rossby wavetrains originating from the anticyclonic anomalies that develop to the east of the SSTA and the perturbation along the mid-latitude westerly jets at 250hPa, and the zonally dipole geopotential anomalies in the higher latitudes at 850hPa level, can be easily identified in the multi model mean response (Fig. 10 (a)). However, the intensities of those features are generally weaker than those in the individual models. For example, the amplitude of the model mean Rossby wavetrain, about 100m, is considerably smaller than the representative amplitudes of the Rossby wavetrains in the individual models (Fig. 14(a) shown later) presumably because of the scattering of longitudinal phases of the response in the 15 APE models found in Fig. 6 and 7. In fact, the magnitudes of the standard deviations of the responses is nearly as large as the amplitudes of the response at the two levels. The diversity of the mod-latitude response among the models can also be reflected in enhanced values of standard deviation along the mid-latitude jet (Fig. 10 (b) and (d)). The large standard deviation at 850hPa in higher latitude represents the scattering of the geopotential response in polar region.

It is worth mentioned that the equatorial Kelvin wave response appears a bit clearer in the multi model mean response than in the individual models (Fig. 6$\sim$ 9); The lower level easterly and upper level westerly wind anomalies along the equator is easily identifiable to the east of $\varphi \sim 90°$. Nearer to the SSTA, the Kelvin response, if it is present to any degree, seems to be completely overshadowed by the intense Rossby responses that develop in that longitudinal region pointed out for the responses in the individual model. Fig. 10

d. Vertical structure along the equator

The vertical structures of the responses, namely, anomalies of temperature, zonal wind, and vertical p-velocity, along the equator for all of the 15 models are shown in Fig. 11. Although the intensity and the detailed anomaly patterns are strongly model dependent, very roughly speaking, the overall response structures of all models can be regarded to be similar to that of GFDL described earlier; the warm upward motion develops over the SSTA, the zonal wind anomaly is very different from that of the first baroclinic equatorial Kelvin wave, and the deep warm anomaly exists to the east of, and partially detached from the SSTA.

The variety of the vertical structure of the temperature anomalies over the SSTA among the models can be interpreted to be varying contributions of following three components: first, a positive anomaly extending from the surface to about 900hPa directly caused by the SSTA, second, a negative anomaly around 600hPa caused by the melting of frozen hydrometeor, and third, a deep warm anomaly in the upper half of the troposphere. Rather surprisingly, the temperature anomaly in the lowermost troposphere, which is more or less directly controlled by the SSTA of specified intensity, show significant diversity; the intensity of the temperature anomaly at 925 hPa varies over a factor of as large as five. This point will be discussed in section 4.3. Several factors, including parameterizations of physical processes such as surface fluxes, turbulence in the mixed layer, and rain evaporation (or the lack of it), could contribute to the difference.

One would expect that the intensities and the patterns of the mid-tropospheric cold anomaly and the upper tropospheric warm anomaly vary among the models, because they are directly forced by the cloud heating which are differently parameterized in different models (Table 1). The vertical section of the latent heating anomaly at the equator in nine models for which the parameterized heating data is available are compared in Fig. 12. Rather surprisingly, the vertical profiles in most of the models exhibit good amount of similarity; except DWD and LASG, heating anomaly is mostly confined to the upper half of the troposphere, although the distribution within the upper troposphere varies among the models. It should be noted, however, that the partitioning of the heating anomaly into parameterized and resolved heatings is strongly model dependent.

Figure 13(a)–(i) show the vertical distributions of the anomaly of temperature tendency due to parameterized and resolved cloud processes at the maxima of precipitation anomaly. In the lower troposphere, the anomalies of parameterized and resolved heatings tend to cancel with each other for ECMWF07, GSFC, and NCAR, whereas both of the two components are weak for AGUforAPE, ECMWF05, and K1JAPAN. The interpretation of the different contributions of the parameterized and resolved heating in different models is not straightforward because different models employ different cloud schemes. Heating near the surface strongly varies among the models; in ECMWF07, K1JAPAN, and NCAR, shallow but intense cooling exists near the sea surface, which is presumably the effect of parameterized evaporation of rain.

Comparison between the vertical profiles of the heatings in these models and the responses at the equator (Fig. 11) reveals that the correspondence between the structures of heating and temperature anomalies above the SSTA is not straightforward. For example, at around 600hPa, a negative temperature anomaly can be found in all models with the latent heating data except for GSFC and LASG in spite that the heating anomaly is positive except for AGUforAPE. Of course, it may not be surprising because other effects, such as advection, diffusion, and other parameterized heating terms, would affect. We do not go further than pointing out that there is considerable difference of the vertical structure of the response. The most peculiar example is GSFC where most of the lower troposphere is occupied by a cold anomaly, which reminds us of the similar cold anomaly found at the location of the enhanced precipitation in the composite convectively coupled equatorial waves in the APE CONTROL experiment by the GSFC model (Nakajima et al. 2012). In GSFC, CSIROstd and K1JAPAN, the vertical velocity anomalies in the lowermost troposphere (below 850hPa) are slightly downward in the convection area at the SSTA. The development of downward flow anomaly at the convective area may seem to be counter intuitive. However, considering that “basic state” upward motion exists along the equator and that the anomaly of convective heating in the lower troposphere above the SSTA is positive at least in two of these models, GSFC and K1JAPAN (Fig. 13(e) and (f)), we can expect that the development of deep convection even with downward perturbation vertical velocity.

To the west of the SSTA, temperature anomaly is generally negative. The anomaly seems to be composed of two separate components; the component in the lower troposphere lying from 1000hPa to 700hPa, and the component in the upper troposphere around 300 hPa. These two seem to appear differently on the models. The low level negative anomaly tends to be prominent in the models with significant negative precipitation to the west of the SSTA, i.e., AGUforAPE, CSIROold, DWD, ECMWF05, ECMWF07, GFDL, LASG, and MIT. On the other hand, that in the upper troposphere tends to be prominent in CSIROstd, CSIROold, DWD, GFDL, and UKMO, most of which are characterized with narrow single ITCZ in the CONTROL experiment. The former model dependence seems to be understandable, whereas the latter remains to be considered.

Although certain deep warm anomalies are commonly notified around several thousand kilometers to the east of the SSTA for all of the models, their longitudinal and vertical distributions and the intensity vary considerably among the models. Comparison among the equatorial sections suggests that the structure of this warm anomaly seems to be related to the structure of temperature anomaly over the SSTA to some extent. For example, in ECMWF05, ECMWF07, and GSFC, where the mid tropospheric cooling over the SSTA is significant (Fig. 11(f),(g), and (i)), the detached warm anomalies are vertically shallow. The intensity of the detached warm anomaly seems to be correlated with the intensity of the Rossby wavetrains generated from the SSTA to the mid-latitudes; the models that exhibit strong detached anomalies, namely, CGAM, CSIROold, MIT, and UKMO, are characterized with intense Rossby wavetrains (Fig. 6 and Fig. 7). Still, the correspondence is not perfect; for example, in NCAR, the Rossby wavetrain is prominent (Fig. 7(n)), but the detached warm anomaly is not very conspicuous (Fig. 11(n)). Other factors, such as the structure of zonal mean zonal wind, and the vertical structure of heating over the SSTA, can also matter. Since the heating anomalies at the corresponding locations are quite weak (Fig. 12(a)–(i)), it is probable that these temperature anomaly have dynamical origin. Further analysis is required to clarify the mechanism for generation and maintenance of the detached warm anomaly. Fig. 11

Fig. 12

Fig. 13

4.3 Relationships among the variables

So far, we have been describing variations of the atmospheric response to the 3KEQ SSTA in different models examining several different variables separately. In this subsection, we examine the relationships among the responses of different variables derived from the 3KEQ runs, and try to identify the sources that produce the variation of the responses found so far in the comparisons among the APE models.

a. Dynamical response

Fig. 14

In the previous subsection, we pointed out large varieties of the equatorial precipitation responses (Fig. 4, Fig. 5 and Table 2) and extratropical geopotential responses in the upper (Fig. 6 and Fig. 7) and lower troposphere (Fig. 8 and Fig. 9). Here, we examine the relationship between the intensities of the tropical precipitation anomaly and the extratropical response.

Figure 14(a) shows the relationship between the amplitude of precipitation anomaly averaged within the $\pm 15°$ latitudes and the amplitude of geopotential height anomaly on 250hPa. Here, the amplitude of geopotential height anomaly is calculated as the difference between the maximum and minimum values of the eddy component geopotential height, practically showing the intensity of Rossby wavetrains at 250hPa. The amplitude of precipitation is represented in the unit of equivalent amount of latent heat; 1000 W m^{-2} corresponds to 4×10^{-4} kg s^{-1} m^{-2}. We can find that both of the amplitudes scatter over the ranges of factor of 2.5, and seem to be in proportion to each other. A similar correlation can be observed also for the wave amplitude at the lower troposphere (not shown here). This correlation suggests that, the variety in the amplitude of extratropical waves mainly results from the variety in the intensity of the tropical precipitation anomaly. Still, a considerable deviation from this correlation remains; for example, in spite that the precipitation amplitudes of MRI and CSIRO are almost the same, the amplitudes of the extratropical waves in these two models differ almost by a factor of two. Several other issues, such as the vertical structure of heating and the structure of the mean flow should be also considered, although we do not go into these issues any further in this paper.

Figure 14(b) shows the relationship between the amplitude of the precipitation response averaged within $\pm 15°$ latitudes and the amplitude of the zonal mean zonal wind anomaly at 200hPa within the same latitudinal band. Although vaguely positive correlation may be present, the variety of the zonal mean wind response is quite large. Figure 14(c) shows the relationship between the upper tropospheric meridional transport of zonal momentum by stationary eddy at 10°N and the amplitude of the zonal mean zonal wind anomaly at 200hPa within averaged within $\pm 10^\circ$ latitudes. More conspicuous correlation between the two variables found in the figure implies the important role of stationary eddy in the zonal mean wind acceleration. However, examination of the time series data of the APE runs shows that the zonal mean zonal winds fluctuate over O(1) m s^{-1} with various time scale ranging from O(10)–O(100) days in each model, so that the degree of zonal wind acceleration is not very certain.

b. Factors controlling precipitation anomaly

Here we examine the response of several variables that could induce the responses of precipitation. First, we compare the amplitude of the precipitation anomaly with the amplitude of the low level temperature anomaly which has an influence in the degree of convective instability. Second, we compare it with the zonal mean intensity of precipitation in the CONTROL experiment, which serves as the "basic state" of precipitation. Third, we compare it with the amplitude of the evaporation anomaly which contributes the moisture supply for the enhanced precipitation. We employ the following two values as the amplitudes of anomalies; one is the intensity averaged within $\pm 5^\circ$ which reflects the variety of the meridional structure among the models, and the other is the intensity averaged within $\pm 15^\circ$ which indicates the longitudinal variation of the precipitation anomaly of the ITCZ as a whole. [1]

Figure 15(a) is the scatter plot showing the amplitude of the precipitation anomaly versus the amplitude of the temperature anomaly at 925hPa averaged within the $\pm 5°$ latitude band. It is rather surprising that the temperature amplitude varies over a factor of four among the models. A vague positive correlation can be found between the two variables, but it is far from conclusive. Figure 15(d) is a similar scatter plot but for the average within the $\pm 15°$ latitude band. The variation among the models is smaller than in Fig. 15(a). Still, the temperature amplitude varies over a factor of three. The two variables seem to be positively correlated. These comparisons of the responses suggest that the intensity of the precipitation response to the localized equatorial SSTA is to some extent controlled by the processes that governs the low level temperature response to the SSTA.

Figure 15(b) the scatter plot showing the amplitude of the precipitation anomaly versus the amplitude of the surface latent heat flux anomaly averaged within the $\pm 5°$ latitude band. The amplitude of the latent heat flux anomaly varies over a factor of three. The correlation between the two amplitudes is very weak. Figure 15(e) is a similar scatter plot but for the average within the $\pm 15°$ latitude band. The scattering of amplitude of the

[1] It should be noted that the western half of the SSTA is lacking in ECMWF05, so that the real response of this model is presumably much stronger.

latent heat flux response is narrower than that for the $\pm 5°$ latitude band; it varies over a factor of two. Now, it seems that there is a good correlation between the two amplitudes. However, the appearance seems to be heavily affected by the existence of an isolated point, MIT, without which other data points are rather clustered around the average. Even if we admit the proportionality between the amplitudes of the precipitation and the latent heat flux anomalies, it should be remarked that the latent heat amplitude is only about a fourth of the precipitation amplitude; there are other major remaining factors that contribute to the intensity of precipitation anomaly.

Figure 15(c) is the scatter plot showing the amplitude of the precipitation anomaly versus the zonally averaged precipitation in the CONTROL experiment averaged within the $\pm 5°$ latitude band. There seems to be a positive correlation in this figure, which may be considered as reasonable. This is because, as was pointed out earlier in this section (Fig. 4), the precipitation response near the equator in the 3KEQ run of a particular model depends heavily on the tropical structure of precipitation and circulation of the corresponding CONTROL run. Figure 15(f) is a similar scatter plot but for the average within the $\pm 15°$ latitude band. Scattering among the models becomes smaller, since the meridional change of ITCZ is averaged out. A weak positive correlation is noted, suggesting that the meridionally averaged precipitation response to an localized equatorial SSTA is stronger in the model where the ITCZ precipitation is large.

In summary, we suggest positive correlations between some pairs of variables above. but, as a whole, the correlations are not conclusive. We also presented the cases where clear correlations are not seen. However, we consider that even such seemingly "negative" results worth presented, because they provide additional information on the characteristics of the variations realized in the participating models. Actually, it should be stressed that even the temperature response in the low level, whose behavior to the SSTA is expected to be rather trivial, scatters in a wide range. The mechanism underlying these scattering should be pursued but we leave it for future studies. Fig. 15

4.4 Linearity of response to localized SST anomaly

By comparing the results of the 3KEQ and the 1KEQ experiments, we can obtain some idea on the extent of linearity of the response to the equatorial localized SSTA. The overall structures of the responses to the 1KEQ SSTA, whose distributions are not shown here, are mostly common to the 3KEQ SSTA except that they are considerably weaker as described below.

Figure 16(a) shows the scatter plot of the amplitudes of precipitation anomalies for 1KEQ and 3KEQ. Fig. 16(b) shows the similar scatter plot but for the averages within the $\pm15^\circ$ latitude band. UKMO is not plotted because 1KEQ experiment was not performed in the model. If the response is linear, the data points should distribute along the line with the slope of 3. Actually, the behavior of many of the models follow the expected relationship in both figures.

Figure 16(c) shows the scatter plot of the amplitudes of extratropical geopotential anomalies at 250hPa in 1KEQ and 3KEQ. Although the amplitudes in 3KEQ and 1KEQ are certainly positively correlated, the ratio between the amplitude in 3KEQ and that in 1KEQ far less than 3, which may indicate the presence of some nonlinearity that suppresses extratropical wave amplitudes. However, we should remind of the possible contributions from the background fluctuations that exist without the SSTA. In fact, the amplitudes of quasi stationary waves in the CONTROL experiment are as large as from 40 to 70m depending on the model. If we tentatively set the background level to be 40m in both experiments and draw a line with the slope of 3 originating from this background level, the results from the models seems to be well explained. Quantitative examination of this point requires more careful statistical considerations and is left for future research. Fig. 16

5. Response to wavenumber one variation of SST: 3KW1

5.1 Characteristic feature of response

In this section, 15 AGCM runs for 3KW1 are presented and compared with one another. Like we did for 3KEQ, before the full comparison in the next subsection and a short presentation of the multi model statistics follows further, we will identify principal features of the response to the 3KW1 SSTA focusing on one of the models, which is NCAR this time, as a clear example in this subsection. Since the intensity of the response is quite strong, we choose to describe the time mean response of NCAR to the 3KW1 SSTA in Fig. 17 by showing mainly the raw values of variables rather than the anomalies from those for the CONTROL run. Southern hemisphere below the latitudes of $-15°$ is omitted because the response is mostly symmetric about the equator.

Forced by the zonal contrast of SST reaching 6 K (Fig. 1), precipitation in the tropics (Fig. 17(a); see also Fig. 19(n) for the corresponding anomaly field) is mostly concentrated within the region of the warm SSTA. There is almost no rainfall over the cold SST region, where downward motion develops and the mid troposphere becomes very dry (Fig. 17(b) and (c)). Mid-latitude precipitation, which is associated with the activity of baroclinic waves, is shifted to the lower latitudes and enhanced around the longitudes to the east of the SST maximum (Fig. 17(a) and Fig. 19(n)). Both of the tropical and the mid-latitude precipitation anomalies are represented as distinct zonal wavenumber one variations around the corresponding latitudes. It is also noted that the anomalies in the tropics and the mid-latitudes are connected. Wavenumber one structure is also identified in the field of vertical motion at the equatorward flank of the baroclinic zone (Fig. 17(c)).

Corresponding to the intense longitudinal variation of the ITCZ precipitation, a wavenumber one, first baroclinic mode structure develops in the tropics as is seen in the mid-level temperature field (Fig. 17(d)) and the lower- and upper-level geopotential height fields (Fig. 17(e) and (f); see also Fig. 21(n) and Fig. 22(n) for corresponding anomaly fields). The maximum of the upper tropospheric high pressure in the tropics is located at the longitudes about 30 $\sim$ 40 degrees to the east of the precipitation maximum (Fig. 17(f)). In the upper troposphere, wind is generally weak in the high pressure region around the equator. Equatorial westerly wind bifurcates at the western tip of the high pressure around $(\lambda, \varphi) \sim (-60^\circ, 0^\circ)$ and merges at the eastern tip around $(\lambda, \varphi) \sim (110^\circ, 0^\circ)$. In the lower troposphere, on the other hand, a pair of anticyclonic anomalies develop in the subtropics in the longitudes to the west of the precipitation maximum centered at $(\lambda, \varphi) \sim (-130^\circ, \pm 20^\circ)$ (Fig. 17(e)). The variation of mid tropospheric temperature, warm around $\lambda \sim 20°$ and cool around $\lambda \sim -140°$ (Fig. 17(d)), is consistent with those of the lower and upper geopotential variations mentioned above. Around the maximum of precipitation in the ITCZ, lower (upper) level zonal flow is divergent (convergent), whereas meridional flow is convergent (divergent) (Fig. 17(e) and (f), and Fig. 21(n) and Fig. 22(n)).

The vertical structure of the zonal wave number one response in the tropics can be confirmed in Fig. 17(g), which shows the equatorial section of zonal wind, vertical p-velocity, and temperature deviation from its zonal average. Both of the fields of temperature and vertical motion vary with zonal wavenumber one patterns, as was already shown in the horizontal sections. The upward motion over the longitudes of the intense precipitation is intense and extends over the full depth of the troposphere. On the other hand, the vertical motion outside the precipitation area is generally weak. The warm anomaly over the warm SST area observed in Fig. 17(d) for the level of 500hPa has a complex vertical structure; the signature of the anomaly is positive at the lower and the upper levels, but is negative at the middle level presumably resulting from the melting of the icy precipitation. There is a positive temperature anomaly around the longitudes about 100 degrees to the east of the SSTA peak.

The westerly wind outside the warm region observed in Fig. 17(f) for the level of 250hPa develops throughout the upper half of the troposphere.

The same section for the same variables but for the anomalies from CONTROL experiment is shown in Fig. 25(n). There is one peculiar behavior worth notifying in the anomaly of vertical velocity; the raw vertical motion (Fig. 17(g)) is upward over the full depth of troposphere, but its anomaly (Fig. 25(n)) appears only in the upper half of troposphere. The response of vertical velocity to the imposition of the SSTA is quite small in the lower levels.

As was in the case with the localized anomaly, 3KEQ, many of the characteristics of the tropical response summarized above are in contradiction to those expected in the classical linear theory of thermal response to a wavenumber one equatorial heat source without background wind, where the off-equatorial upper-tropospheric high pressure anomalies develop to the west of the heat source (e.g., Fig.9 in Matsuno, 1966). In the NCAR 3KW1 run, the upper tropospheric high pressure region (Fig. 17(f)) seems to be corresponding to the “zero potential vorticity” area associated with the active convection; absolute vorticity is homogenized within the high pressure region in the upper troposphere as seen in Fig. 17(h). However, an important difference from the zero potential vorticity region in the real atmosphere which usually develop at or to the west of the convection center (Sardeshmukh and Hoskins, 1985) is that it develops to the east of the convection center in the 3KW1 experiment. This is also considered to be a result of the invasion of strong westerly wind in the upper troposphere observed in the CONTROL runs of APE that is mentioned in Section 3.

Comparing the horizontal distribution of the absolute vorticity in the upper troposphere in 3KW1 (Fig. 17(h)) and that in CONTROL (Fig. 2(c)), we notice that the meridional gradient of absolute vorticity in the upper troposphere in cool SST region in 3KW1 is much steeper than that in CONTROL. As noted at the beginning of this subsection, the ITCZ precipitation in the region of the negative SSTA almost disappears (Fig. 17(a)). Due to this drastic change of precipitation, the upper tropospheric poleward flow of the Hadley cell also disappears in the longitudes of the negative SSTA. Consequently, the equatorial air parcel with zero absolute vorticity can not be transported over the wider latitudes around the equator. Instead, the air parcel of the subtropical latitudes with the larger absolute vorticity is advected to the equatorial region. The extreme change of the tropical upper tropospheric absolute vorticity distribution in 3KW1 is in contrast to that in 3KEQ (Fig. 3(h)), where the degree of change responding to the SSTA is only modest wavy perturbations.

The extratropical response structure is also characterized with zonal wavenumber one. In the upper troposphere, the westerly jet is shifted equatorward and strengthened in the longitudinal regions to the east of the SSTA maximum (Fig. 17(f) and Fig. 21(n), where the mid tropospheric meridional temperature gradient is also enhanced (Fig. 17(d)). The activity of baroclinic waves is also enhanced along the intensified westerly jet manifested as the low level cyclonic anomaly (Fig. 17(e)) and the upper level trough (Fig. 17(f)) that develop to the north of the jet enhance region to the east of the SSTA. In the longitudes of the suppressed precipitation, the westerly jet is weak but becomes broader to reach equator (Fig. 17(f)), and considerably cool air is advected from higher latitudes in the longitudes around $\lambda = -180^\circ \sim -90^\circ$, (Fig. 17(d)). The invasion of westerly jets around the longitudes of the cold SSTA results in considerable acceleration of zonal mean zonal wind. Figure 18 shows the meridional structure of the anomaly of zonal mean zonal wind in 3KW1 of NCAR from that of CONTROL. The westerly acceleration is centered in the equatorial upper troposphere and confined within the Hadley cell. The low latitude flank of the westerly jets are considerably decelerated in the upper troposphere, and stratospheric wind in high latitudes is also decelerated.

In the anomaly from the CONTROL experiment (Fig. 21(n)), the strengthening and narrowing of the jet in the upper troposphere around the longitudes of the warm SSTA corresponds to the region of enhanced meridional geopotential gradient between the positive anomaly around the equator and the negative anomaly just to the north of the jet. Conversely, the weakening and broadening of the upper tropospheric jet around the the longitudes of cold SST is represented as the north-south oriented dipole geopotential anomaly centered around $\lambda = -150^\circ$, positive (negative) in the poleward (equatorward) side straddling the mid-latitude westerly jet. In the lower troposphere, the development of cyclonic anomaly just to the north of the baroclinic zone in the raw geopotential field at 850 hPa and the meander of the westerly jet (Fig. 17(e)) are represented as a distinct zonal wavenumber one anomaly of geopotential at or slightly poleward of the baroclinic zone (Fig. 22(n)). In the extratropics poleward of the westerly jet, the vertical structure of the geopotential height anomaly is equivalent barotropic, whereas it is baroclinic in the tropics. Fig. 17

Fig. 18

5.2 Variety of response among the 15 APE models

a. Precipitation response

In the following three subsections, we will compare the responses to the SSTA in 3KW1 experiment in the 15 APE models. Since the responses are mostly symmetric about the equator for all of the APE models, southern hemisphere below the latitudes of -15° is omitted from the figures of the horizontal structures of the responses. The latitudes higher than 60° are also omitted because the precipitation anomalies are weak there.

In Fig. 19 we compare the time mean precipitation anomalies obtained in the 15 AGCM runs of APE. As is demonstrated by the case of NCAR in the previous subsection, zonal wavenumber one patterns are evident in wide range of latitudes in all of the models. The dominance of wavenumber one is shared among variables other than the precipitation for all models. There are three latitudinal bands where the response is notable; the ITCZ around the equator and the mid-latitude baroclinic zones (one for each hemispheres). As additional features which are also common to all models, we can point out a few items below. Unlike the case of the 3KEQ SSTA, the wavenumber 5 variation along the baroclinic zones can not be identified, or is overshadowed by the wavenumber one anomaly which is much stronger than the east-west dipole in the 3KEQ. In the higher latitudes, precipitation decreases around $\lambda = 0°$ and increases around $\lambda = 180°$ along $\varphi \sim \pm 50°$ in the majority of the models.

The meridional structures of the precipitation anomalies at the ITCZs vary among the models. The models can be classified into three categories concerning the positive anomaly pattern over the warm SSTA: First, CSIROstd has two distinct zonally elongated maxima along the latitudes around $\pm 6°$. Second, ECMWF05 and ECMWF07 exhibit an intense maximum along the equator associated with a pair of negative anomaly bands; this peculiar feature results presumably from the accidental narrow meridional scale of the SSTA used in these two ECMWF experiments as noted in Section 2. The equatorial concentration of precipitation is quite intense in ECMWF05, but is not so intense in ECMWF07, as will be shown below. Third, in other models, the positive anomaly is most intense along the equator but has some meridional extent. Focusing on the negative anomaly pattern over the cool SSTA, the models can be classified into two categories. In CGAM, GSFC, K1JAPAN, NCAR and UKMO, the reduction of precipitation is intense at two latitude bands off the equator. In the rest of the models, it is most intense at the equator. The meridional structure of the negative anomaly of a particular 3KW1 run reflects the meridional structure of the ITCZ in the corresponding CONTROL run. Since the precipitation anomaly in 3KW1 is so strong that the precipitation over the cool SST area is almost completely suppressed (e.g., Fig. 17(a) for NCAR). As a result, the precipitation anomaly there becomes simply the rainfall in CONTROL but with the negative signature.

Focusing on the behavior of precipitation in the subtropics, the models can be classified into two groups. In GSFC, MRI, NCAR, and also in ECMWF07, there are noticeable anomalies in the subtropics that bridge the equatorial and the mid-latitude anomalies. The anomaly pattern, tilted from south-east to north-west in the northern hemisphere, suggests the presence of Rossby waves propagating from the tropics to the higher latitudes. In other models, such features are weak or absent.

The intensities of precipitation anomalies around the ITCZs and the baroclinic zones of the 15 APE models are summarized in Figure 20 and Table 3. In the left column of Fig. 20, the zonal distributions of precipitation anomalies along the equator are listed. Excluding the two experiments of ECMWF that are undoubtedly affected by the off-specification of narrow meridional scale of the SSTA, the peak-to-peak amplitude varies over a factor as large as 5 from the weakest of CSIROstd to the strongest of DWD. It is also noted that the precipitation maximum is not necessarily located at the position of the highest SST. In the majority of the models, the precipitation peaks are located to the west of the SST peak by the longitudes of 10$\sim$40 degrees. An exception is LASG, in which the precipitation peak is shifted to the east.

If we compare the precipitation anomalies normalized by the precipitation obtained in the CONTROL run for each model, scattering among the models reduces considerably like in 3KEQ as shown in the first and the second columns of Table 3; the maximum values range from 115% to 282%, and the minimum values range from 9% to 42% of the CONTROL runs on the equator, excluding the two ECMWF experiments for which the meridional width of the SSTA is half that for the other models. As for those models with the double peaked ITCZ structure, the scaled responses at the off-equatorial latitudes are shown in the third and fourth columns of Table 3). In CSIROstd and K1JAPAN, the scaled positive precipitation anomalies are stronger than those at the equator. In CSIROstd, the amount of precipitation at the off-equatorial maxima is about 4 times that of CONTROL, resulting the distinct meridional splitting of the positive precipitation anomalies (Fig. 19(c)). In CGAM and K1JAPAN, the negative anomalies are much stronger than those at the equator.

In the central column of Fig. 20, the longitudinal distributions of the anomalies of precipitation meridionally averaged over an equatorial band within $\pm 15°$ of the 15 models are plotted. In spite that the variety of meridional structures are eliminated by the meridional averaging, a considerable longitudinal variation among the models still remains. The scaled response in the same latitudinal band listed in the sixth and seventh columns of Table 2 also confirms the reduction of scattering among the models; the maxima are about 200% and the minima are about 30% of the CONTROL runs. The shape of the zonal variations of precipitation is sawtooth-like in the majority of the models; going to the east, it increases slowly and then decrease steeply.

In the right column of Fig. 20, the meridional distributions of the precipitation anomalies at the mid-latitude baroclinic zone averaged between $20° N$ and $40° N$ are plotted. They are dominated by the wavenumber one variation in common. The peaks are located at the longitudes around $\lambda = 90°$ in most of the models, and the amplitudes of them do not vary much among the models. This similarity among the mid-latitude precipitation responses contrasts to the much larger variety found in the 3KEQ runs listed in the right column of Fig. 5. In the scaled variation listed in the last two columns of Table 3, the amplitudes of midlatitude average precipitation anomalies reach about 60% of the CONTROL runs in most of the models, which are about three times as those in 3KEQ.

Fig. 19

Table 3

Fig. 20

b. Horizontal structure of dynamic fields

The horizontal structures of the responses, namely the anomaly fields of horizontal wind and geopotential height, on the 250hPa and the 850hPa surfaces are shown in figure 21 and 22 for all models. Since the responses are mostly symmetric about the equator, the southern hemisphere below the latitudes of $-15°$ is omitted.

The major features of the response described for NCAR in section 5.1 are common among the models, though the intensities, the locations and other details of the anomaly patterns differ among the models. At the level of 250hPa (Fig. 21), a positive geopotential anomaly appears on the eastern side of the warm SSTA longitudes, a north-south oriented dipole anomaly centered around the longitude of $\lambda \sim -150°$ develops straddling the mid-latitude westerly jet, and a negative anomaly appears just poleward of the jet around the longitudes of the SSTA. At the level of 850hPa (Fig. 22), a distinct zonal wavenumber one anomaly of geopotential at or slightly poleward of the baroclinic zone can be noted. Positive anomaly of zonal mean zonal wind in the tropical upper troposphere like that observed in NCAR (Fig. 18) can also be found in most of the models. However, as will be compared later, their intensities vary significantly among the models. The invasion of westerly wind to the equatorial region around the longitudes of the cold SSTA is, as was mentioned for NCAR, considered to be responsible for the zonal wind acceleration (Fig. 21). A further noteworthy feature is that, a trace of Rossby wave propagation from the tropics to the mid latitude baroclinic zone can be found in CSIROold, GSFC, MRI, and NCAR at the level of 250hPa (Fig. 21(d), (i), (m) and (n), respectively). A series of geopotential height anomalies continue in the subtropics with westward phase tilt from the lower to the higher latitudes. Fig. 21

Since the responses in the 3KW1 experiments are dominated by zonal wavenumber one patterns as have been described above, we compare the responses paying attention to the amplitudes and phases of the wavenumber one components of a few variables. Figure 23(a) compares the amplitudes and phases of the precipitation anomalies averaged in the latitudinal band between $\pm 15^{\circ}$. Although the amplitudes scatter over a factor of about 2, the phases are well concentrated within a longitudinal range of 30 degrees. In most of the models, the precipitation response is shifted to the west lon- Fig. 22

gitudinally by about 30 degrees from the SST variation. Figure 23(b)–(d) compare the amplitudes and phases of geopotential anomalies at the level of 250hPa at the latitudes of 20, 40, and 60 degrees, respectively. The amplitudes and phases at 20 degrees latitude are distributed in a fairly compact region which is located slightly to the east of the SSTA; relative scattering of the amplitudes looks smaller than that of the precipitation (Fig. 23(a)). At 40 degrees latitude, the phases of the geopotential anomalies are scattered considerably, but scattering of the amplitudes is still within 30% of its average value. However, at 60 degrees latitude, the phases of the geopotential anomalies are scattered over a quite large range of degrees; the phase variation reaches almost 90 degrees, and scattering of the amplitudes exceeds factor of 5. One might imagine that the larger scattering of wave properties in the higher latitudes might quite natural because of the naive nature of Rossby wave propagation and increase of geopotential magnitude in variabilities of geostrophic phenomena as the increase of latitude. However, quantitative analyses on these issues remain to be performed. Fig. 23

c. Multi model statistics of the response

Figure 24 (a) shows the model mean response of geopotential and horizontal wind vectors at 250hPa, and Fig. 24 (b) shows the standard deviation of the geopotential anomalies in 3KW1 at 250hPa in the 15 APE models.

Figure 24 (c) and (d) show those at 850hPa. Because the responses in 3KW1 in the 15 APE models commonly shared zonally wavenumber one structure, which is directly represented in the model mean response. It is notable that the distribution of the standard deviations has considerable longitudinal inhomogeneity. In low latitudes, the scattering of the upper tropospheric geopotential anomaly among the models (Fig. 24(b)) is smaller (larger) in the region of high (low) pressure anomaly. Such correlation is absent in the lower level (Fig. 24(d)). In the extratropics, the locations of enhanced scattering in the lower and upper levels nearly coincide, presumably resulting from the generally barotropic structure of response in the individual models. Fig. 24

d. Vertical structure along the equator

Figure 25 shows the vertical sections of the anomalies of temperature, zonal wind, and vertical p-velocity at the equator of the 15 APE models. Figure 26 shows the vertical sections of the anomalies of temperature tendency due to the sum of parameterized and resolved cloud processes of the 9 APE models where data are available. Figure 27(a)–(i) show the vertical distributions of the anomalies of temperature tendency due to parameterized and resolved cloud processes at the maxima of precipitation anomalies in the 9 APE models. The anomalies of temperature, vertical motion, and latent heating are all dominated with the zonal wavenumber one variations for all of the models, although their vertical structures vary considerably.

The longitudinal distributions of the upward motion and the positive heating anomalies roughly coincide with the distribution of precipitation anomalies (the left column of Fig. 20) in most of the models The anomaly of the vertical motion in CSIROstd exhibits an exception; downward motion dominates over the most of the area of the lower troposphere below 600hPa. This is presumably a result of the the distinct “double peak” structure of the positive precipitation anomaly of CSIROstd around the warm SSTA (fig. 19(c)) and the associated trough line of precipitation anomaly along the equator.

The location of the temperature anomalies (represented by the contours in Fig. 25, is shifted to the east of the precipitation anomalies typically by the longitude of 20 to 40 degrees. As for the temperature anomaly in the lower troposphere, the eastward shift could be explained by the advection of colder air from the higher latitudes by the meridionally converging low level wind anomaly that develop between $\lambda \sim -60^\circ$ and $\lambda \sim 0^\circ$ (Fig. 22). As for the temperature anomaly in the middle and upper troposphere, the eastward shift results presumably from the eastward advection by the westerly wind invading the tropics (Fig. 2(b)). The vertical structure of temperature anomaly is not simple and model dependent. Still, several common characters can be found, one of which is that the temperature anomalies in the middle troposphere are weaker and shifted to the east of the precipitation anomalies. In AGUforAPE, GSFC, and NCAR, the temperature anomalies at the level around 600hPa are more complicated; we can find shallow, eastward shifted, positive anomalies, presumably related to the melting and/or freezing of hydrometeors.

Compared to the temperature anomalies at the equator in 3KEQ (Fig. 11), the temperature anomalies at the equator in 3KW1 are considerably stronger; typical temperature increase of the positive anomalies at 700hPa is 1.5–2 K in 3KW1, whereas it is 0.5–1 K in 3KEQ. In other words, the "weak temperature gradient approximation" (Sobel *et al.*, 2001) does not apply well in 3KW1 even along the equator.

The heating anomaly corresponding to the positive precipitation anomaly is intense in the upper troposphere for all of the models except for LASG. Accordingly, the upward motion around the peak of the precipitation anomaly is stronger in the upper troposphere than in the lower troposphere in most of the models. However, again as in 3KEQ, the correspondence between the vertical structures of heating and vertical motion is not perfect; for example, the thin heating anomaly just above 600hPa and the thin cooling anomaly just below in AGUforAPE (Fig. 27(a)) are not reflected in the vertical velocity response. Instead, the shallow warm anomaly develops at 600hPa to the east of the precipitation anomaly (Fig. 25(a)). The shallow regions of cooling, found in ECMWF07, K1JAPAN, and NCAR, induced by the evaporation of rain in the lowest atmosphere are not reflected in the corresponding vertical velocity anomalies. This is presumably because of the effects of other physical processes which cancel the cooling such as turbulent mixing, and also its proximity to the sea surface which prohibits the vertical motion.

The signature of the heating anomalies in the regions of suppressed precipitation is mostly negative (Fig. 26). The vertical structures of the heating anomalies in the regions of the positive and the negative precipitation anomalies are not the same. In most of the models, heating in the positive precipitation anomaly is more intense and is located in the higher levels, and, is richer in the components with short vertical wavelengths. This deviation from the perfect asymmetry between the positive and the negative heating anomalies is also reflected in the structure of vertical motion in the corresponding model (Fig. 25). K1JAPAN exhibits an additional interesting character; outside the region of positive rainfall anomaly, there is shallow but significant *positive* heating anomaly develop below 800 hPa (Fig. 26(f)) between $\lambda = 50°$ and $\lambda = 180°$ (Fig. 19(j)). Corresponding shallow upward motion anomaly also exists (Fig. 25(j)). Origin of this peculiar behavior is not identified.

In most of the models, the westerly wind anomaly over the longitudes of the cold SSTA, which was mentioned as a characteristic at the level of 250hPa in Fig. 21, extends over the upper half of the troposphere, and contributes to the zonal mean zonal wind anomaly, which will be discussed later.

Fig. 25

Fig. 26

Fig. 27

Fig. 28

5.3 Relationships among the variables

As we have done for 3KEQ, we examine the relationships among the responses of different variables and try to identify the sources that produce the variation of the responses found so far in the comparisons among the APE models. Like done for 3KEQ, we employ the peak-to-peak range as the gross measure of the amplitude of the anomaly of a variable.

a. Dynamical response

Figure 28(a) shows the scatter plot between the amplitude of the precipitation anomaly averaged over the equatorial latitudes between $\pm 15^\circ$ and the amplitude of the geopotential anomaly at the level of 250 hPa at the equator. The amplitude of precipitation is shown in the unit of equivalent amount of latent heat; 1000 W m^{-2} corresponds to 4×10^{-4} kg s^{-1} m^{-2}. It can be recognized that the range of scattering of the geopotential anomalies are comparable to the typical magnitude of geopotential variation (the half of the peak-to peak magnitude of anomaly) and no signature of correlation with the precipitation anomaly can be found. Such characteristics are also seen for the geopotential anomalies at other latitudes (not shown). Other factors such as the difference of the vertical structure of heating may explain the scattering.

Figure 28(b) shows the relationship between the upper tropospheric meridional transport of zonal momentum by stationary eddy at 10° N and the amplitude of the zonal mean zonal wind anomaly at 200hPa within averaged within ±10° latitudes. Some correspondence between the two variables found, suggesting the importance of stationary eddy in the zonal mean wind acceleration, but the correlation is not very well; for example, the difference between the magnitudes of momentum flux in DWD and NCAR is only modest, but the zonal mean zonal wind acceleration differ over a factor of two. Figure 28(c) shows the scatter plot between the precipitation in 3KW1 within ±10° latitudes and the amplitude of the zonal mean zonal wind anomaly at 200hPa, where a weak negative correlation can be noted. The positive correlation with poleward export of easterly momentum by stationary eddy (Fig. 28(b)) and the negative correlation with equatorial precipitation (Fig. 28(c)) are consistent with the result of Kraucunas and Hartmann (2005), who compare idealized GCM experiments with prescribed zonally symmetric and zonally asymmetric heating and show that the equatorial superrotation is accelerated by the export of easterly momentum by tropical stationary eddy and decelerated by the vertical advection of easterly momentum by the upward motion near the equator.

b. Factors controlling precipitation anomaly

Here we examine the response of several variables that could induce the response of precipitation. First, we compare the amplitude of precipitation anomaly with the amplitude of low level temperature anomaly, which could have a certain influence in the degree of convective instability. Second, we compare it with the zonal mean intensity of precipitation in the CONTROL experiment, which serves as the "basic state" of precipitation. Third, we compare it with the amplitude of evaporation anomaly, which contributes to the supply of moisture for the enhanced precipitation. As in Fig. 15, we employ the following two values as the amplitudes of anomalies; one is the intensity averaged within $\pm 5°$ which reflects the variety of the meridional structure among the models, and the other is the intensity averaged within $\pm 15°$ which indicates the longitudinal variation of the precipitation anomaly of the ITCZ as a whole. [2]

---

[2] ECMWF05 and ECMWF07 are excluded in the comparison concerning the precipitation anomaly averaged within $\pm 5°$. However, we include these two models in the comparison concerning the precipitation anomaly averaged within $\pm 15°$ because the intensity of precipitation response averaged within this latitudinal band does not seem to be affected by the narrow meridional scale of the SSTA setup of these two runs very

Figure 29(a) is the scatter plot showing the amplitude of precipitation anomaly versus the amplitude of temperature anomaly at 925hPa averaged within the $\pm 5^\circ$ latitude band. The amplitude of temperature anomaly varies over a factor of 1.5 among the models. The range is considerably narrower than that for 3KEQ. Figure 29(d) is a similar scatter plot but for the average within the $\pm 15^\circ$ latitude band. The amplitude of temperature anomaly varies over a factor of two among the models. In contrast to the case with 3KEQ (Fig. 15(a) and (d)), no trace of positive correlation can be found between the amplitudes of the precipitation anomaly and the low level temperature anomaly. This absence of correlation arises from the existence of the intense temperature anomaly occupying the whole depth of the troposphere (Fig. 26), which is roughly in phase with the low level temperature anomaly and tends to cancel the variation of convective instability that could be caused by the low level temperature and moisture anomalies.

Figure 29(b) is the scatter plot showing the amplitude of precipitation anomaly versus the amplitude of surface latent heat flux anomaly averaged within the $\pm 5^\circ$ latitude band. As in the case of 3KEQ, the amplitude of the latent heat flux anomaly varies over a factor of three. However, the correlation between the amplitude of precipitation anomaly and the amplitude of surface latent heat flux anomaly is very weak. Figure 29(d) is a

seriously as seen in the central column of Fig. 20.

similar scatter plot but for the averages within the $\pm 15^\circ$ latitude band. The scattering range of the amplitude of latent heat flux anomaly is narrower than that for the $\pm 5^\circ$ latitude band; it varies over a factor of about two. As in the case of 3KEQ, there is a good degree of correlation between the two amplitudes. Moreover, the ratio of the amplitude of latent heat anomaly to the amplitude of precipitation anomaly is larger than for 3KEQ; it reaches about 40%, compared to about 25% of 3KEQ.

Figure 29(c) is the scatter plot showing the amplitude of precipitation anomaly versus the zonal mean precipitation amount in CONTROL averaged within the $\pm 5^\circ$ latitude band. As in 3KEQ, positive correlation is found in this figure. This seems to be reasonable, because, as is pointed out in section 5.2(a), the response of precipitation near the equator exhibits large model dependence consisting of the latitudinal structure which inherits the that latitudinal structure of precipitation in the corresponding CONTROL run of the model. Figure 29(f) is a similar scatter plot but for the average within the $\pm 15^\circ$ latitude band. Scattering among the models is smaller because the meridional structure of ITCZ is averaged out. As in 3KEQ, a weak positive correlation can be found. Fig. 29

5.4 *Comparison between the responses in 3KEQ and 3KW1*

So far, we have been describing the variety of the behaviors of the APE models for 3KEQ and 3KW1 separately. As the last item of model comparison in the present paper, we briefly compare the responses for 3KEQ and for 3KW1. We limit ourselves mostly to the comparison of the responses of precipitation, which is the primary forcing agent in the atmospheric general circulation and might be expected to respond more directly to a given SSTA complared to other variables; the responses of other variables would be more complicated by a number of interacting processes within the models.

Figure 30(a) shows the relationship between the amplitudes of precipitation anomalies of 3KEQ and 3KW1 averaged within $\pm 5°$ latitudes among the models. The anomalies of 3KEQ and 3KW1 are roughly in proportion to each other. If we disregard MIT as an outlier, the correlation increases further. Similar tendency can be found also for the precipitation ageraged within $\pm 15°$ latitudes (Fig. 30(b)).

The good correspondence between the intensities of precipitation anomalies in 3KEQ and 3KW1 settings is, in fact, not surprising, because both of them are correlated with the precipitation intensity in the corresponding CONTROL run (Fig. 15(c), (d), and, Figure 28(a), (b)). Even normalized by the precipitation in the corresponding CONTROL run, some correlation still remains between the precipitation anomalies averaged within $\pm 5°$ latitudes (Fig. 30(c)). Some positive correlation can also be noted between the normalized midlatitude responses in 3KEQ and 3KW1 (Fig. 30(e)). However, in the normalized anomalies averaged ±15° latitudes, we cannot find a singnature of correlation (Fig. 30(d)). The origin of these characteristics is unclear and we leave the pursuit of it for a future study.

Figure 30(f) shows the correspondence between the amplitudes of zonal mean zonal wind anomalies in 3KEQ and 3KW1. Although uncertainty of about 1m s^{-1} should be counted in the anomalies for 3KEQ as noted in section 4, some degree of positive correlation can be identified.

Finally, we comment on the vertical structures of heating response, which are shown in Fig. 12 and Fig. 13 for 3KEQ and Fig. 25 and Fig. 27 for 3KW1. Comparing the heating structures in each of the models, we can find that, in general, the peak intensity of the positive heating anomaly in 3KEQ is stronger than that in 3KW1 in most of the models. This difference between the intensities of heating anomalies in 3KEQ and 3KW1 reflects the difference between the intensities of the positive precipitation anomalies in 3KEQ and 3KW1 (see Fig. 5 and Fig. 20). We also see the vertical structures of heating in the two SST settings are roughly similar in most of the models. A few differences we can point out may be listed as follows. The heating profile in LASG is vertically two-peaked for 3KEQ but is one-peaked for 3KW1, and heating in the lower troposphere in ECMWF05 is more intense for 3KW1 than for 3KEQ. Fig. 30

6. Summary and remarks

Varieties of precipitation and circulation structures that appear in response to a localized (3KEQ and 1KEQ) and a planetary scale SSTA (3KW1) superposed on a zonally homogeneous SST (CONTROL) in the 15 AGCMs participating the APE have been described and compared. We have examined only the time mean response defined as the difference of the temporal average of the atmospheric state for an SSTA from that for the corresponding CONTROL run.

6.1 Characteristics of the response to the SSTAs in the APE

a. The response to a localized SSTA

Gross features of the anomalies that appear in all of the models in common as the response to the localized equatorial warm SSTA found in the 3KEQ experiment can be summarized as below. (i) a distinct positive precipitation anomaly, whose amplitude exceeds twice the mean precipitation at the equator in the corresponding CONTROL run, develops over the SSTA. On the other hand, weak but widespread negative anomaly appears on the ITCZ outside the SSTA. Corresponding to the positive precipitation anomaly, a positive heating anomaly develops over the SSTA, and it is mostly distributed in the upper half of the troposphere in most of the models. (ii) the divergent flow from the heating anomaly forces a pair of intense upper tropospheric anticyclones at the subtropical latitudes to the north and south of the precipitation anomaly. Influenced by the strong westerly jets invading to the latitudes near the equator, the anticyclones extend eastward. (iii) disturbed by the flow associated with the anticyclones, the Kelvin wave response expected to the east of the positive precipitation anomaly is almost completely obscured. The baroclinic equatorial Rossby wave response expected to the west is also weak or absent presumably because of the very small value of absolute vorticity contributed by the anticyclonic shear on the equatorward sides of the westerly jets mentioned above. As a result, the appearance of tropical response structure is very different from the structure that characterizes the standard framework of thermal response problem of Matsuno(1966) and Gill(1980). (iv) from the off-equatorial anticyclonic anomalies at the longitudes of the SSTA, equivalent barotropic Rossby wavetrains are emitted and propagate poleward, and are imediately refracted back to the tropical latitudes at around 10,000 km to the east of the SSTA, resulting in a distinct deep warm signal in the tropics which is partially separated from the warm region over the SSTA. The Rossby wavetrains further propagate eastward along the waveguides associated with the mid-latitude westerly jets. (v) the mid-latitude dynamical response described above induces non negligible precipitation anomalies mainly on the equatorward flanks of the westerly jets, which are composed of the negative anomalies around the longitudes of the SSTA and the positive anomalies to the east by latitudes of $50 \sim 100°$ and slight enhancement of the wavenumber 5 quasi-stationary features identified in the CONTROL experiment.

The variety of the responses found among the models can be summarized below. (i) the intensity, structure, and location of each element of the responses summarized above are considerably model dependent. The peak-to-peak amplitude of the precipitation anomaly at the equator varies over more than a factor of three, reflecting the variety of the meridional structure of the anomalies, each of which is basically inherited from the meridional structure of the ITCZ precipitation of the corresponding CONTROL run. The variety of the amplitudes of responses reduces when they are averaged meridionally over $\pm 15°$ latitudes from the equator that covers all of the equatorial precipitation anomaly, but still remains over more than a factor of two among the models. (ii) the vertical structures of the heating anomalies differ among the models, presumably reflecting the characters of particular convective cloud parameterizations used in the different models. (iii) the details in the structures of the precipitation anomalies over the equatorial region vary considerably, although they are common in sharing the dissimilarity to the standard Matsuno-Gill patern as mentioned previously. (iv) the intensities of the Rossby wavetrains vary over more than a factor of two, and to some extent vary according to the intensities of the precipitation anomalies averaged within ±15 degrees from the equator, suggesting that the Rossby waves are excited basically as a linear response to the heating anomaly over the SSTA. (v) the factors which control the intensity of the precipitation anomaly in different models are sought but are not successfully identified.

The intensities of the anomalies associated with the stronger localized equatorial SSTA (3KEQ) and those with the weaker SSTA (1KEQ) of the same shape in the corresponding models are compared. The results indicate that the intensities of the precipitation anomaly over the SSTA vary roughly in proportion to the intensity of the SSTA in each of the models. The intensity of the Rossby wavetrain also increases in each model as the intensity of the SSTA increases, but proportionality does not necessarily hold.

b. The response to the zonal wavenumber one SSTA

Gross features of the anomalies that appear in all of the models in common as the response to the wavenumber one variation of the equatorial SSTA found in the 3KW1 experiment can be summarized as below. (i) both of the precipitation and dynamical responses are characterized with the wavenumber one zonal variation. (ii) at the warm (cold) SST region, a zonally extensive positive (negative) precipitation anomaly appears. The amplitude of the anomaly is comparable to, or more than the zonal mean precipitation amount in the corrresponding CONTROL run. (iii) the vertical structure of the heating anomaly is strongly weighted to the upper troposphere in most of the models. (iv) in the upper troposphere, affected by the divergent wind from the precipitation anomaly, the region of small absolute vorticity extends poleward, whose longitudinal location is shifted eastward from the precipitation anomaly. Contrarily, in the cold SST region, the region of small absolute vorticity almost disapperars, and the subtropical westerly jets become weaker but more widespread, invading deep into the tropics almost to the equator. In the lower troposphere, low pressure anomaly develops to the east of the positive precipitation anomaly. (v) the upper tropospheric wind response at the equatorial precipitation maximum is dominated by zonal convergence and meridional divergence. In the low levels, convergence is dominated by the meridional component. These characteristics are, as in the response to the localized SSTA, distinctly different from those of the standard thermal response of the Matsuno-Gill pattern. (vi) dynamical responses in the lower and the higher latitudes exhibit contrasting vertical structure. Equatorward of the subtropical westerly jets, the response is baroclinic; in the warm SST region, upper (lower) level response is high (low) pressure, whereas in the cold SST region, upper (lower) level response is low (high) pressure. Poleward of the westerly jets, the response is barotropic; low (high) pressure response dominates in the longitudes of warm (cold) SST both in upper and in lower troposphere. (vii) associated with the mid-latitude dynamical response, variations of precipitation develop at the baroclinic zones, whose amplitude are about a half of the zonal mean precipitation in the corresponding CONTROL run. (viii) considerably westerly acceleration of zonal mean zonal wind is noted in the upper troposphere around the equator.

Less variety is found in the response to the wavenumber one SST variation, compared with the large variety found in the response to a localized SSTA. The variety of the response noted among the models can be summarized below. (i) the intensities of the precipitation anomalies near the equator vary almost over a factor of five, and the meridional distributions of the anomalies mostly reflect the structure of the ITCZ in the corresponding CONTROL run. The shape and the longitudinal phase of the precipitation anomalies vary significantly. The variety of the amplitudes reduces considerably when the anomalies are averaged meridionally within ±15 degrees from the equator that covers all of the equatorial precipitation anomalies, and the peak-to-peak amplitudes are typically 150% of the corresponding amounts in CONTROL. (ii) the intensities of the geopotential height anomalies over the subtropics and the high latitudes vary in a range of a factor of 2 among the models. Although similar range of variety exists in the amplitude of precipitation anomaly, no clear relationship can be noted between the precipitation and dynamical response amplitudes. (iii) the anomalies of zonal mean zonal wind in the upper troposphere vary over a factor of three, and can be related positively to the zonal momentum transport by stationary wave and negatively related to the intensities of mean equatorial precipitation intensity.

Comparing the responses of the participating models for the 3KEQ SSTA and those for the 3KW1 SSTA, it can be pointed out that each model responds to both SSTAs in a consistent manner. For example, the meridional structures of the equatorial precipitation anomalies are similar, and the models with more intense precipitation response for 3KEQ in comparison to the other models tend to exhibit more intense precipitation response also for 3KW1 in comparison to the other models.

6.2 Comments on the observed response to SSTA

The intensity and the horizontal extent of the SSTA in 3KEQ are not very different from those of the SSTA in the warm phase of El Nino, and those of 3KW1 are somewhat similar to those associated with climatological zonal variation of tropical SST over the indian and pacific oceans, so that it may be appropriate to give some comments on the response to SSTA observed in the real atmosphere.

During the warm phase of ENSO, the upper tropospheric geopotential anomaly is characterized with a pair of anticyclones in the subtropics about 50° longitude to the east of the peak equatorial SST anomaly and very weak Kelvin response as depicted in Fig.12a of Dima and Wallace (2007) for example (with sign reversed). These features are superficially similar to those established in the 3KEQ experiments. However, one should be cautious about the choice of a "basic state" reffering to which an "anomaly" is difined. As is shown in Fig.2a of Dima and Wallace for example, the climatology of upper tropospheric geopotential height is characterized with a pair of anticyclones aroound the longitudes of the maritime continent and a pair of deep troughs in the eastern pacific. On the other hand, as is shown Fig.13a of the same reference for example, the geopotential field in the tropics is almost zonally symmetric during the warm phase of ENSO. As a result, the structure of the "anomaly" in the warm phase is, in fact, the structure of the climatology with the signature reversed; the dynamics shaping the response of geopotential to the SSTA should be interpreted not with the situation during the warm phase but with the situation in the climatology in mind. Of course, in climatology, the pair of anticyclones are located to the west of the convection center. Another subtle feature of the response of real atmosphere to the SSTA of ENSO, which is not necessarily independent from the issue above, is that the enhancement of convection in the equatorial central Pacific during El Nono is accompanied with suppression of convection in the western Pacific presumably resulting from the cool SST anomaly (DeWeaver and Nigam, 2004, for example), which results in cancellation of positive and negative Kelvin responses. On the other hand, each of the precipitation responses to the 3KEQ SSTA in the APE models is much closer to a "monopole". In summary, the nature of the tropical response in 3KEQ in the present study should be regarded as being considerably different from the response structure that characterizes the "anomaly" during the warm phase of ENSO.

The structure of response to 3KW1 is also very differnt from that of the Walker circulation in the real atmosphere. As can be found in Fig.4 of Dima and Wallace(2007) for example, observed Walker cell is characterized with the divergent zonal wind around the maximum of precipitation. In contrast, as described in Section 5, zonal wind is convergent at the precipitation maxima in 3KW1. By separating the horizontal wind field into rotational and divergent components (not presented here), we can show that most of the zonal convergence/divergence along the equator is attributed to the rotational wind fields in both climatological state and 3KW1 result. In other words, the distinct difference between the observed Walker circulation and the response in 3KW1 originates mainly from the difference in the longitudinal phase of the Rossby response.

Bearing the considerable difference between the response to SSTA in 3KEQ and the anomaly associated with ENSO, and that between the response in 3KW1 and the observed Walker cell in mind, we consider that further quantitative comparison between the results obtained in this study and fetaures observed in the real atmosphere is not appropriate.

6.3 Remaining issues

As is stated in Section 1, since the focus of the present paper is to survey the results of AGCM experiments conducted with zonally varying SSTs in the APE, a number of interesting issues found during the execution of the survey have been described but are not pursued any further. These issues are summrized below.

As noted above, the structure of the response to the SSTA in the equatorial region is strongly affected by the intense upper tropospheric westerly wind due to the equatorward shift of the mid-latitude baroclinic jets in CONTROL compared to the real atmosphere (section 3). It is implied that the characteristics of the response to the SSTA of the APE can not necessarily be regarded as representative ones expected in "realistic" conditions. With this possibility in mind, it would be useful to conduct a small extension of the APE in which the same anomalies of SST are placed on a series of different zonally uniform basic state SSTs, e.g., FLAT, QOBS, PEAKED, and CONTROL5N SST profile defined in the specification of the APE (Blackburn and Hoskins,2012). Such extended series of experiments will strengthen the applicability of the SSTA response experiments of the APE to the real atmosphere. We conducted a preliminary study on such a series of experiment with one of the participating models of the APE, and have found the responses to the 3KEQ SSTA is considerably different from those described here. The results will be reported elsewhere.

We have not examined the dynamical structure of the positive rainfall anomaly that develop over the localized SSTA in detail. Nor we could identify the factors that determine the distribution and intensity of the precipitation anomaly in the models with confidence. Considering the diversity of the gross responses of precipitation and other variables (e.g., Fig 15 and 16), understanding the issue of direct response requires more careful analyses of the parameterization tendency, not only that of cumulus parameterization but also those of boundary layer processes, radiation, etc. Even with such more comprehensive datasets, feedbacks and interactions among various kinds of atmospheric processes might make achievemnt of understanding the issue a difficult task. For example, preliminary survey of time series of precipitation shows that the precipitation anomaly emerges as the increase of activity of precipitating disturbances like demonstrated in a previous study (Hosaka et al. 1998), suggesting that we have to analyze not only the stationary features but also transient components to understand the mechanism of the development of the precipitation anomaly over the SSTA. Model with higher resolution (e.g., Yoshioka and Kurihara,2008) would also be informative.

We have pointed out that there are several types of precipitation anomalies outside the region of the SSTA, which are the negative anomaly along ITCZ outside the SSTA in 3KEQ, the east-west dipoles at the equatorward flank of baroclinic zones in 3KEQ and 3KW1, and the mid-latitude wavenumber 5 variation that also affects the rainfall along the ITCZ. These are presumably indirectly induced as the remote dynamical responses forced by the precipitation anomaly over the SSTA. Examination of the generation mechanism of them, e.g., what kind of dynamical features are involved, how particular precipitation anomalies are induced, etc., are left for future research. This could be a difficult task due to complex interaction among various processes in the model. One method that could be useful is to examine the time-dependent response (e.g. Jin and Hoskins, 1995), namely in an ensemble experiment (Toyoda *et al.*, 1999; Nakajima *et al.*,2004). More detailed analysis of wave propagation would also be useful using the wave activity diagnosis of Takaya and Nakamura (2001). Analysis on the transient disturbances mentioned earlier would also be useful for this purpose.

The mechanisms that produce the model dependence in the subtropical and extratropical responses to the SSTA are also left unsolved. It is probable that both the variety of the patterns and intensities of the heating anomalies above the SSTA and the varieties of the structure of zonal mean state of the atmosphere in different models contribute to the emergence of the variety in the response outside the tropics. As for the response to the localized SSTA (3KEQ), we have tried a limited examination of the origin and propagation characteristics of the Rossby wavetrain in only one of the models (Appendix A). Such analysis must be repeated for the rest of the models to grasp the variety of the behaviors of waves among the models. As for the response to the wavenumber one SST variation (3KW1), preliminary analysis suggests that the influence of the eastward advection by strong westerly wind rather than westward propagation as Rossby wave is important. A series of analysis on the modification of storm tracks by the surface conditions like in Inatsu *et al.* (2002) or Sampe *et al.* (2012, this issue) should be applied to investigate the mechanism of the response. The effects of transient waves also should be investigated. These issues are also left for future studies.

We did not touch the properties and model dependence of transient disturbances in the presence of the SSTA. The space time spectra of precipitation and OLR presented in the APE-ATLAS (Williamson et al. 2012a) exhibit both considerable variety among the models and a large degree of change responding to the SSTA, namely 3KW1, suggesting the presence and the variety of the response of the transient disturbances. Analysis of composite structures of precipitation such as done by Nakajima *et al.* (2012) for the experiments with the CONTROL SST profile would be useful to elucidate the response of transient disturbances. The analysis of these points is worth doing, particularly because behavior of such disturbances may be important in shaping the stationary response structure. Unfortunately, datasets required for such analysis are not collected in the experiments with SSTAs. Full analysis of transient disturbances awaits the next attempt of APE project with more complete collection and archive of data.

Appendix A:

Behavior of Rossby waves in a 3KEQ experiment

In this appendix, we briefly examine the behavior of stationary Rossby waves in 3KEQ. and demonstrate that the upper tropospheric low latitude response that develop in response to the SSTA of 3KEQ has characteristics quite different from those of the thermal response problem of Matsuno(1966) and Gill(1980). We examine the 3KEQ GFDL model as a clear example;

the results presented below can be applied commonly to all of the APE models in a gross sense.

The propagation characteristics of Rossby waves can be conveniently represented by the wave activity flux derived by Takaya and Nakamura (2001) in the quasi-geostrophic approximation, and the excitation of Rossby waves can be represented by the Rossby wave sources (or vorticity sources) defined by Sardeshmukh and Hoskins (1988), whose definition is summarized in Appendix B. Calculation of the wave activity flux requires a specification of zonally uniform basic zonal flow. We employ the zonal and temporal mean zonal wind in the CONTROL run of the same model as the basic flow. Fig. 31

Figure 31 shows the horizontal component of the wave activity flux vector superposed and the contour diagram showing the distribution of Rossby wave source at 250 hPa surface. In order to save space, only the northern hemisphere is shown; the structure of the wave behavior is mostly symmetric about the equator (not shown here). Low latitude region where the flux can not be suitably defined is also omitted. We observe that a strong anticyclonic (negative) vorticity source exists around $(\lambda, \varphi) = (0°, \pm 23°)$, where the wave activity flux emerge and propagate northeastward. The vorticity source consists mainly of the advective source (see Appendix C for the definition) that results from the meridionally directed divergent wind, whose origin is the precipitation anomaly above the SSTA, flowing on the steep gradient of absolute vorticity near the westerly jet. There are two additional areas of intense vorticity sources; one is the cyclonic (positive) vorticity source around $(\lambda, \varphi) = (15°, \pm 35°)$, and another is the anti-cyclonic source around $(\lambda, \varphi) =(70°, \pm 32°)$. These sources are mainly contributed by the divergent source related to the vertical motion associated with the wind flowing around the anticyclone centered at $(\lambda, \varphi) \sim (50°, \pm 45°)$ (see Fig. 6(h)) in the baroclinic zone, and should be interpreted as showing the vertical propagation of Rossby waves rather than the "true sources"; the vertical component of wave activity flux in the middle troposphere (not shown here) exhibits significant downward (upward) flux at the location of the convergence of wave activity flux.

Overall picture is that the Rossby wavetrain is excited at the equatorward flank of the westerly jet at the longitude of the SSTA and propagates eastward along the waveguide in the westerly jet meandering in the 20–40 degrees latitudinal band (Hoskins and Ambrizzi, 1993). The feature of the Rossby waves in 3KEQ is in distinct contrast with that in the standard Matsuno-Gill thermal response as can be summarized as follows: First, Rossby wave is excited at fairly high latitudes (Fig. 31), and it propagates *eastward* affected by the Doppler shift unlike the equatorial Rossby wave in Matsuno-Gill response which propagate *westward*. The anticyclonic anomaly that develops as the direct effect of the vorticity source also extends eastward, so that the wind field near the equator to the east of the SSTA is strongly disturbed, and the Kelvin response, which would dominate in usual Matsuno-Gill response, is almost completely eliminated (Fig. 6 $\sim$ Fig. 9). Second, the equatorial Rossby wave that would appear in Matsuno-Gill framework is excited only weakly. This is because the absolute vorticity is very weak in the tropical upper troposphere in CONTROL (Fig. 2(h)). The reason for both of the behaviors above is the significant invasion of westerly jets, being as strong as 50 m s^{-1} at the latitudes of the Rossby wave source, resulting in a significant anticyclonic shear to the low latitudes in the 3KEQ experiment of the APE.

Appendix B:
Definition of Rossby Wave Sources

Sardeshmukh and Hoskins (1988) pointed out that, in the absence of friction, the conservation equation of the vertical component of absolute vorticity ζ can be written as

$$\left(\frac{\partial}{\partial t} + \mathbf{v}_\psi \cdot \nabla\right)\zeta = S_{ad} + S_{div}, \tag{5}$$

where S_{ad} and S_{div} are the advective and the divergent sources of vorticity, respectively, which are defined as

$$
\begin{aligned}
S_{ad} &\equiv -\mathbf{v}_{\chi} \cdot \nabla \zeta, &(6)\\
S_{div} &\equiv -\zeta D, &(7)
\end{aligned}
$$

where ζ is absolute vorticity, D is divergence; $\mathbf{v}_{\chi}$ and $\mathbf{v}_{\psi}$ are divergent and rotational component of wind, respectively.

S_{ad} and S_{div} are calculated by the following procedure: First, ζ and D are calculated from the time mean wind field. Second, stream function, ψ, and velocity potential, χ, are obtained from vorticity and divergence, respectively. The inversion of spherical Laplacian operator is conducted employing the spectral method. Third, rotational and divergent components of wind vectors are obtained by differentiating the stream function and velocity potential, respectively. Forth, advective and divergent source terms are calculated by using (6) and (7) and the divergent wind vector and the vorticity.

Acknowledgements

The authors deeply thank two anonymous referees for carefully reading the several versions of manuscripts and a number of their critical and constructive comments that helped the authors improve the original manuscript substantially. Kind advice from Hisashi Nakamura is also acknowledged. Stimulative and encouraging discussions with Drs. M. Blackburn and D. L. Williamson were the great pabulum to accomplish this work. Numerical integration of AGU model were performed at the Earth Simulator Center. Shin-ichi Takehiro helped the authors in the preparation of many of the figures. Analysis software and local computational environments were constructed by the use of the resources of GFD-DENNOU-CLUB, including GPhys, spmodel, and DCL. This work was supported by Grants-in-Aid(B) for Scientific Research (12440123 and 21340139).

References

Alexander, M. A., I. Bladé, M. Newman, J. R. Lanzante, N.-C. Lau, and J. D. Scott, 1997: The atmospheric bridge: The influence of enso teleconnections on air-sea interaction over the global oceansstationary rossby-wave propagation in a baroclinic atmosphere. *Q. J. R. Meteorol. Soc.*, **123**, 919–928.

Bjerknes, J., 1969: Atmospheric teleconnections from the equatorial pacific 1. *Mon Wea. Rev.*, **97**, 163–172.

Blackburn, M., and B. J. Hoskions, 2012: Context and aims of the aqua planet experiment. *J. Meteor. Soc. Japan*, **APE Special Issue**, submitted.

Blackburn, M., D. L. Williamson, K. Nakajima, W. Ohfuchi, Y. O. Takahashi, Y.-Y. Hayashi, H. Nakamura, M. Ishiwatari, J. McGregor, H. Borth, V. Wirth, H. Frank, P. Bechtold, N. P. Wedi, H. Tomita, M. Satoh, M. Zhao, I. M. Held, M. J. Suarez, M.-I. Lee, M. Watanabe, M. Kimoto, Y. Liu, Z. Wang, A. Molod, K. Rajendran, A. Kitoh, and R. Stratton, 2012: The aqua planet experiment (APE): CONTROL SST simulation. *J. Meteor. Soc. Japan*, **APE Special Issue**, in press.

DeWeaver, E., and S. Nigam, 2004: On the forcing of enso teleconnections by anomalous heating and cooling. *J. Climate*, **17**, 3225–3253.

Dima, I. M., and J. M. Wallace, 2007: Structure of the annual-mean equatorial planetary waves in the era-40 reanalyses. *J. Atmos. Sci*, **64**, 2861–2880.

Gill, A. E., 1980: Some simple solutions for heat-induced tropical circulation. *Q. J. R. Meteorol. Soc.*, **106**, 447–462.

Hoerling, M. P., and A. Kumar, 2002: Atmospheric response patterns associated with tropical forcing. *J. Climate*, **15**, 2184–2203.

Hosaka, M., M. Ishiwatari, S. Takehiro, K. Nakajima, and Y.-Y. Hayashi, 1998: Tropical precipitation patterns in response to a local warm SST area placed at the equator of an aqua planet. *J. Meteor. Soc. Japan*, **76**, 289–305.

Hoskins, B. J., and T. Ambrizzi, 1993: Rossby wave propagation on a realistic longitudinally varying flow. *J. Atmos. Sci*, **50**, 1661–1671.

Hoskins, B. J., and D. J. Karoly, 1981: The steady linear response of a spherical atmosphere to thermal and orographic forcing. *J. Atmos. Sci*, **38**, 1179–1196.

Jin, F., and B. J. Hoskins, 1995: The direct response to tropical heating in a baroclinic atmosphere. *J. Atmos. Sci*, **52**, 307–319.

Kraucunas, I., and D. L. Hartmann, 2005: Equatorial superrotation and the factors controlling the zonal-mean zonal winds in the tropical upper troposphere. *J. Atmos. Sci*, **62**, 371–389.

Lindzen, R. S., and S. Nigam, 1987: On the role of sea surface temperature gradients in forcing low-level winds and convergence in the tropics. *J. Atmos. Sci*, **44**, 2418–2436.

Liu, Z., and M. Alexander, 2007: Atmospheric bridge, oceanic tunnel, and global climatic teleconnetions. *Rev. Geophys.*, **45**, RG2005.

Matsuno, T., 1966: Quasi-geostrophic motions in the equatorial area. *J. Meteor. Soc. Japan*, **44**, 25–42.

Nakajima, K., E. Toyoda, M. Ishiwatari, S. Takehiro, and Y.-Y. Hayashi, 2004: Initial development of tropical precipitation patterns in response to a local warm SST area: An aqua-planet ensemble study. *J. Meteor. Soc. Japan*, **82**, 1483–1504.

Nakajima, K., Y. Yamada, Y. Takahashi, M. Ishiwatari, W. Ohfuchi, and Y.-Y. Hayashi, 2012: The variety of spontaneously generated tropical precipitation patterns found in APE results. *J. Meteor. Soc. Japan*, **APE Special Issue**, in press.

Neale, R. B., and B. J. Hoskins, 2000a: A standard test for AGCMs including their physical parametrizations: I: The proposal. *Atmos. Sci. Lett.*, **1**, 101–107.

Neale, R. B., and B. J. Hoskins, 2000b: A standard test for AGCMs including their physical parametrizations. II: Results for the met office model. *Atmos. Sci. Lett.*, **1**, 108–114.

Sardeshmukh, P. D., and B. J. Hoskins, 1985: Vorticity balances in the tropics during the 1982-83 El Niñio-Southern oscillation event. *Q. J. R. Meteorol. Soc.*, **111**, 261–278.

Sardeshmukh, P. D., and B. J. Hoskins, 1988: The generation of global rotational flow by strady idealized tropical divergence. *J. Atmos. Sci*, **45**, 1228–1251.

Sobel, A., J. Nilsson, and L. M. Polvani, 2001: The weak temperature gradient approximation and balanced tropical moisture waves. *J. Atmos. Sci*, **58**, 3650–3655.

Takaya, K., and H. Nakamura, 2001: A formulation of a phase-independent wave-activity flux for stationary and migratory quasigeostrophic eddies on a zonally varying basic flow. *J. Atmos. Sci*, **58**, 608–627.

Toyoda, E., K. Nakajima, M. Ishiwatari, and Y.-Y. Hayashi, 1999: Response of the tropical atmosphere to a localized warm SST area: time-development observed in an aqua-planet ensemble experiment. *Nagare*, **18 (Nagare Multimedia 1999)**, http://www2.nagare.or.jp/mm/99/toyoda/index.htm.

Webster, P. J., 1983: The large scale structure of the tropical atmosphere. *General circulation of the atmosphere*, B. J. Hoskins and R. Pearce, Eds., Academic Press, 235–275.

Williamson, D. L., M. Blackburn, B. Hoskins, K. Nakajima, W. Ohfuchi, Y. O. Takahashi, Y.-Y. Hayashi, H. Nakamura, M. Ishiwatari, J. McGregor, H. Borth, V. Wirth, H. Frank, P. Bechtold, N. P. Wedi,

H. Tomita, M. Satoh, M. Zhao, I. M. Held, M. J. Suarez, M.-I. Lee, M. Watanabe, M. Kimoto, Y. Liu, Z. Wang, A. Molod, K. Rajendran, K. A., and R. Stratton, 2012a: *The APE Atlas. NCAR/TN-484+STR.* Natilnal Center for Atmospheric Research.

Williamson, D. L., M. Blackburn, K. Nakajima, W. Ohfuchi, Y. O. Takahashi, Y.-Y. Hayashi, H. Nakamura, M. Ishiwatari, J. McGregor, H. Borth, V. Wirth, H. Frank, P. Bechtold, N. P. Wedi, H. Tomita, M. Satoh, M. Zhao, I. M. Held, M. J. Suarez, M.-I. Lee, M. Watanabe, M. Kimoto, Y. Liu, Z. Wang, A. Molod, K. Rajendran, A. Kitoh, and R. Stratton, 2012b: The aqua planet experiment (APE): Response to changed meridional SST profile. *J. Meteor. Soc. Japan*, **APE Special Issue**, in press.

Yoshioka, M. K., and Y. Kurihara, 2008: Influence of the equatorial warm water pool on the tropical cyclogenesis: an aqua planet experiment. *Atmos. Sci. Lett.*, **9**, 248–254.

List of Figures

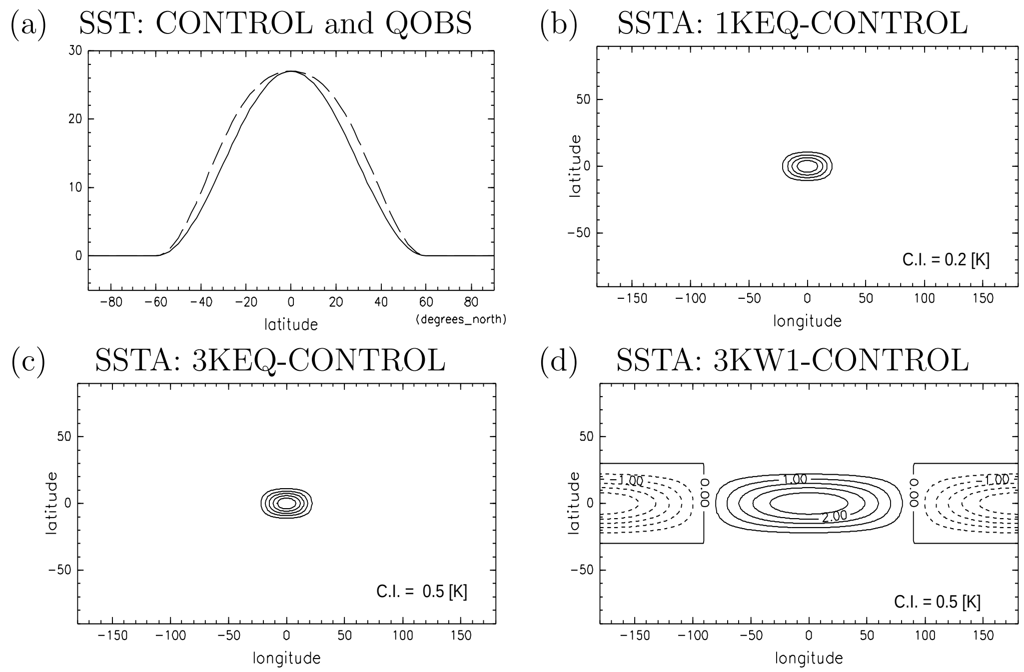

Fig. 1. (a) Specification of SST for CONTROL (solid) and QOBS (dashed), and SST anomalies from CONTROL for (b) 1KEQ, (c) 3KEQ, and (d) 3KW1, respectively. Unit is degree Celsius.

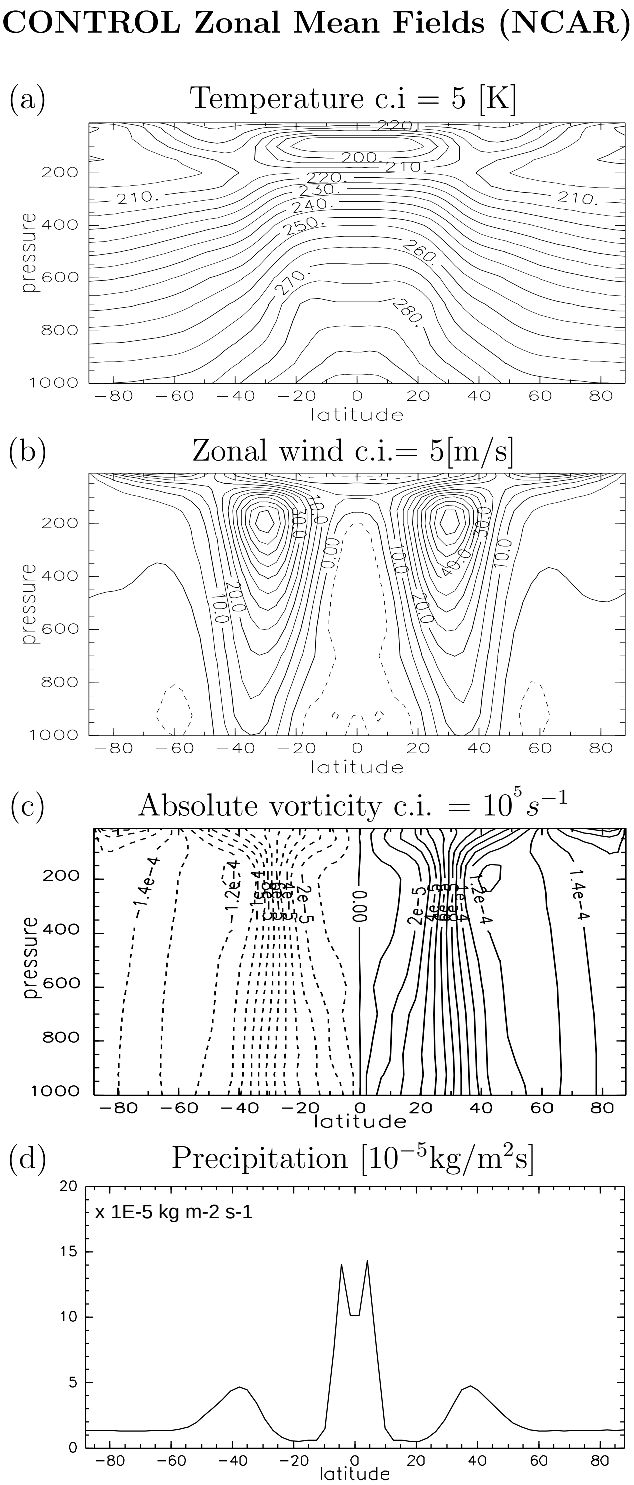

Fig. 2. Time and zonal mean fields obtained by the CONTROL run of NCAR. (a) temperature, (b) zonal wind, (c) absolute vorticity, and (d) precipitation. Unit and/or Contour interval are indicated at the top of each panel.

3KEQ Response (GFDL)

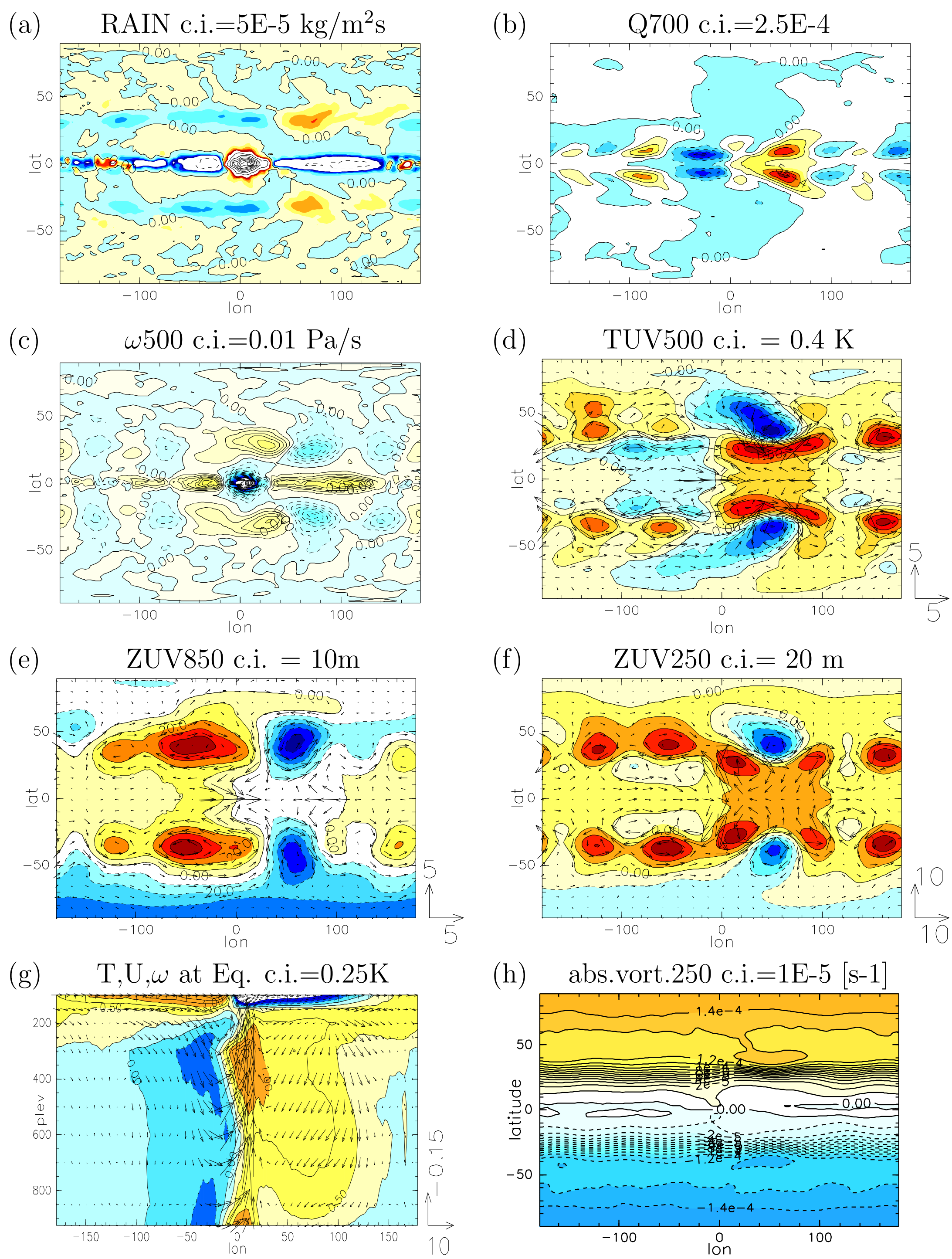

97

Fig. 3. Time mean response obtained by the 3KEQ run of GFDL. (a) horizontal distribution of precipitation anomaly, (b) water vapor mixing ratio anomaly at 700 hPa, (c) pressure velocity anomaly at 500 hPa, (d) temperature and horizontal wind anomalies at 500 hPa, (e) geopotential height and horizontal wind anomalies at 850 hPa, (f) geopotential height and horizontal wind anomalies at 250 hPa, (g) temperature, zonal wind, and vertical p-velocity anomalies at the equator, and (h) absolute vorticity at 250hPa. Unit and Contour interval are indicated

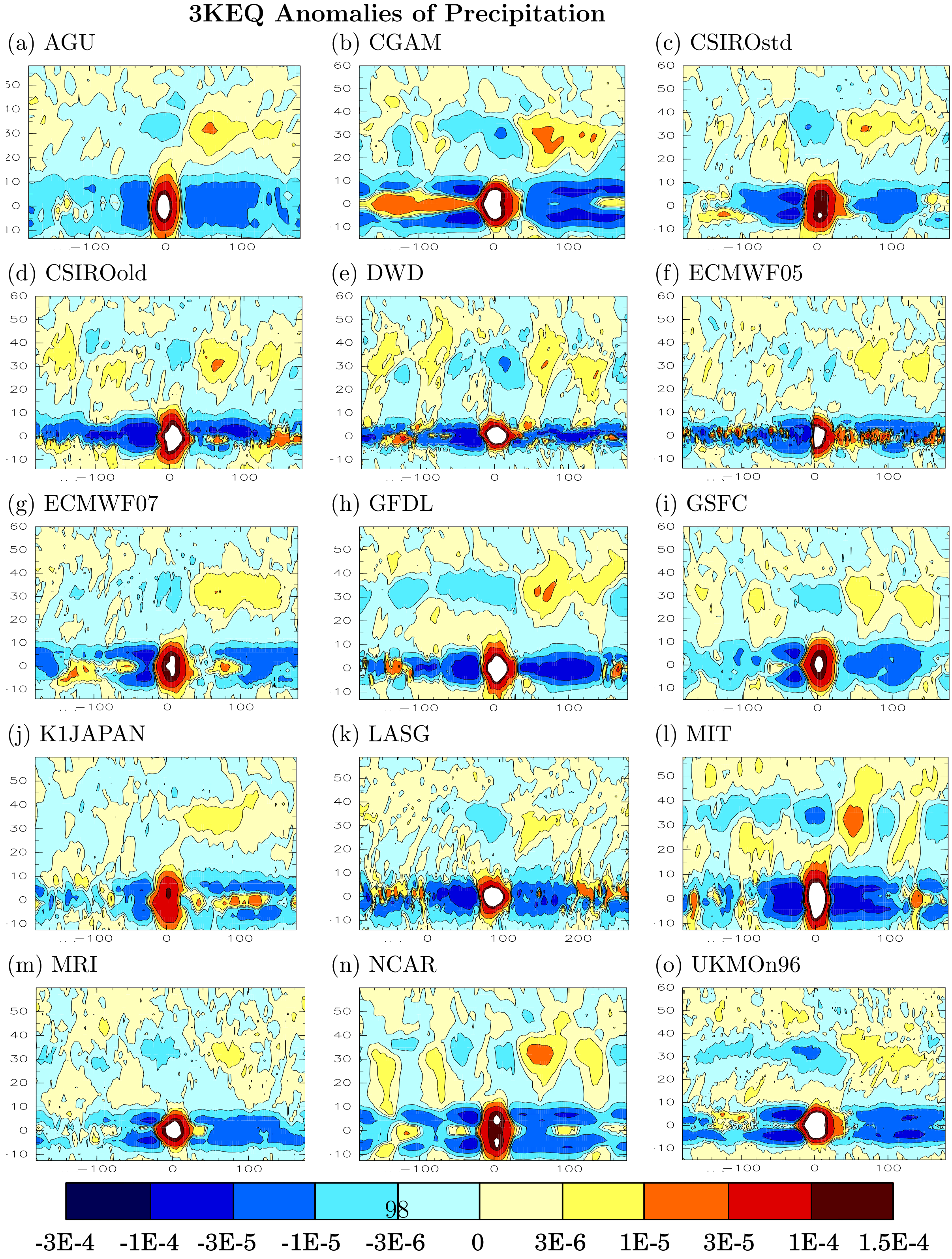

Fig. 4. Time mean precipitation anomalies in the 3KEQ runs of 15 APE models. Unit is kg/m^{2}s. Note that the polar region and most of the southern hemisphere are omitted. Note also that the region of precipitation higher than 1.5×10^{-4} kg/m^{2}s is not colored to enhance the position of precipitation maximum around the SSTA. See Table 1 for

3KEQ Responses of Precipitation at Selected Latitude Bands

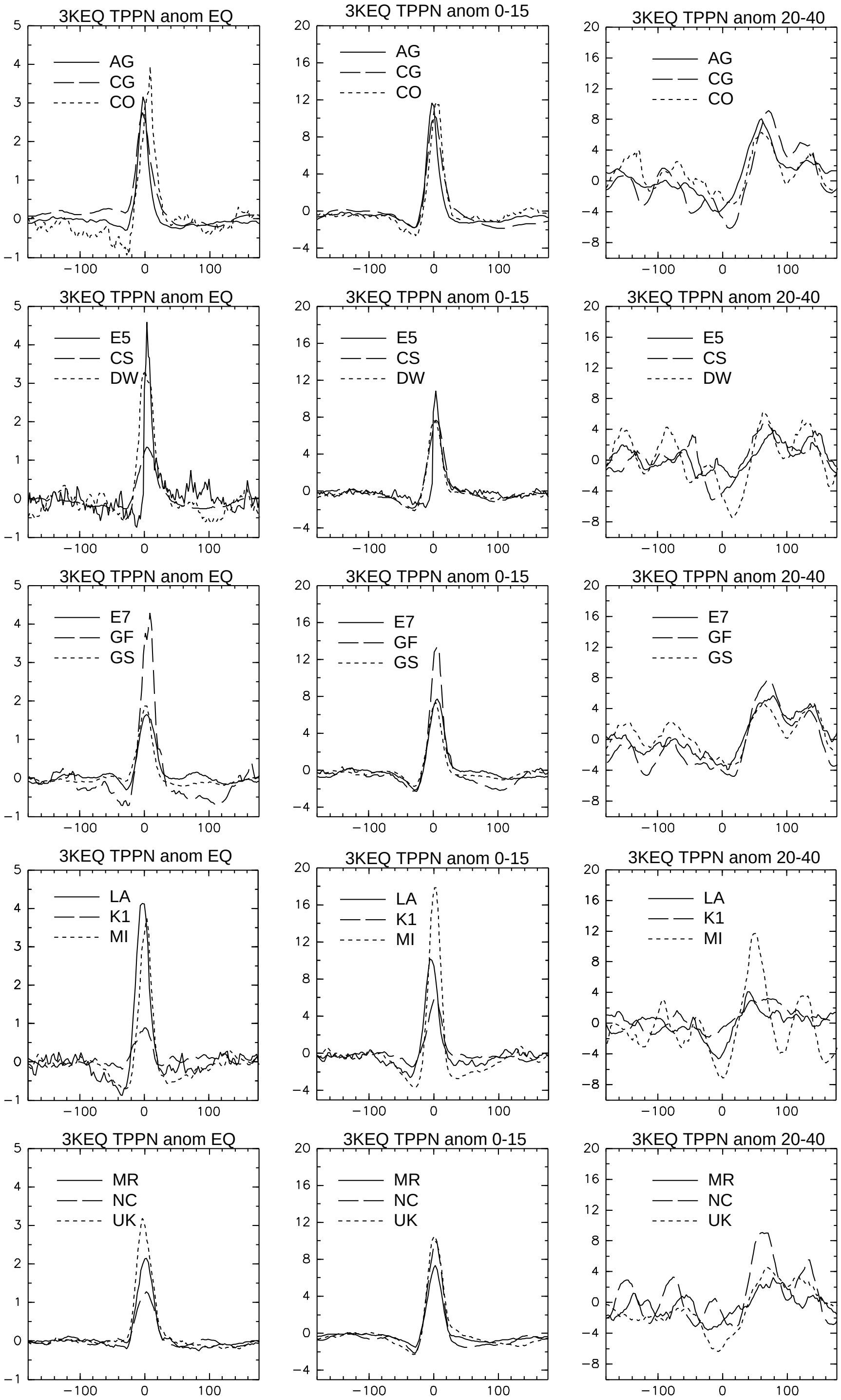

Fig. 5. Zonal distributions of precipitation responses at three selected latitudinal bands in the 3KEQ runs for 15 APE models. Left: raw values at the equator (unit:10^{-4}[kg m^{-2} s^{-1}]). Center: meridional averages over an equatorial band from $-15°$ to $15°$ (unit:10^{-5}[kg m^{-2} s^{-1}]). Right: meridional average over a mid-latitude band from $20°$ to $40°$ (unit:10^{-6}[kg m^{-2} s^{-1}]). See Table 1 for the legends of labels.

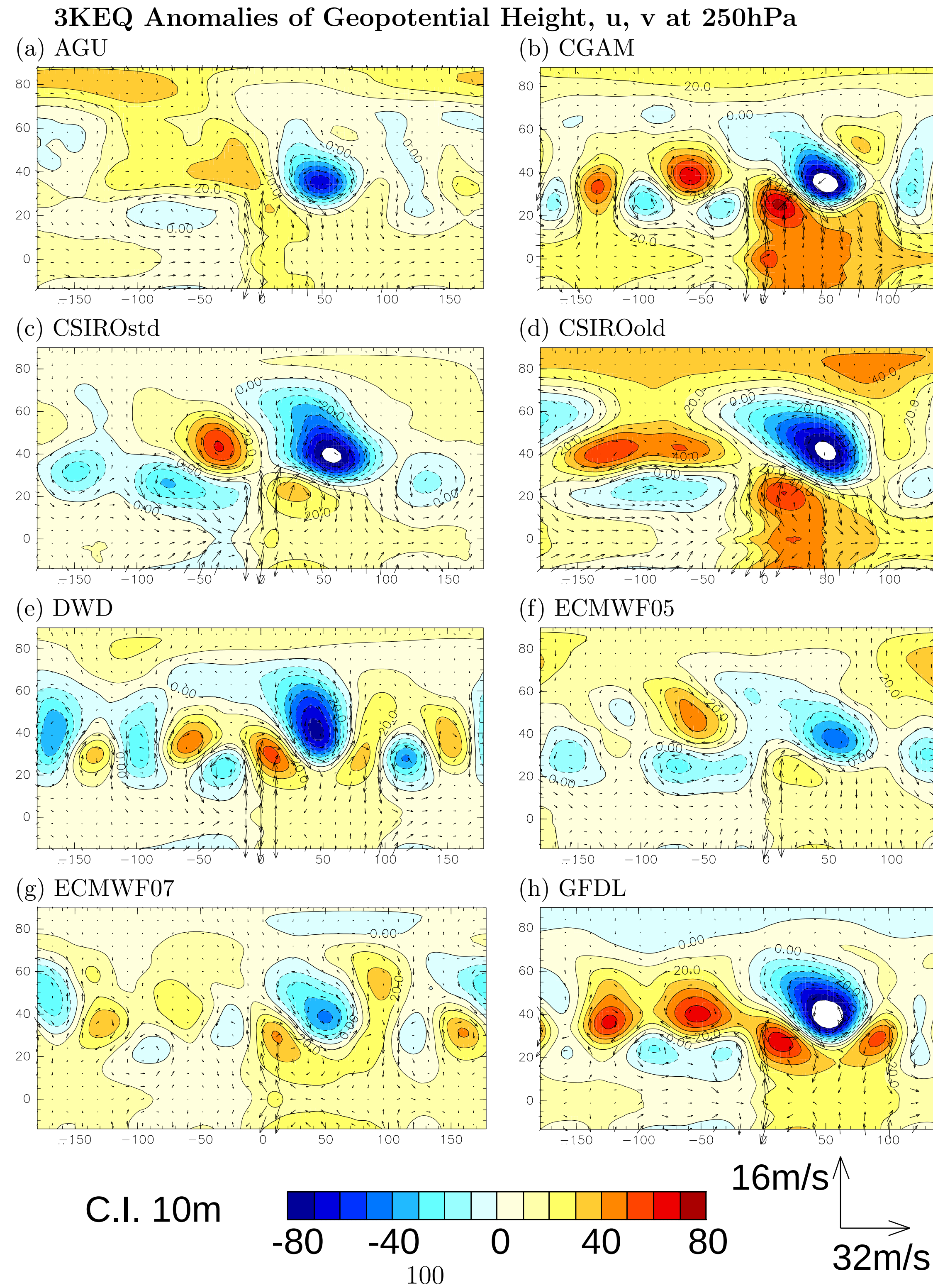

Fig. 6. Time mean anomalies of geopotential height and horizontal velocity vector at 250hPa in the 3KEQ runs of 15 APE models. Contour interval and magnitudes of wind vector components are indicated at the bottom.

See Table 1 for the legends of labels.

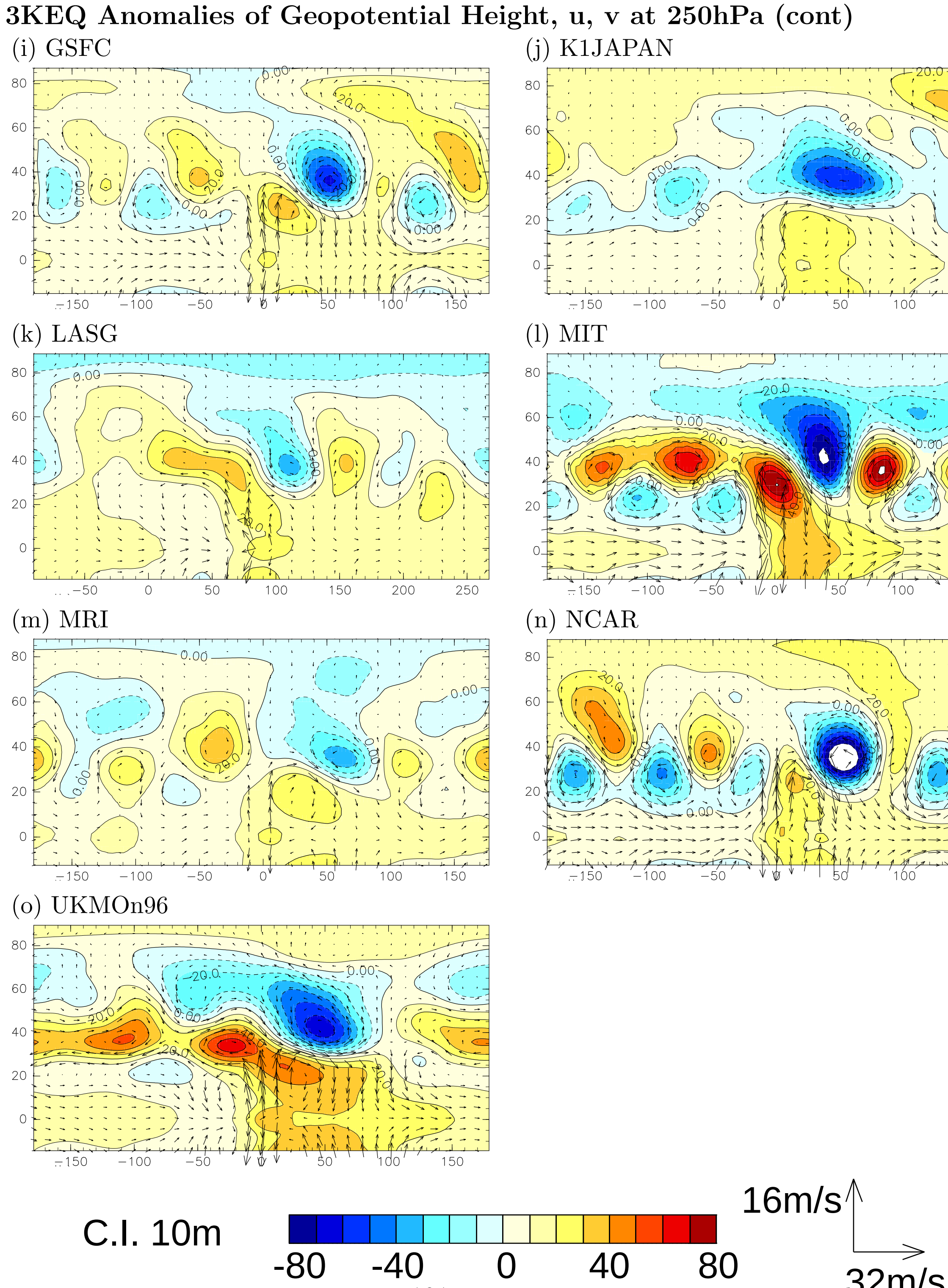

Fig. 7. (continued from Fig. 6)

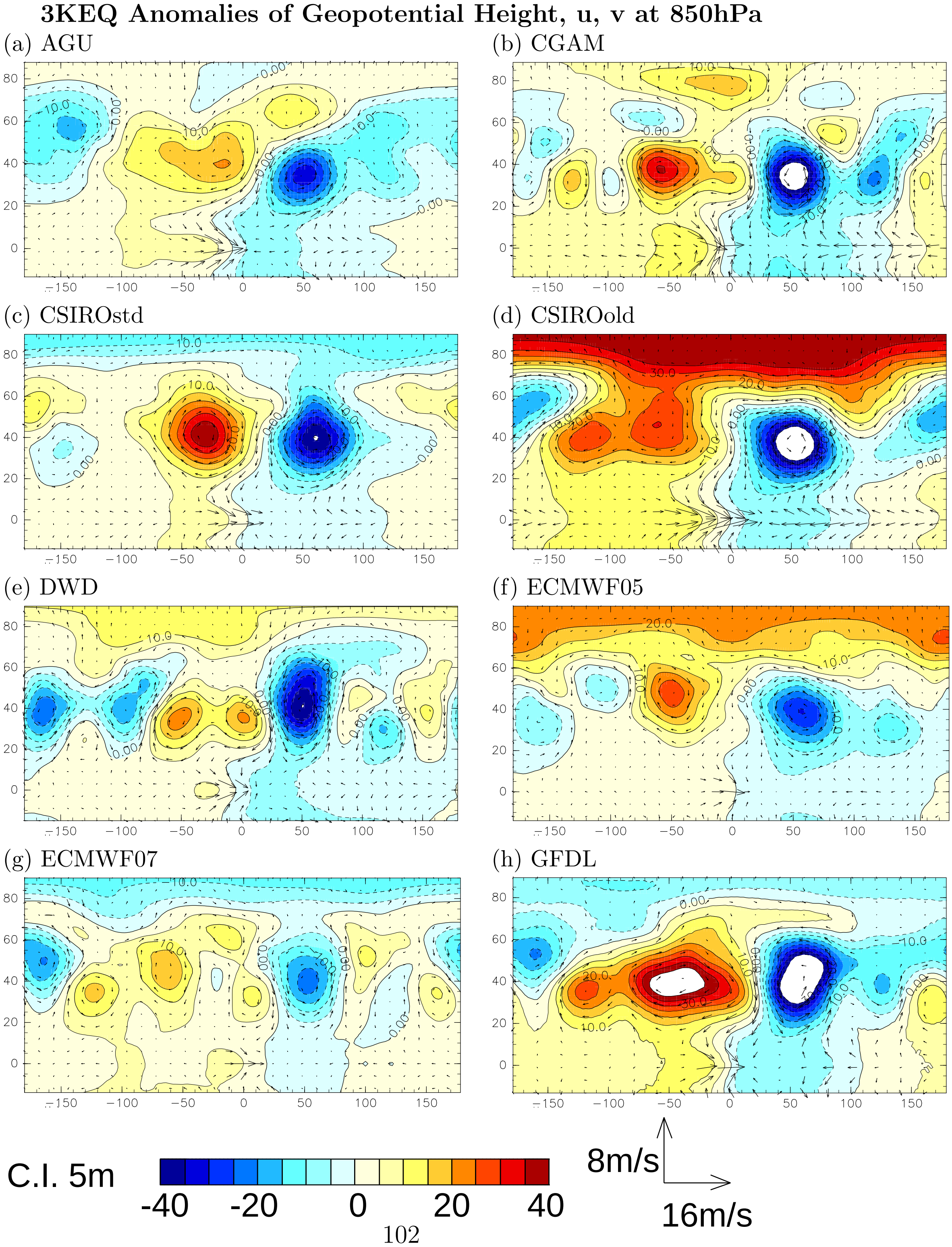

Fig. 8. Same as Fig. 6 but for 850hPa.

3KEQ Anomalies of Geopotential Height, u, v at 850hPa (cont)

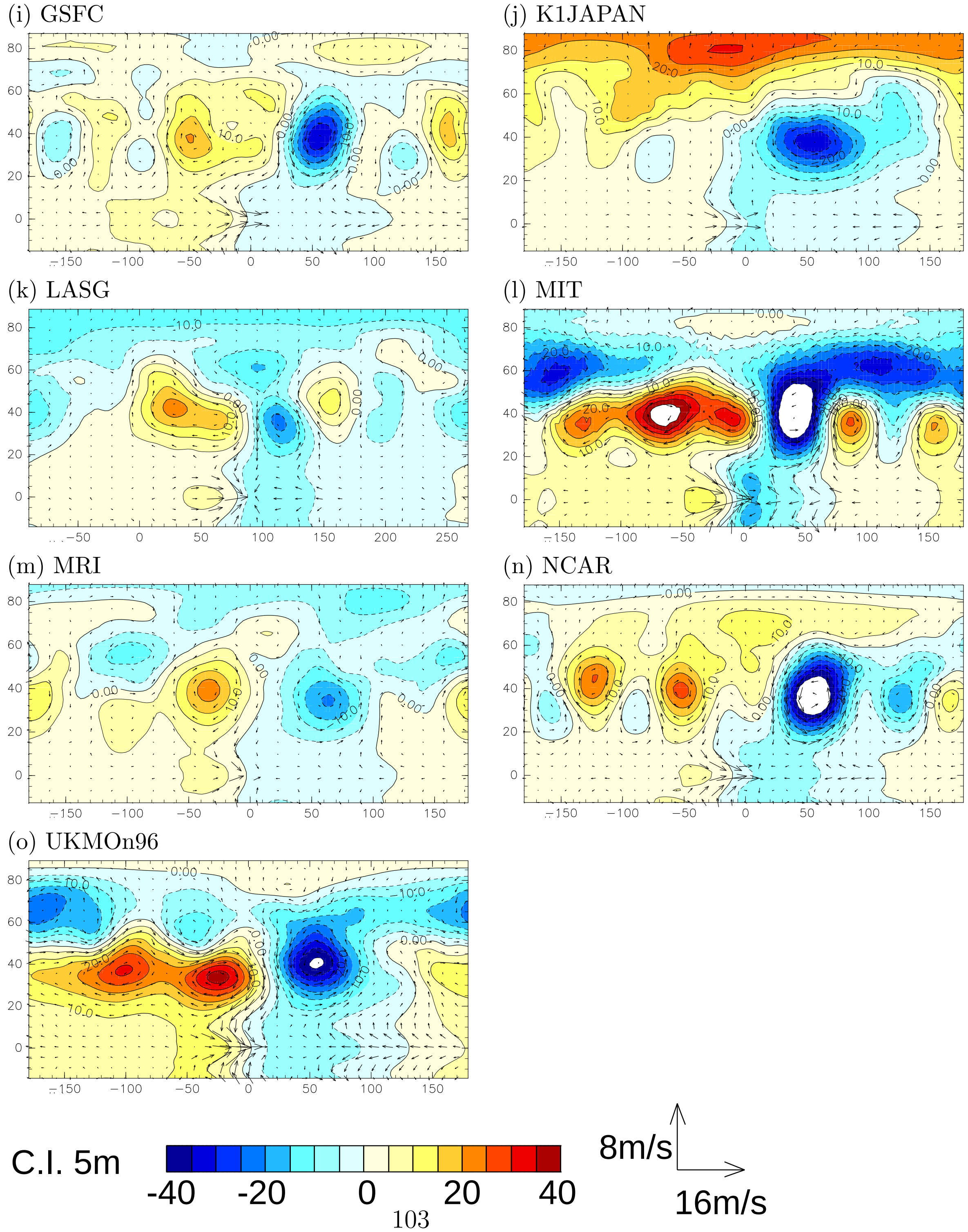

Fig. 9. (continued from Fig. 8)

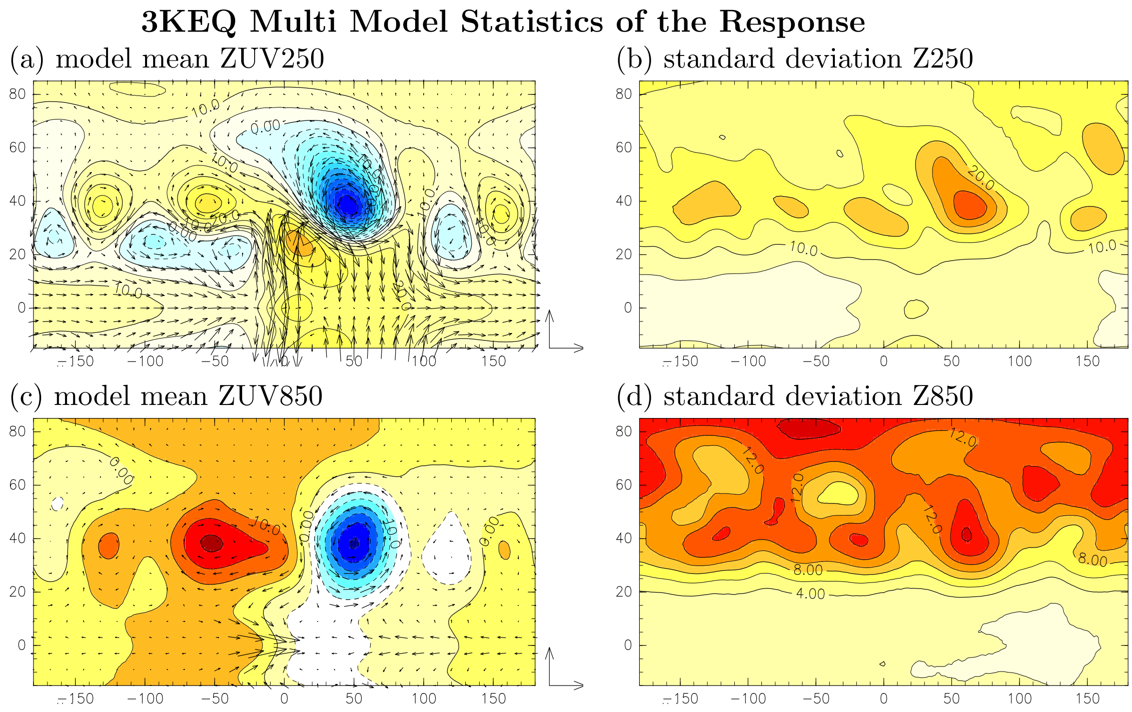

Fig. 10. Time mean anomalies of Multi model statistics of the response in the 3KEQ runs of 15 APE models. (a) Model averages of the temporal mean anomalies of geopotential height and horizontal velocity vector at 250hPa. Contour interval is 10m. The unit vectors of zonal and meridional wind are 16m/s and 8m/s, respectively. (b) The standard deviation of the temporal mean anomalies of geopotential height 250hPa. Contour interval is 5m. (c) Same as (a) but for 850hPa. Contour interval is 5m. The unit vectors of zonal and meridional wind are 8m/s and 4m/s, respectively. (d) Same as (b) but for 850hPa. Contour interval is 2m.

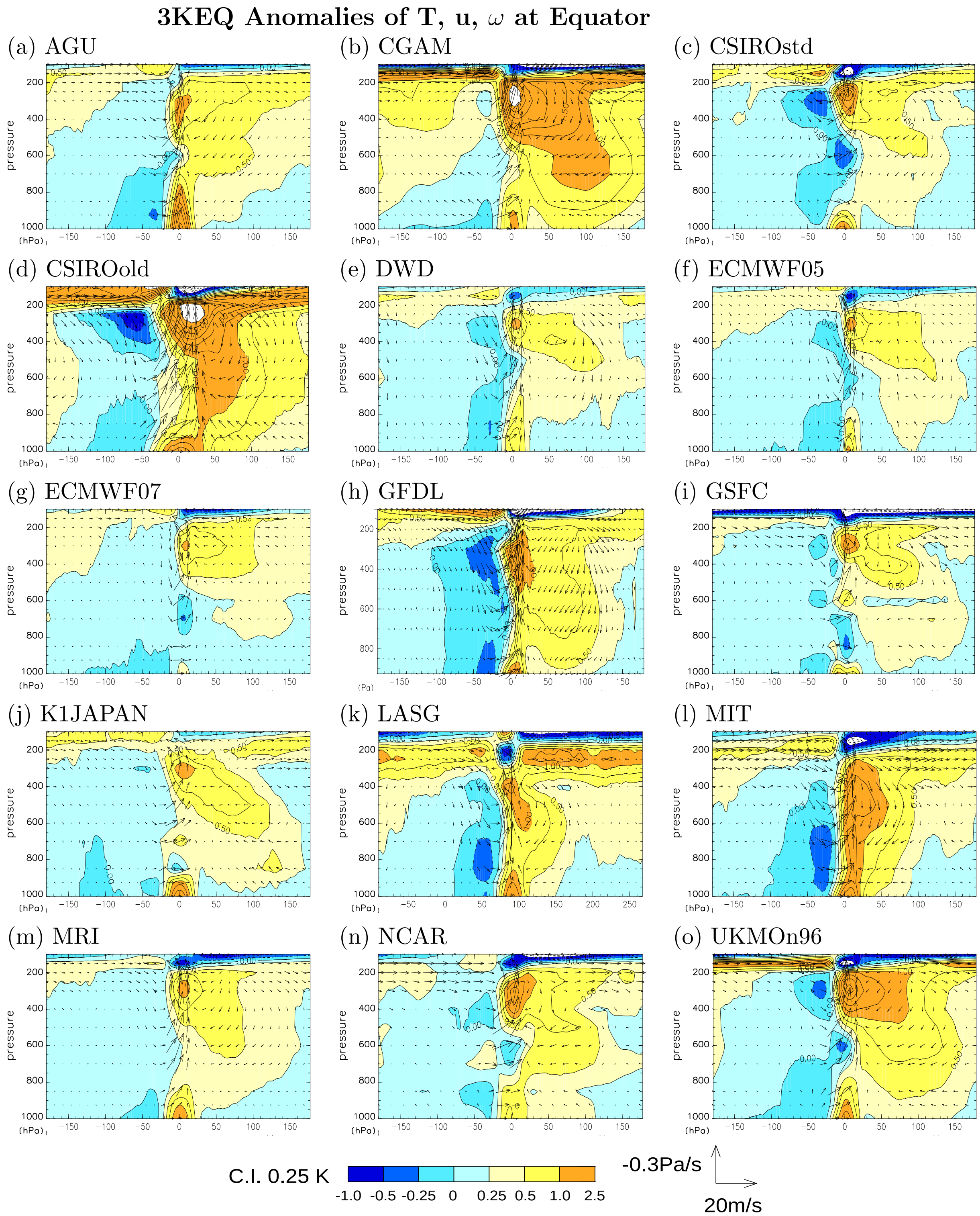

Fig. 11. Vertical distributions of time mean anomalies of temperature, zonal velocity, and p-velocity along the equator in the 3KEQ runs of 15 APE models. Contour interval and magnitudes of wind vector components are indicated at the bottom.

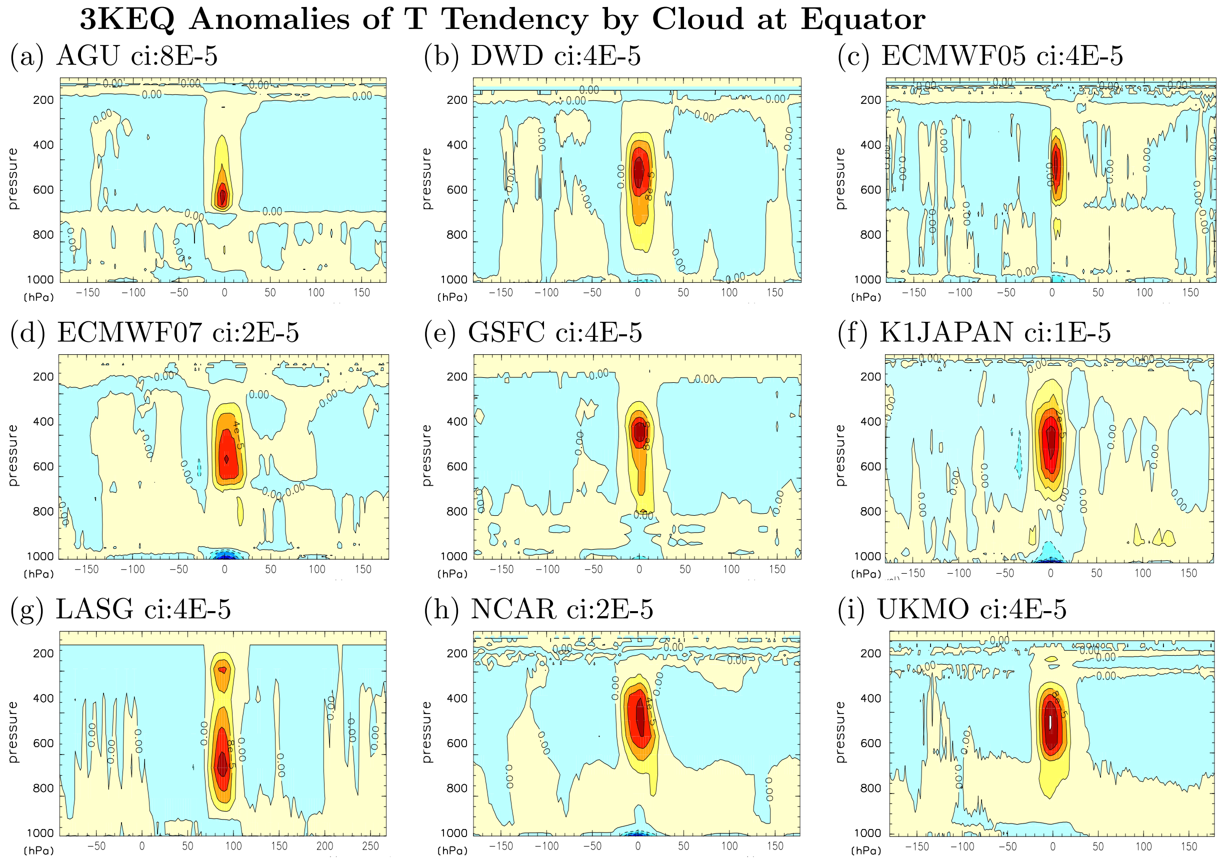

Fig. 12. Vertical distributions of time mean temperature tendencies at the equator in the 3KEQ runs of 15 APE models. Contour interval is indicated at the top of each panel. Vertical axis is pressure.

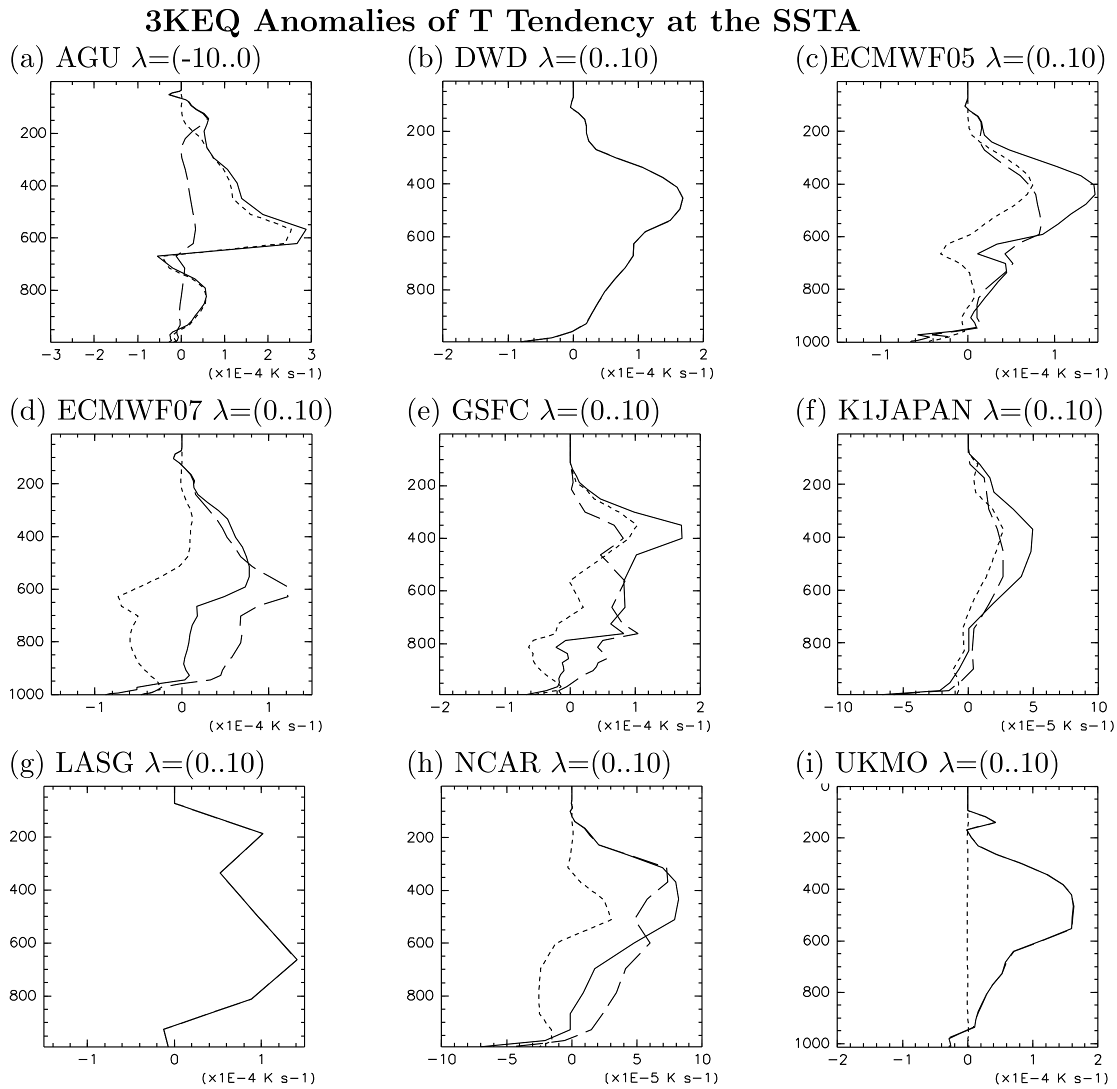

Fig. 13. Vertical profiles of time mean temperature tendencies at the SST anomaly in the 3KEQ runs of the 9 APE models from which data are provided. Unit is K s^{-1}. Vertical axis is pressure. Dotted and dashed lines indicate tendencies due to resolved clouds and due to parameterized convection, respectively, and solid line indicate the sum of the two. Note that heating due to resolved clouds is not available for DWD and LASG.

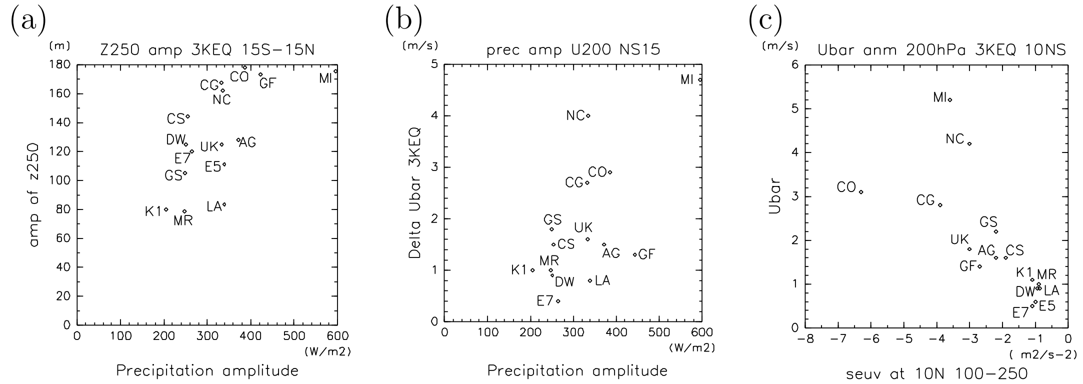

Fig. 14. Scatter plots concerning the dynamical response of the variables in the 3KEQ runs of 15 APE models. (a) The peak-to-peak amplitudes of the precipitation anomaly vs that of the geopotential height anomaly at 250hPa. (b) The peak-to-peak amplitudes of the precipitation anomaly vs zonal mean wind anomaly at 200hPa. Plotted values are those averaged over the equatorial latitudinal band within ±15°. (c) Poleward zonal momentum flux associated with stationary eddy at 10°N averaged for pressure levels between 100hPa and 250hPa vs zonal mean acceleration averaged within 10 degrees from the equator at 200hPa. See Table 1 for the legends of labels.

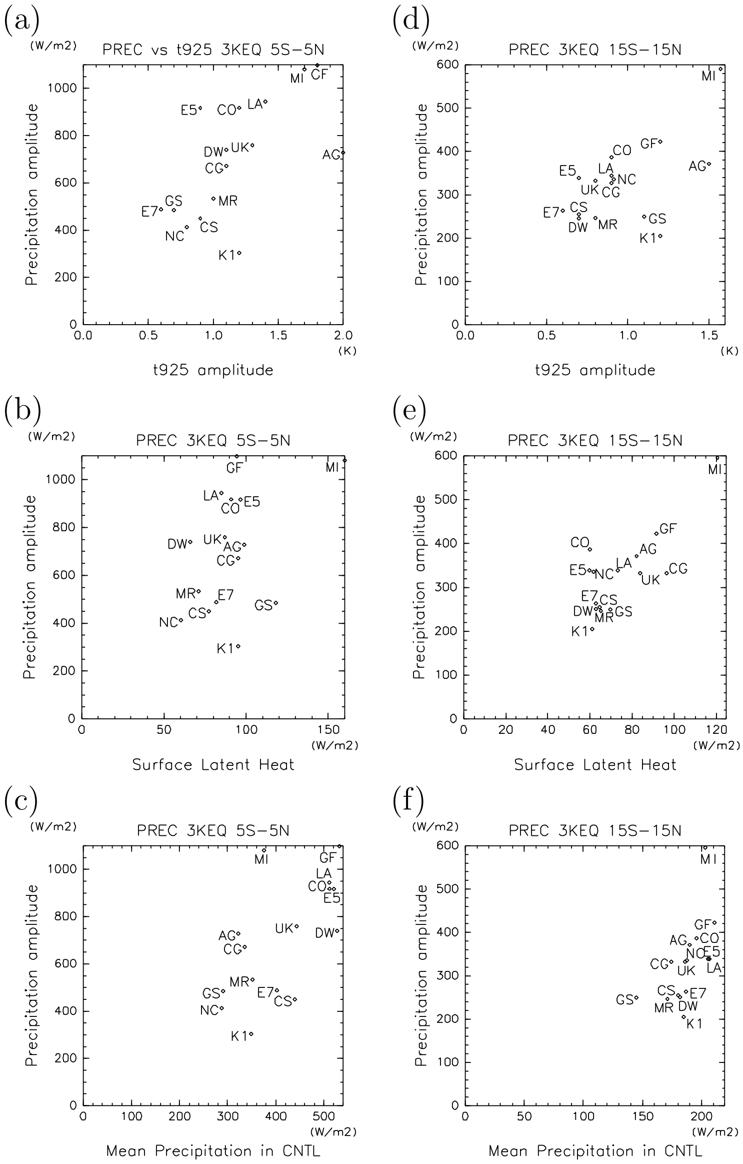

Fig. 15. Scatter plots of the peak-to-peak amplitudes of the precipitation anomalies and of the anomalies of several variables in the 3KEQ runs of 15 APE models. (a) Temperature anomaly at 925hPa versus precipitation anomaly, both of which are averaged within ±5° latitude band around the equator. (b) Same as (a) but for the latent heat flux anomaly. (c) Same as (a) but for the precipitation intensity in CONTROL. (d) Same as (a) but for the averages within 15 degrees from the equator. (e) Same as (b) but for the averages within 15 degrees from the equator. (f) Same as (c) but for the averages within 15 degrees from the equator. See Table 1 for the legends of labels.

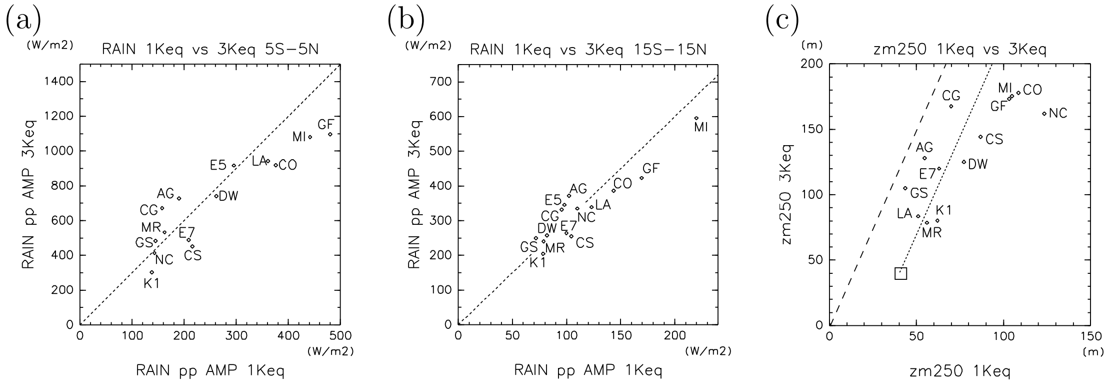

Fig. 16. Scatter plot comparing the peak-to-peak amplitudes of the anomalies in the 1KEQ and the 3KEQ runs of 15 APE models. (a) precipitation anomaly averaged within 5 degrees from the equator. (b) precipitation anomaly averaged within 15 degrees from the equator. (c) mid-latitude geopotential height anomaly. The dotted lines in (a) and (b) correspond to the relationship where the amplitudes in 3KEQ are three times those in 1KEQ. In (c), the broken line corresponds to the same relationship as above, whereas the dotted line corresponds to the similar relationship but the amplitudes in 3KEQ and 1KEQ have the common background value of 40 [m] noted by a square. See Table 1 for the legends of labels.

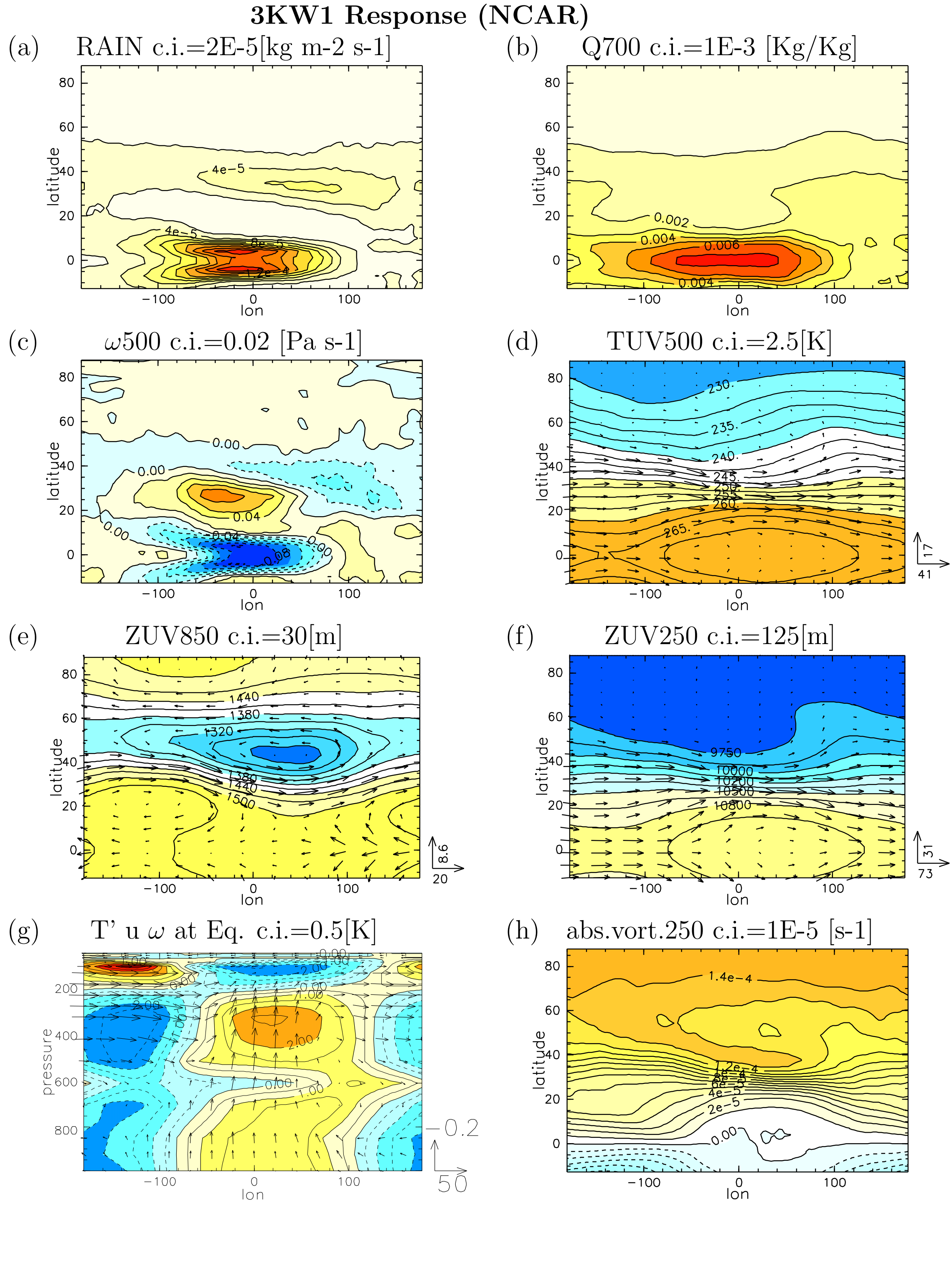

Fig. 17. Time mean response obtained by the 3KW1 run of NCAR. (a) horizontal distribution of precipitation, (b) water vapor mixing ratio at 700 hPa, (c) pressure velocity at 500 hPa, (d) temperature and horizontal wind at 500 hPa, (e) geopotential height and horizontal wind at 850 hPa, (f) geopotential height and horizontal wind at 250 hPa, (g) temperature deviation from zonal mean, zonal wind, and vertical p-velocity at the equator, and (h) absolute vorticity at 250hPa. Unit and Contour interval are indicated at the top of each panel. Magnitudes of the components of vector are indicated to the right of each panel. Units are

3KW1 Anomaly of Zonal Mean Zonal Wind (NCAR)

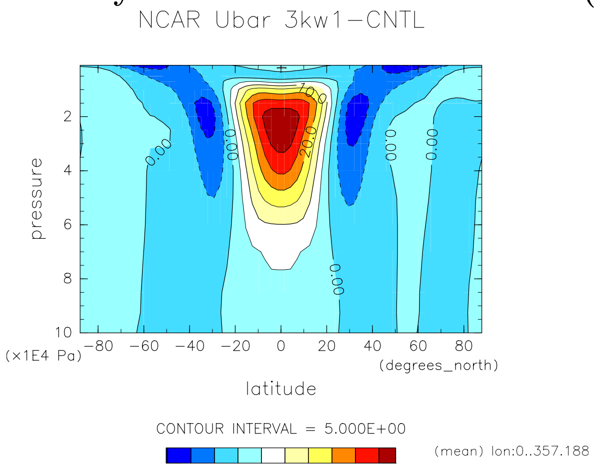

Fig. 18. Zonal mean zonal wind anomaly in the 3KW1 run of NCAR. Contour interval is 5 m/s.

3KW1 Anomalies of Precipitation

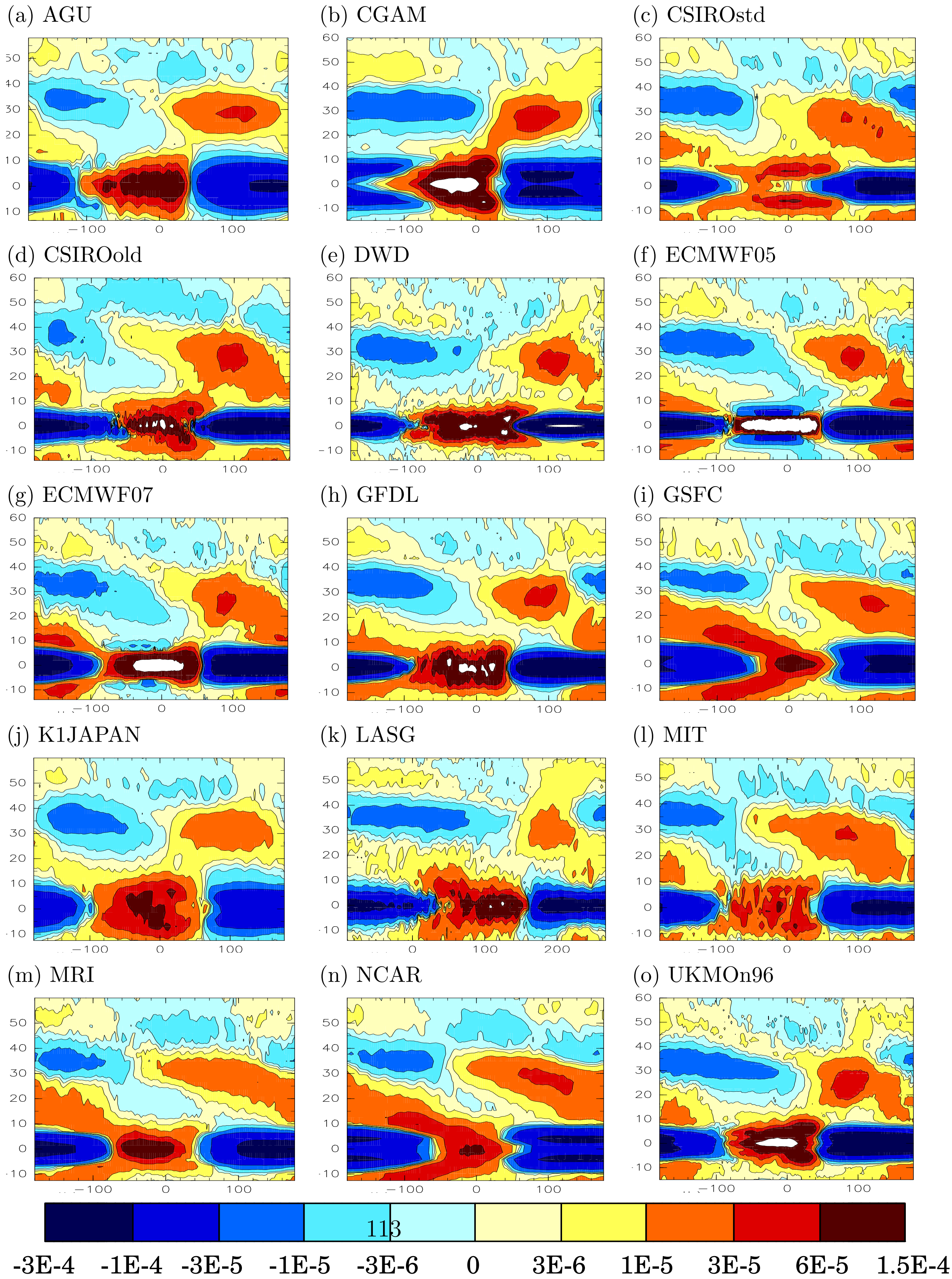

Fig. 19. Same as Fig. 4 but for the 3KW1 runs. Note that coloring for greater than 6 $\times 10^{-5}$ kg/m^{2}s is different from Fig. 4.

3KW1 Responses of Precipitation at Selected Latitude Bands

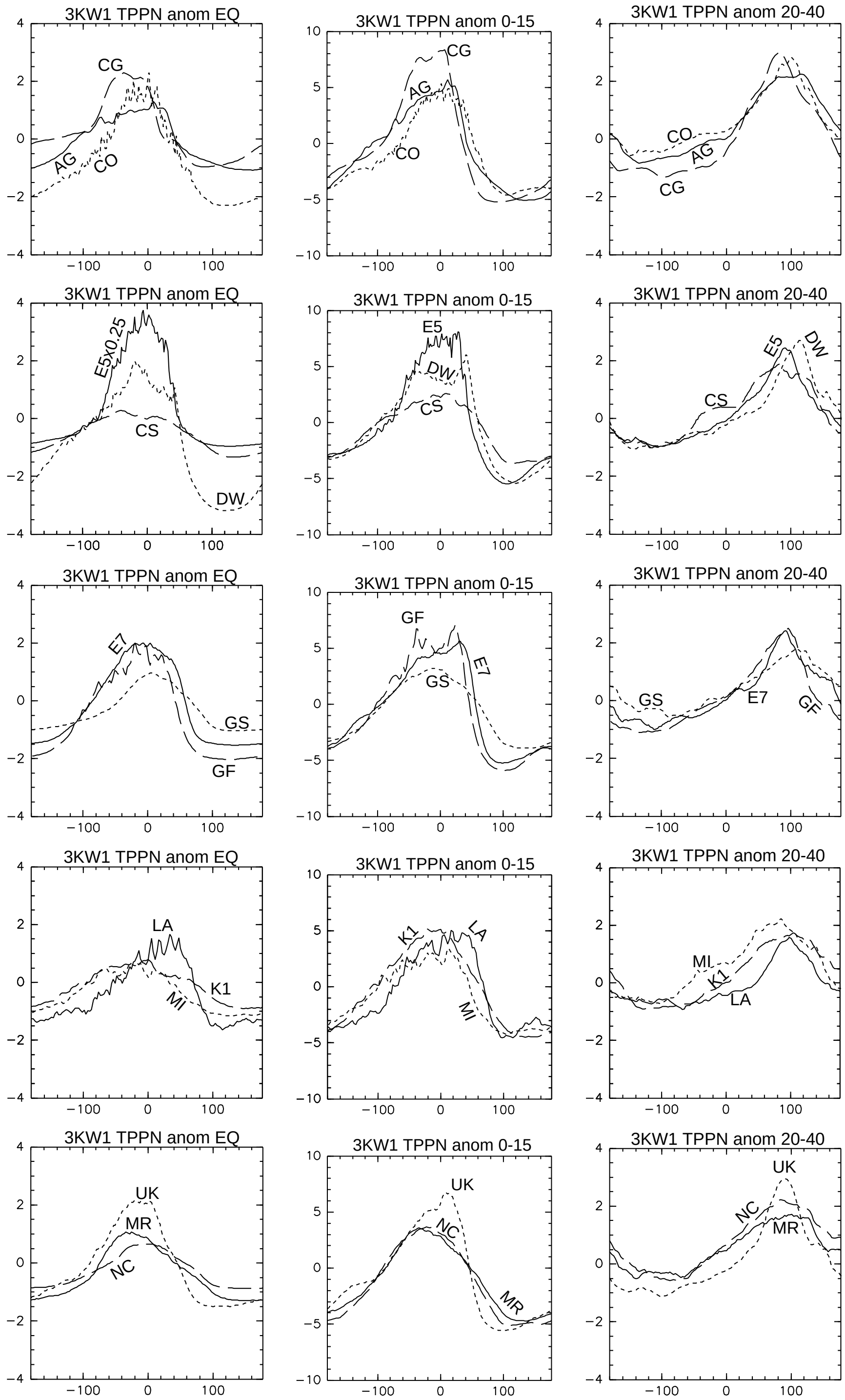

Fig. 20. Same as Fig. 5 but for the 3KW1 runs. Units are 10^{-4}[kg m^{-2} s^{-1}] for left panels, 10^{-5}[kg m^{-2} s^{-1}] for center and right panels, respectively. See Table 1 for the legends of labels.

3KW1 Anomalies of Geopotential height, u, v at 250hPa

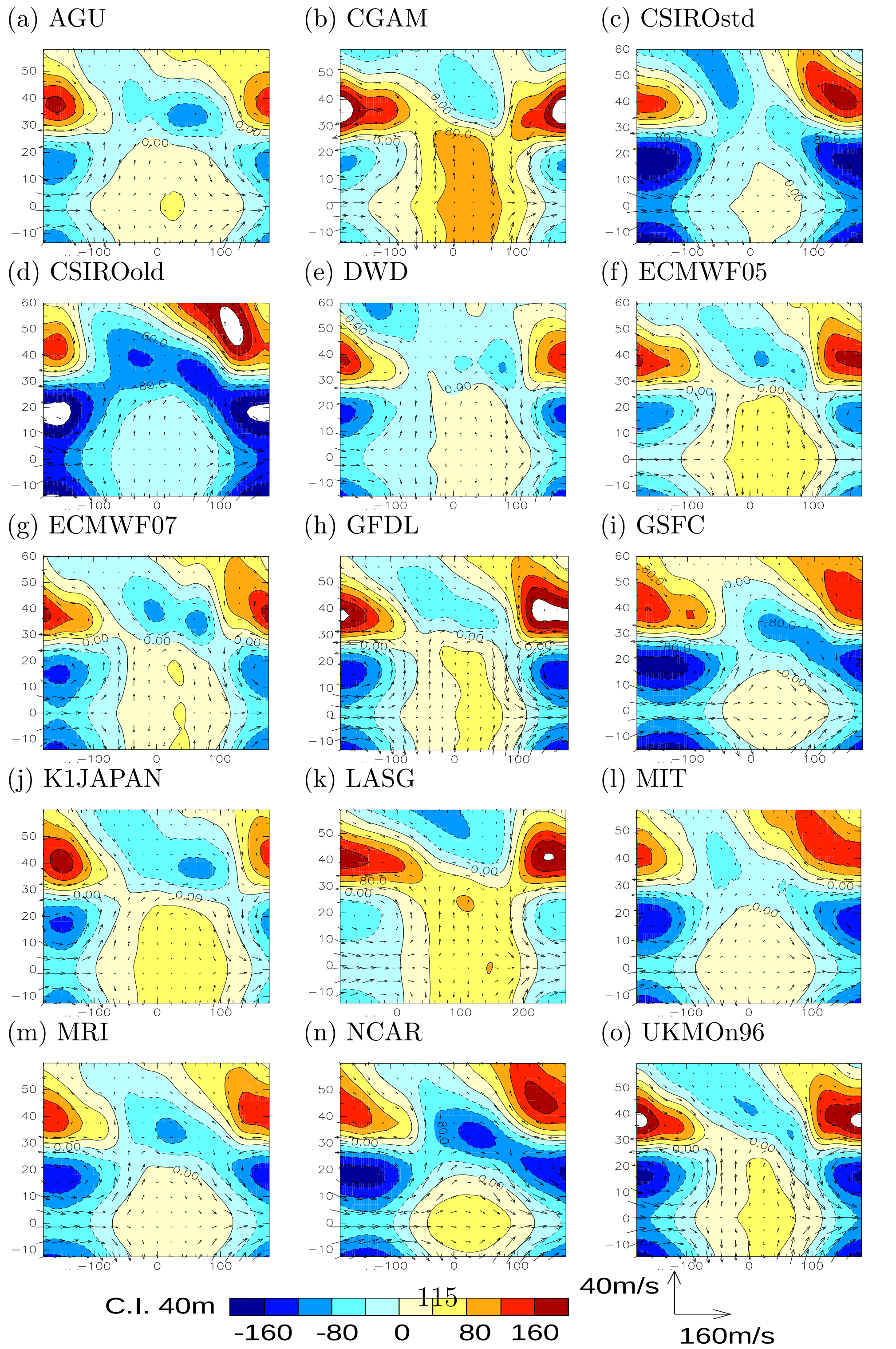

Fig. 21. Time mean anomalies of geopotential height and horizontal velocity vector at 250hPa in the 3KW1 runs of 15 APE models. Contour interval and magnitudes of wind vector components are indicated at the bottom.

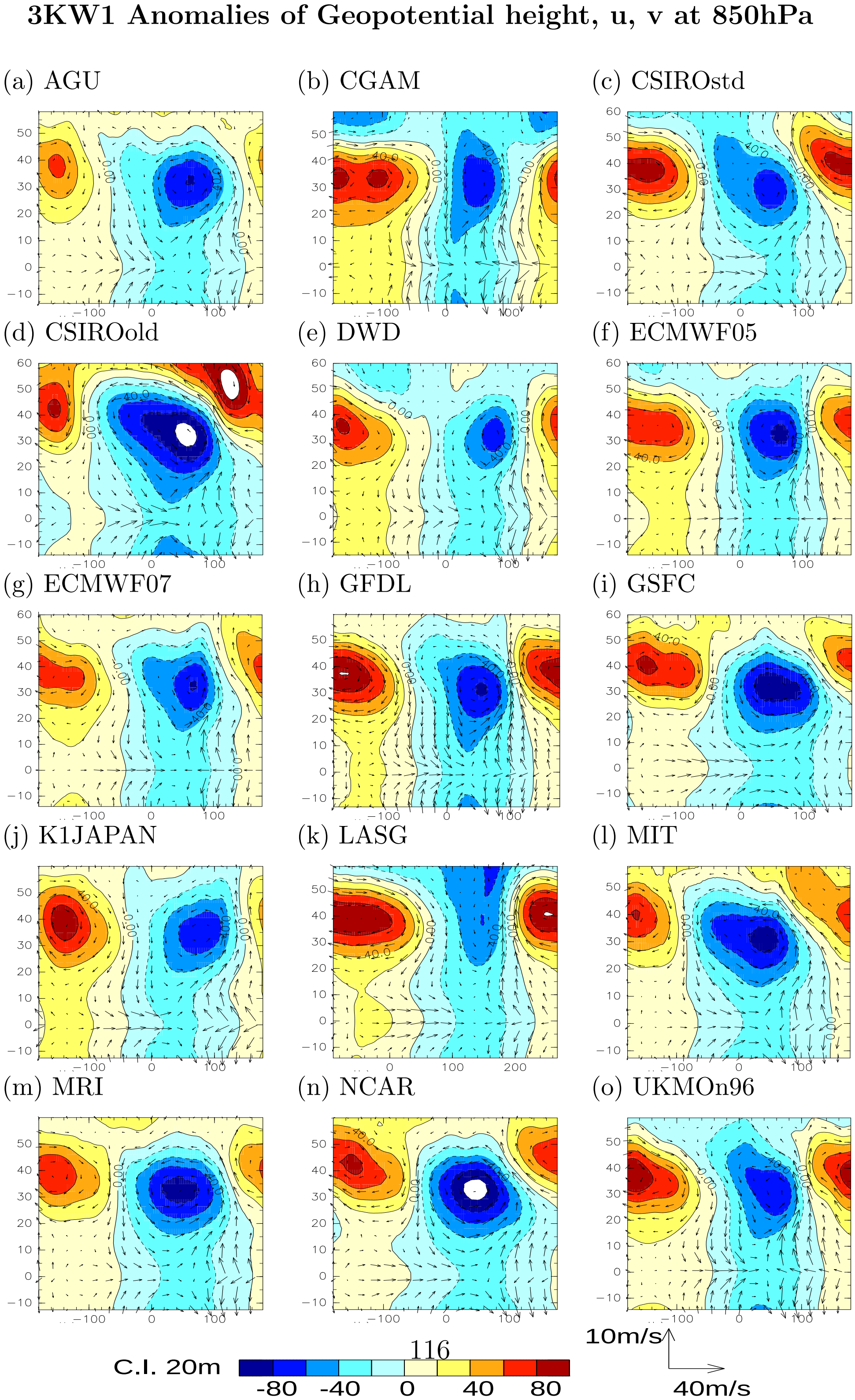

Fig. 22. Same as Fig. 21 but for 850hPa.

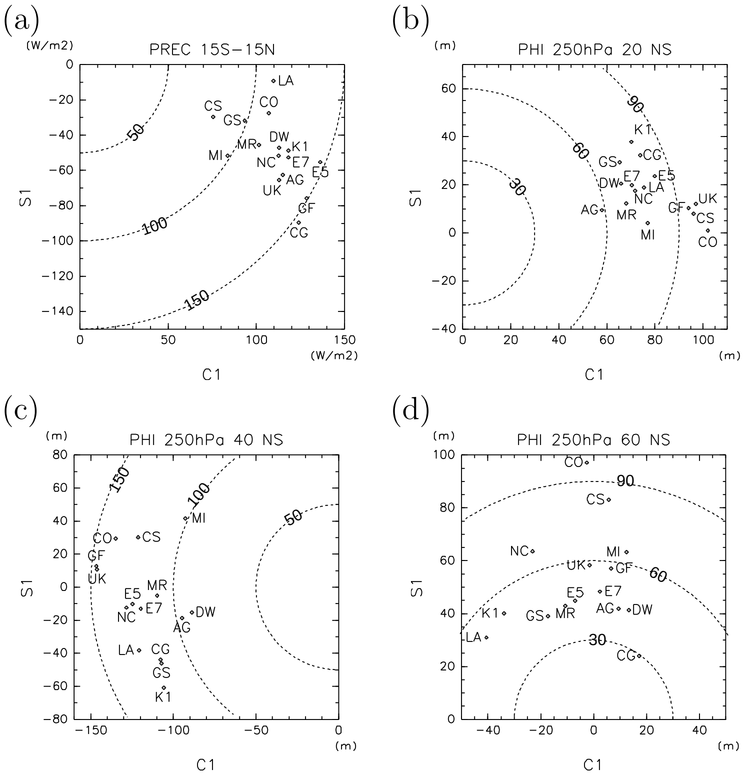

Fig. 23. Scatter plots showing the sine(s1) and the cosine (c1) coefficients of wavenumber one components of variables in the 3KW1 runs of 15 APE models. (a) Precipitation averaged within ±15 degrees from the equator, (b) geopotential height at 20°N, (c) geopotential height at 40°N, and (d) geopotential height at 60°N. Dashed lines indicate magnitudes. See Table 1 for the legends of labels.

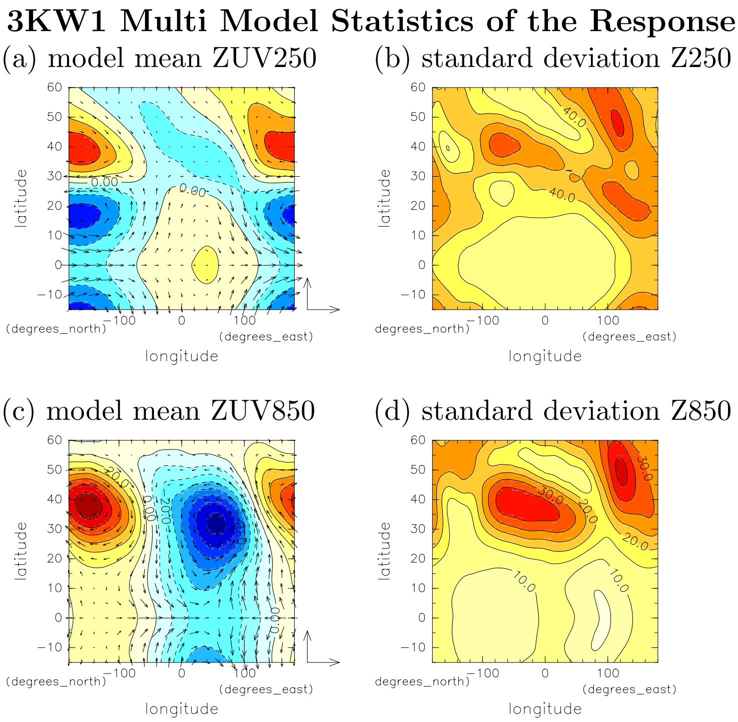

Fig. 24. Time mean anomalies of Multi model statistics of the response in the 3KW1 runs of 15 APE models. (a) Model averages of the temporal mean anomalies of geopotential height and horizontal velocity vector at 250hPa. Contour interval is 40m. The unit vectors of zonal and meridional wind are 80m/s and 20m/s, respectively. (b) The standard deviation of the temporal mean anomalies of geopotential height 250hPa. Contour interval is 10m. (c) Same as (a) but for 850hPa. Contour interval is 10m. The unit vectors of zonal and meridional wind are 20m/s and 5m/s, respectively. (d) Same as (b) but for 850hPa. Contour interval is 5m.

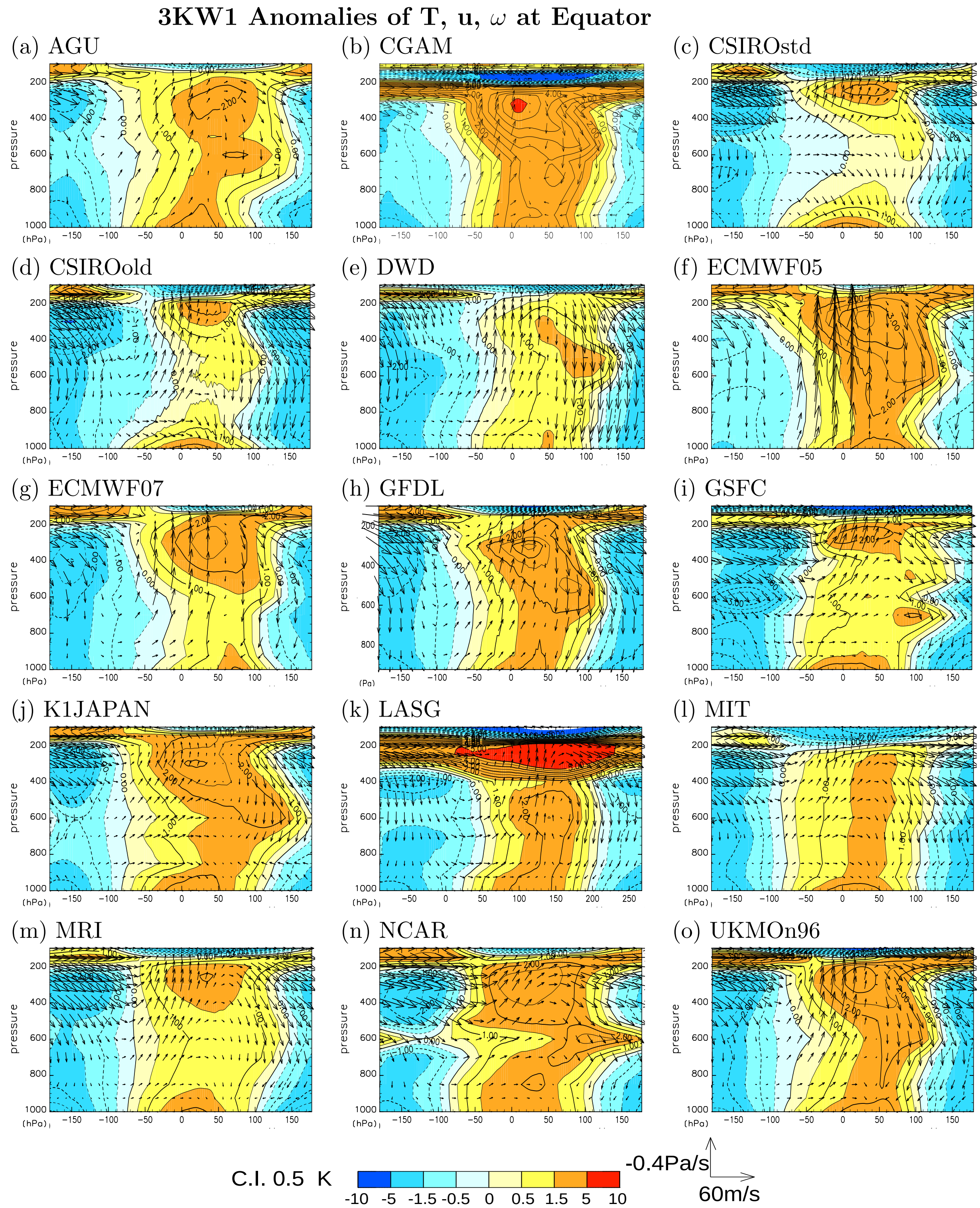

Fig. 25. Vertical distributions of time mean anomalies of temperature, zonal velocity, and p-velocity along the equator in the 3KW1 runs of 15 APE models. Contour interval and magnitudes of wind vector components are indicated at the bottom.

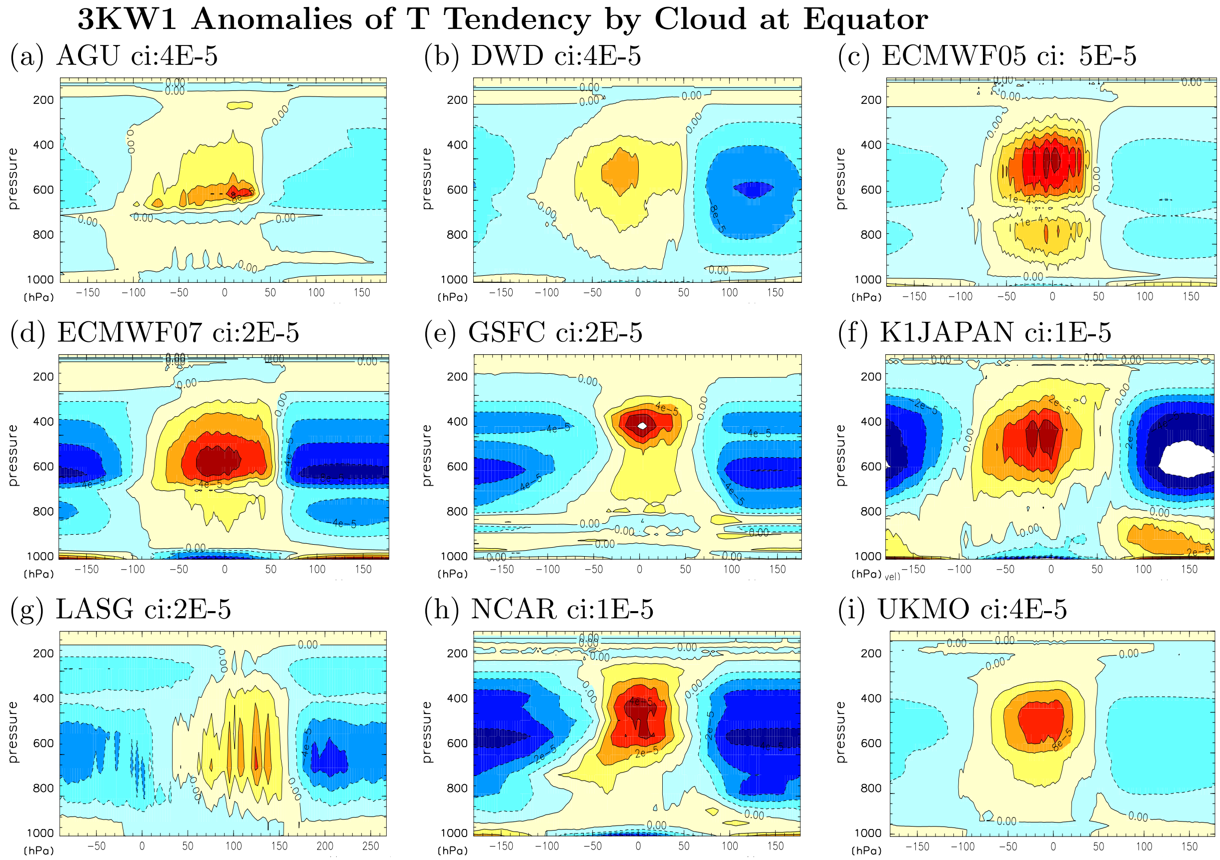

Fig. 26. Vertical distributions of time mean temperature tendencies at the equator in the 3KW1 runs of 9 APE models. Contour interval is indicated at the top of each panel. Vertical axis is pressure.

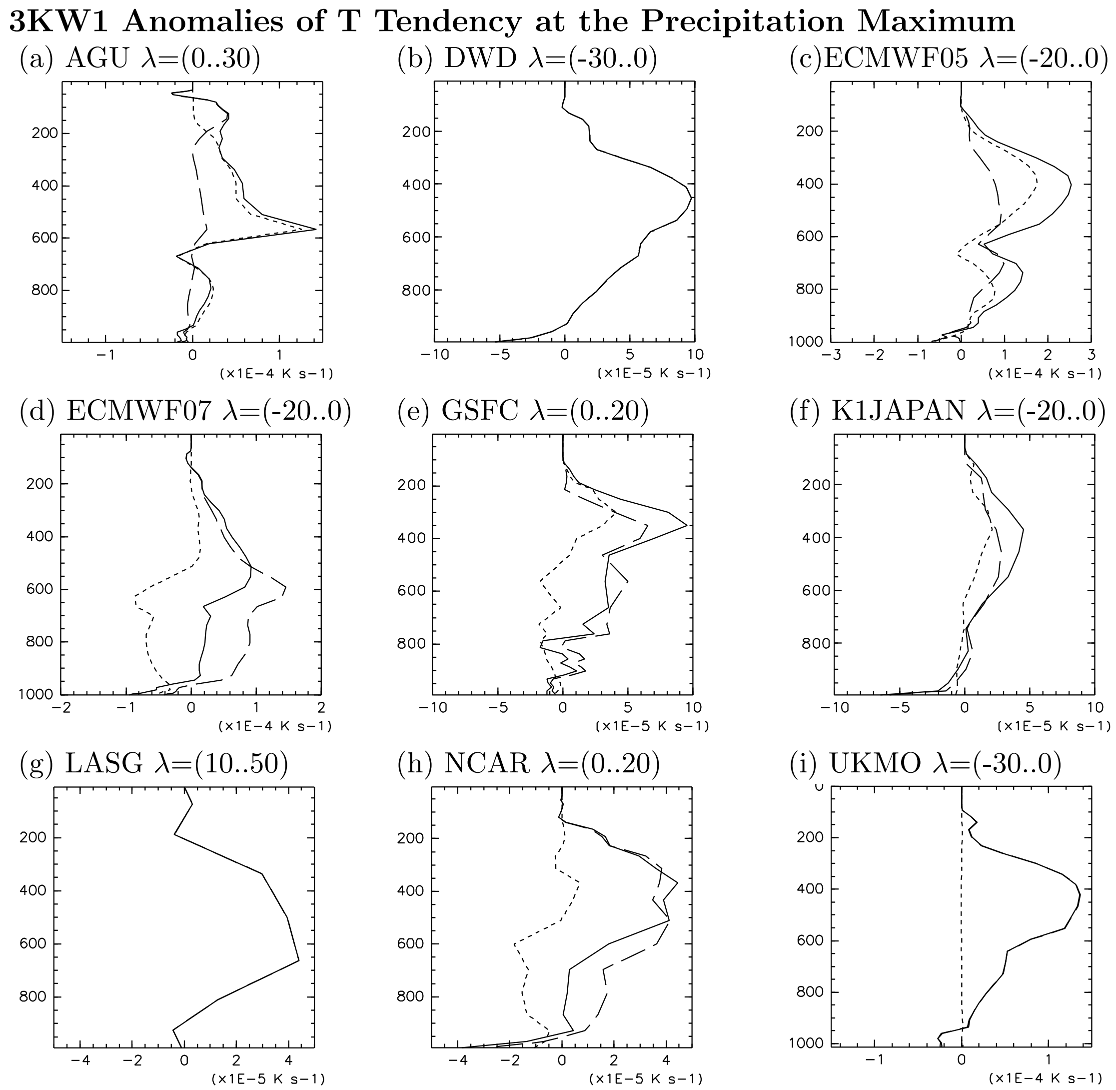

Fig. 27. Vertical profiles of time mean temperature tendencies at the SST anomaly in the 3KW1 runs of the 9 APE models from which data are provided. Unit is K s^{-1}. Vertical axis is pressure. Dotted and dashed lines indicate tendencies due to resolved clouds and due to parameterized convection, respectively, and solid line indicate the sum of the two. Note that heating due to resolved clouds is not available for DWD and LASG.

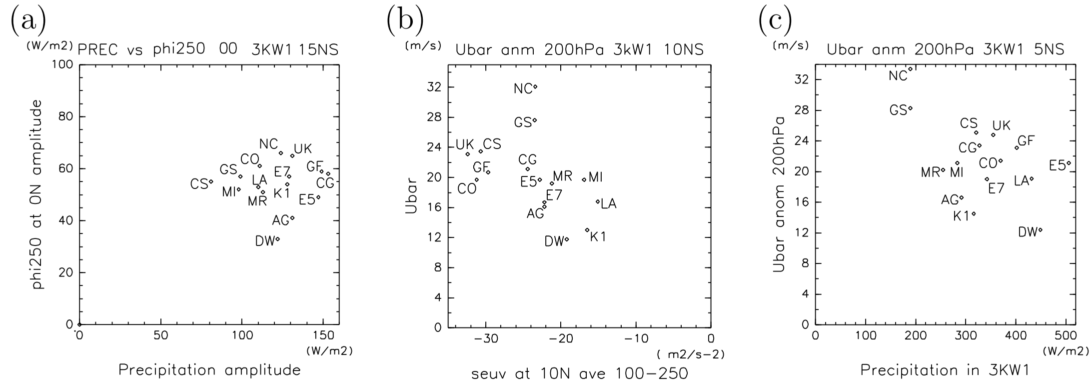

Fig. 28. Scatter plots concerning the dynamical response of the variables in the 3KW1 runs of 15 APE models. (a) The amplitude of wavenumber one component of geopotential anomaly at 250hPa at the equator vs that precipitation anomaly averaged within 15 degrees from the equator. (b) Poleward zonal momentum flux associated with stationary eddy at 10°N averaged for pressure levels between 100hPa and 250hPa vs zonal mean acceleration averaged within 10 degrees from the equator at 200hPa. (c) Zonally mean precipitation averaged within 5 degrees from the equator vs zonal mean acceleration averaged within 15 degrees from the equator at 200hPa. See Table 1 for the legends of labels.

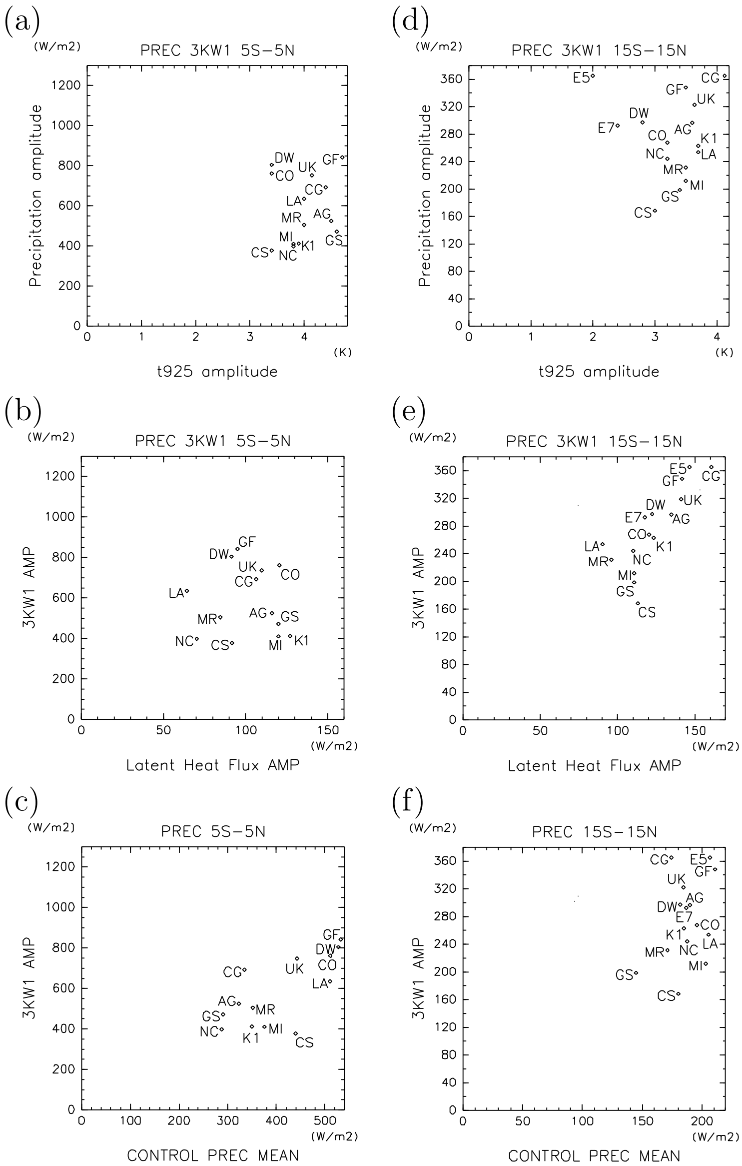

Fig. 29. Same as Fig. 15 but for 3KW1.

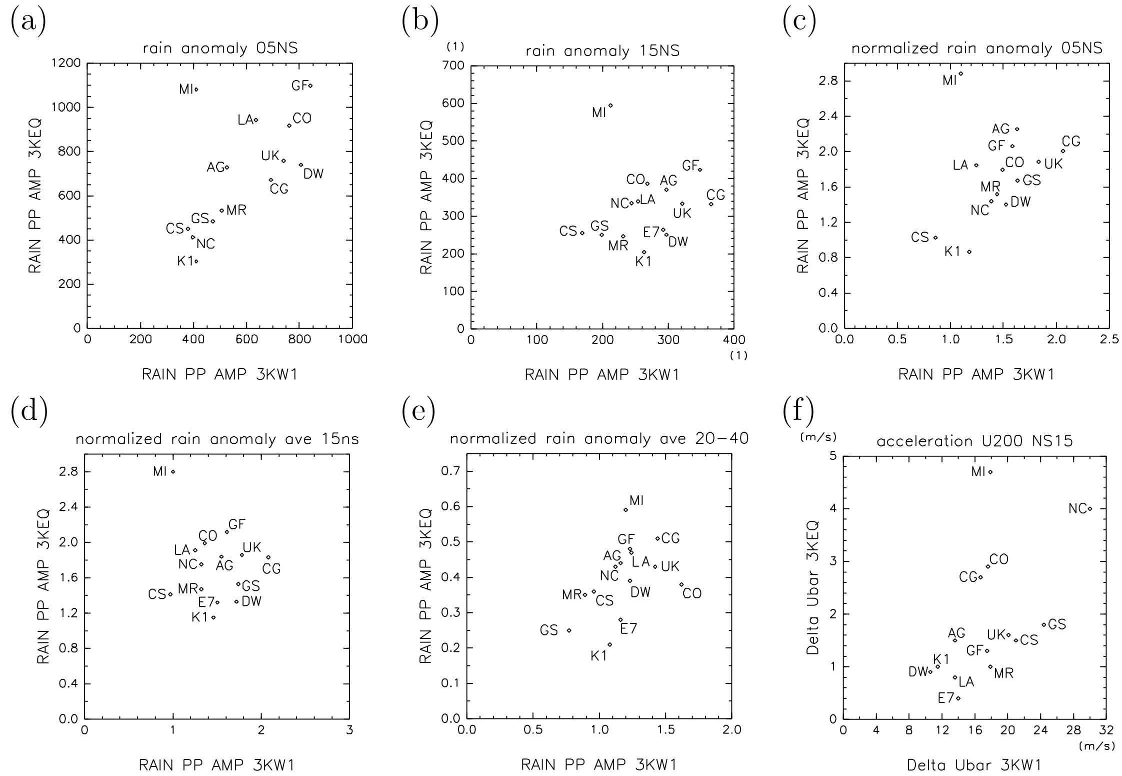

Fig. 30. Scatter plots comparing the amplitudes of anomalies in the 3KEQ and the 3KW1 runs of the APE models. (a) precipitation averaged over the equatorial latitudinal band within ±5°. (b) same as (a) but for averaged within ±15°. (c) same as (a) but for the amplitude of precipitation anomaly normalized by the time mean zonal mean precipitation of the corresponding CONTROL run. (d) same as (c) but for averaged within ±15°. (e) same as (c) but for averaged over the latitudinal band from 20°N and 40°N. (f) Change of zonal mean zonal wind at 200hPa averaged over the equatorial latitudinal band within ±5°. See Table 1 for the legends of labels.

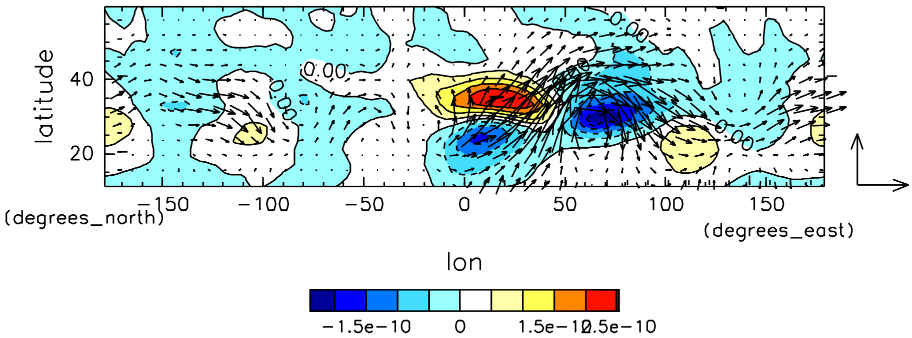

Fig. 31. Rossby wave source term of Sardeshmukh and Hoskins (1988), and the horizontal components of wave activity flux vector of Takaya Nakamura (2001) at 250hPa for the 3KEQ run of GFDL. Contour interval is 5×10^{-11}[s^{-2}]. Unit vectors corresponds to 25 [m^2s^{-2}].

List of Tables

Table 1. Participating models

group symbol	model	horizontal resolution	no.of levels	deep convection	short symbol	PF data	note
AGU	AFES	T39	48	Emanuel	AG	○	
CGAM	HadAM3	3.75° x 2.5°	30	Gregory-Rawntree	CG		
CSIROstd	CCAM-05e	∼210km	18	McGregor	CS		
CSIROold	CCAM-05a	∼210km	18	McGregor	CO		
DWD	GME	∼1°	31	Tiedtke	DW	○	
ECMWF05	IFS cy29r2	T159	60	Bechtold *et al.* 2004	E5	○	a,b
ECMWF07	IFS cy32r3	T159	60	Bechtold *et al.* 2008	E7	○	b
GFDL	AM2.1	2.5° x 2°	24	RAS	GF		c
GSFC	NSIPP-1	3.75° x 3°	34	RAS	GS	○	
K1JAPAN	CCSR/NIES 5.7	T42	20	Pan-Randall	K1	○	
LASG	SAMIL	R42	9	Manabe	LA	○	
MIT	MIT-GCM	∼280km	40	RAS	MI		
MRI	MRI/JMA98	T42	30	Randall-Pan	MR		
NCAR	CCSM-CAM3	T42	26	Zhang-McFarlane	NC	○	
UKMOn96	pre-HadGAM1	1.875° x 1.25°	38	Gregory 1999	UK	○	

a. Western half of the 3KEQ SSTA is lacking.
b. Meridional scale of the 3KW1 SSTA is halved.
c. Mean sea level pressure is 1000hPa.

Table 2. 3KEQ Responses of Precipitation normalized by CONTROL

GROUP	equator %		off-equator %			ave. in 15S-15N %		ave. in 20N-40N %	
SYMBOL	min	max	min	max	lat.	min	max	min	max
AGU	79	327	–	–	–	77	261	83	127
CGAM	83	318	58	276	6	70	253	80	131
CSIROstd	86	171	59	211	5	75	216	83	119
CSIROold	66	242	–	–	–	62	261	91	129
DWD	82	194	–	–	–	73	206	78	117
ECMWF05	72	275	–	–	–	78	239	89	115
ECMWF07	81	198	62	221	5	72	204	89	117
GFDL	70	282	–	–	–	69	281	77	125
GSFC	82	265	51	243	6	69	222	88	113
K1JAPAN	88	156	70	210	5	75	190	94	115
LASG	66	258	–	–	–	67	258	75	122
MIT	56	333	39	308	5	48	328	74	133
MRI	84	238	49	180	5	75	222	82	117
NCAR	85	226	39	287	6	69	244	88	131
UKMOn96	87	280	37	292	5	68	254	79	122

Table 3. 3KW1 Responses of Precipitation normalized by CONTROL

GROUP	equator %		off-equator %			ave. in	15S-15N %	ave. in	20N-40N %
SYMBOL	min	max	min	max	lat.	min	max	min	max
AGU	23	193	–	–	–	26	181	68	184
CGAM	24	282	13	199	4	19	227	55	199
CSIROstd	29	115	95	422	8	47	144	63	159
CSIROold	17	183	–	–	–	35	171	73	235
DWD	10	156	–	–	–	24	186	66	189
ECMWF05	9	456	–	–	–	29	207	67	191
ECMWF07	9	219	–	–	–	24	177	67	173
GFDL	13	184	–	–	–	25	186	63	186
GSFC	9	185	9	162	6	26	200	82	159
K1JAPAN	42	150	17	247	5	34	180	62	170
LASG	37	164	–	–	–	40	165	55	179
MIT	27	141	–	–	–	42	142	75	195
MRI	17	169	–	–	–	24	156	82	171
NCAR	13	164	13	138	6	25	157	72	184
UKMOn96	15	223	14	182	3	22	200	61	203